A flux calibration device for Integral Field Spectrographs

Dissertation
zur Erlangung des akademischen Grades

Doctor rerum naturalium
(Dr. rer. nat.)

im Fach Physik
Spezialisierung: Experimental Physik

eingereicht an der
Mathematisch-Naturwissenschaftlichen Fakultät
der Humboldt-Universität zu Berlin
von

M. Sc. Simona Lombardo

Präsidentin der Humboldt-Universität zu Berlin
Prof. Dr.-Ing. Dr. Sabine Kunst

Dekan der Mathematisch-Naturwissenschaftlichen Fakultät
Prof. Dr. Elmar Kulke

Gutachter:	1. Prof. Dr. Marek Kowalski 2. Prof. Dr. Thomas Lohse 3. Prof. Dr. Martin M. Roth
Tag der mündlichen Prüfung:	18.05.2017

To my favorite star,
may you always be in my life
and point me to the right direction.

Declaration

I declare that I have produced this doctor's thesis independently using only the tools I have specified, in accordance with section 7 para. 3 of the Faculty of Mathematics and Natural Sciences PhD regulations, published in the Official Gazette of Humboldt-Universität zu Berlin (*Amtliches Mitteilungsblatt*) no. 126/2014 on 18/11/2014.

I have not applied for a doctoral degree in the doctoral subject of Physik elsewhere and do not hold a doctoral degree in the doctoral subject of Physik.

I have taken due note of the Faculty of Mathematics and Natural Sciences PhD Regulations, published in the Official Gazette of Humboldt-Universität zu Berlin (Amtliches Mitteilungsblatt) no. 126/2014 on 18/11/2014.'

M. Sc. Simona Lombardo
June 2017

Abstract

SNe Ia can be used as standard candles to measure the dark energy equation of state parameter, w. Having observed a good number of these objects, current studies are limited by systematic uncertainties, among which relative (color) flux calibration is dominating. There are ongoing efforts in all the current (SNLS, Pan-STARRS, DES) and future (LSST, WFIRST) major surveys to develop new techniques and instruments for calibration in order to gain a 1% precision knowledge of the instrumental artifacts. This work presents a way to solve, or at least limit, the problem with the SNIFS Calibration Apparatus (SCALA). SCALA's goal is to provide high precision calibration for the "telescope + SNIFS" system and refine the primary standard star network, to eliminate the uncertainties due to the knowledge of their models. SCALA produces 18 quasi-parallel and collimated monochromatic (and wavelength tunable) beams with opening angles of 1 degree. The combination of these beams allows us to achieve an illumination of the focal plane of the UH 88 telescope, that is flat to within 1%. SCALA was commissioned in 2014 and fully deployed in 2015. In the in-situ set up, one of the SCALA beams is constantly monitored by a photodiode (calibrated against a NIST-calibrated photodiode), which is used as flux standard to transfer the NIST-calibration to the telescope+instrument first, and the standard star spectra afterwards. We use another of these calibrated photodiodes to reconstruct the spectral relative efficiency of the light produced by the other 17 beams, by moving it from beam to beam. We are able in this way to reproduce the overall wavelength trend of the illumination from SCALA with a precision better than 1%, by comparing this in-situ measurements with a laboratory characterization of the SCALA beams. We are able to produce throughput curves of the SNIFS+UH 88 system. The measured systematics affecting our results sum to errors smaller than 0.7%. We are currently comparing the calibration of the system achieved with SCALA with the traditional calibration obtained by observing standard stars.

Zusammenfassung

SNe Ia können als Standardkerzen verwendet werden, um den Parameter für dunkle Energie w in der Zustandgleichung zu messen. Nachdem viele dieser Objekt beobachtet wurden, wird die Genauigkeit aktueller Studien durch systematische Fehler beschränkt, wobei die Flusskalibrierung die dominierende Fehlerquelle ist. In dieser Arbeit wird eine Möglichkeit präsentiert, das Problem mit dem "SNIFS Calibration Apparatus" (SCALA) zu lösen oder wenigstens zu verringern. Das Ziel von SCALA ist es für das System, das aus dem Teleskop und SNIFS besteht, eine Hochpräzisionskalibrierung zu erreichen, sowie das Standardstern-Netzwerk zu erweitern, um die Ungenauigkeiten zu unterdrücken, die aus den Modellen resultieren. SCALA erzeugt 18 nahezu parallele und kolimierte monochromatische Strahlen (mit regulierbarer Wellenlänge), die Öffnungswinkel von einem Grad haben. Durch die Kombination dieser Strahlen lässt sich die Bildebene des UH88 Teleskops (Universität Hawaii 88 inch Teleskop) mit einer Genauigkeit von 1% gleichmäßig ausleuchten. SCALA wurde im Jahr 2014 installiert und ist seit 2015 regulär in Betrieb. Im in-situ Aufbau wird einer der Strahlen ständig mit einer Photodiode überwacht, die mit einer NIST-kalibrierten Photodiode kalibriert wurde. Sie dient als Standard, um die NIST-Kalibrierung zuerst auf das System aus Teleskop und Instrument und danach auf die Standardsterne zu übertragen. Eine zweite so kalibrierte Photodiode wird von Strahl zu Strahl bewegt, um den Helligkeitsverlauf der anderen 17 Strahlen als Funktion der Wellenlänge zu messen. Auf diese Weise sind wir in der Lage die Ausleuchtung von SCALA mit einer Genauigkeit von besser als 1% zu reproduzieren, indem wir die in-situ Messungen mit den im Labor gemessenen Eigenschaften der Strahlen vergleichen. So können bei bekannter Farbe des emittierten und des beobachteten Lichts die Durchsatzkurven des SNIFS+UH 88 Systems gemessen werden. Die gemessenen systematischen Ungenauigkeiten der Messung betragen weniger als 0.7%. Da in der selben Nacht sowohl die Standardsterne als auch SCALA beobachtet wurden, besteht der nächste Schritt darin, die Kalibration, die SCALA erreicht, mit der traditionellen Kalibration, der Beobachtung von Standardsternen, zu vergleichen.

Table of contents

Chapter 1

Introduction

There is no such thing as a perfect measurement. Every time a measurement is made, whether it is of the length of a table or the number of electrons in a Charge-Coupled Device (CCD) chip, this includes an error. However, we can try to minimize the error by making sure to use a tool for the task that reduces these problems.

For example, how could one derive the diameter of an ideal, perfectly spherical, orange below the skin, without peeling it? One could measure the diameter of the orange with its skin, and then use a known (in this case fictional) law that connects the thickness of the skin to the overall diameter. So we can now derive the diameter, but how well will we know it?

We are facing two major kinds of error. First, we have an error directly related to the knowledge of the object we want to study. How precise is the relationship between skin thickness and diameter? Are we sure that it is really an orange and not a grapefruit, or a very large mandarine? Unfortunately, our current (lack of) knowledge of oranges prevents us from ignoring those questions completely, but there are ongoing studies which will hopefully shed light on the matter.

The second source of error is due to the precision with which we measure the diameter. Is our ruler good enough? Does it have mm or nm notches? How well does it compare to the official standard? How carefully is the measurement made? By improving the technique with which the ruler is built and used we can directly reduce such measurement errors.

Leaving now the fictional world with all its theories of thickness of fruit's skin, the oranges I studied are called type Ia Supernovae (SNe Ia). They are extremely bright explosions of stars, and the quantity to measure is their luminosity.

During my PhD I worked on reducing both kind of errors: trying to improve the knowledge we have of SNe on one hand (see Appendix B.1), and building an instrument to improve the precision of the tools used to observe them on the other hand.

The reason that makes these objects worth so much trouble is their use as standard candles for cosmological research. Whatever physical process causes SNe Ia, this is almost

always closely repeated, creating nearly identical light-curves (brightness as function of time). Furthermore, they are extremely bright and can thus be observed also at very large distances. Through measuring how faint SNe Ia appear to us, we can thus estimate their (relative) distances.

Such a strong probe of the universe is very appealing to cosmologists who wants to investigate its origin and evolution. SNe Ia provided the first evidence for the accelerated expansion of the universe (Perlmutter et al., 1999; Riess et al., 1998), and they are currently used to measure finer quantities of cosmological theories (e.g. the dark energy equation of state parameter, w). However, after having observed many of these objects, current studies are limited by systematic uncertainties, among which the flux calibration is dominating (Betoule et al., 2014; Conley et al., 2011). Flux calibration in astronomy is a fundamental step in data reduction, in which the counts recorded on the detector (CCD) are transformed into physical flux entering the Earth atmosphere. This calibration is performed by comparing the observed spectra of so called standard stars with their assumed intrinsic spectra. These spectra are today ultimately derived from models of star atmospheres (pure hydrogen white dwarfs).

It is the flux ratio between nearby and very far SNe that allows us to constrain cosmological parameters. When photons from very distant objects travels towards us, the expanding universe causes an effect called cosmological redshift, which acts in an equivalent way as a Doppler effect in shifting the light towards redder wavelengths. Therefore, photons from distant SNe are redshifted, and thus, while the absolute flux (the intrinsic brightness of SN Ia) cancels in the flux ratio relevant to cosmology, one has to establish a reliable (relative) flux calibration as a function of wavelength. A relative flux calibration only provides the conversion of counts as function of wavelength ignoring the absolute scaling, that instead defines the absolute flux calibration.

Reducing the systematic calibration uncertainties (the second kind of error in the orange thought experiment) can be divided into two tasks: knowledge of the instrumental artifacts and of the atmospheric extinction (Stubbs and Tonry, 2006).

There is an ongoing effort to develop new techniques and instruments for calibration (Regnault et al., 2015; Stubbs et al., 2010) in order to reach a 1% precision knowledge of the instrumental artifacts. My PhD thesis focuses on a new approach to the problem using the SNIFS Calibration Apparatus (SCALA), an in-situ flux calibration device developed for the SuperNova Integral Field Spectrograph (SNIFS, Lantz et al., 2004) mounted on the 2.2 m telescope of the University of Hawaii. SCALA's main purpose is to calibrate the relative instrumental response of the "telescope + SNIFS" system to 1% precision. Such a device will provide an independent verification of the flux calibration by recalibrating the network of standard stars currently observed for flux calibration. SCALA was commissioned in 2014 and fully deployed in 2015. It is operational and remotely controllable.

SCALA is unique in that it is is built to calibrate an Integral Field Spectrograph. As already mentioned, calibration is crucial to improve the cosmological constraints obtained from SN observations. However, even with a perfectly calibrated system, systematic uncertainties also arise since the SN explosion mechanism, and all the physics involved, is not yet fully understood. An IFS has unique possibilities to obtain photometric and spectroscopic information. Photometric because it produces images of the field of view observed, keeping the spatial information on where the sources are located, and spectroscopic because these images are produced for each wavelength observed. This means that every pixel in the image has a spectrum.

The Nearby Supernova factory (SNfactory) observes nearby SNe with SNIFS. The spectrophotometric time series – a series of spectrophotometric observations of the SN at different times from the explosion – produced by SNIFS also enable to test and improve the algorithms used to determine the peak SN luminosity ("standardization") and, hence, to prevent possible biases in their results (i.e. corresponding to verifying what kind of fruit is at hand!). With all these qualities IFSs are the kind of instrument that allows to avoid systematic uncertainties in SN cosmology that affect traditional photometry-based surveys.

Improving the calibration of such an instrument and reducing the instrumental systematic uncertainties by doing so, would directly propagate to reduced systematic uncertainties on cosmological parameters. With SCALA we aim to calibrate SNIFS at a 1% precision level and use it to recalibrate the standard star network. This newly calibrated network could be used by every other survey that observes the same stars and in turn uses them to calibrate its own instruments.

In the next chapters of this thesis some theoretical background on cosmology will be given (chapter 2) and some of the observables used to constraint cosmological parameters will be described (chapter 3). We will then exclusively focus on the observations of SNe Ia, the current results achieved and their limitations (chapter 3). We will then discuss the importance of calibration and the techniques currently used to calibrate astronomical images and instruments (chapter 4). We will describe the SNfactory project (chapter 5), of which I am part, and give the required details on the integral field spectrograph that we want to calibrate (SNIFS). We will describe the design of SCALA (chapter 6) and show some of the pre-commissioning simulations and system-tests that helped refining design and characterization of SCALA. We will then focus on the calibrated photodiode data used to monitor the light produced by SCALA (chapter 7). In chapter 8, the first commissioning phase in 2014 and the final deployment in 2015 are described along with the different tests and measurements performed to reproduce the pre-commissioning characterization of SCALA. In chapter 9 we explain how we process the SCALA observations acquired by the reference photodiode and by SNIFS. During the deployment phase we measured the SNIFS+telescope system response as function of wavelength and compared it to the response obtained with the calibration

achieved through standard stars observations. The results of this measurement and the comparison between these calibration methodologies are shown in chapter 10. In the same chapter the systematics that affect our measurements are also discussed. We conclude in chapter 11.

My contribution to SCALA development The construction and commissioning of SCALA required the work of many people. Since the beginning of my PhD I simulated its performances to refine the design, initially laid out by Prof. Marek Kowalski, Dr. Akos Hoffmann and Eymen Alyaz. After the construction, I lead the lab testing of the system and the two commissioning phases, with inputs by Daniel Küsters (halogen lamp and primary mirror mask design), Dr. Akos Hoffmann (technical assistance), Dr. Klaus Reif (design consultant), Dr. Mickael Rigault (development of controlling software). I also built the pipeline for processing the calibration data and analyze them. Determining the fully correlated error on the calibration, as well as recalibrating the standard star network, are part of an ongoing PhD thesis work by Daniel Küsters and outside the scope of this work.

Chapter 2

The evolution of the Universe

The goal of cosmology is to explain the origin and evolution of the universe. Einstein's theory of General relativity provides the necessary formalism for doing so. It is based on a geometrical interpretation of gravity and makes use of a metric that relates coordinates to physical distances:

$$ds^2 = g_{\mu\nu} dx^\mu dx^\nu, \tag{2.1}$$

where $g_{\mu\nu}$ is the metric, ds an infinitesimal line element and dx the coordinates. In this chapter we will derive some of the fundamental equations and describe some of the possible observables which are used in the rest of the thesis.

2.1 A metric for the universe

The theories that describe how the universe evolves are based on two assumptions, supported by observational evidence, called the cosmological principles: spatial homogeneity and isotropy at large scales (larger than 100 Mpc), which means that the universe is invariant under translation and rotation. Under these assumptions the metric assumes a simpler form.

2.1.1 FLRW Metric

Friedmann-Lemaitre-Robertson-Walker (FLRW) (Friedmann, 1922; Lemaître, 1927; Robertson, 1929; Walker, 1933) derived a four-dimensional metric tensor in spherical coordinates, for a homogeneous and isotropic universe:

$$ds^2 = -c^2 dt^2 + a^2(t)[d\chi^2 + S_k(\chi)^2 d\Omega^2], \tag{2.2}$$

where

$$d\Omega^2 \equiv d\theta^2 + \sin^2\theta d\phi^2 \tag{2.3}$$

and

$$S_k(\chi) = \begin{cases} \sqrt{|K|^{-1}}\sin(\sqrt{|K|}\chi), & \text{for K} > 0 \\ \chi, & \text{for K} = 0 \\ \sqrt{|K|^{-1}}\sinh(\sqrt{|K|}\chi), & \text{for K} < 0\ , \end{cases} \tag{2.4}$$

with K varying between a closed ($K > 0$, spherical), flat ($K = 0$) and open ($K < 0$) universe, $a(t)$ is the scale factor, which describes how distances between objects contract or expand as function of time, χ is a comoving radial coordinate, θ and ϕ are angular coordinates. The comoving distance, χ, between two objects remains invariant, which means that if the universe expands it will stay the same, while the proper – physical – distance grows with the scale factor.

2.1.2 Einstein equations

Einstein's field equation provides the relation between geometry (described through the Einstein tensor, which in turn is constructed from $g_{\mu\nu}$ and its derivatives) and the energy content described by the energy-momentum tensor, $T^{\mu\nu}$.

$$G_{\mu\nu} = \frac{8\pi G}{c^4} T_{\mu\nu} + \Lambda g_{\mu\nu}, \tag{2.5}$$

where $G_{\mu\nu}$ is the Einstein tensor, G is Newton's gravitational constant[1], and Λ is the cosmological constant introduced by Einstein to achieve a static universe. The energy-momentum tensor for a perfect fluid in thermodynamic equilibrium is $T^{\mu\nu} = (\rho + p/c^2)u^\mu u^\nu + pg^{\mu\nu}$, where p is the pressure, ρ is the mass-energy density and $u^{\mu\nu}$ is the fluid four velocity. Λ has been considered equal to zero for many years before the discovery of the accelerated expansion of the universe (Perlmutter et al., 1999; Riess et al., 1998), which will be discussed in the next chapter.

2.1.3 Friedmann equations

We can, as first a approximation, fill the universe with a perfect isotropic fluid, to expand the right-hand side of eq. 2.5 under the cosmological principle assumptions. We want to see how the universe evolves in time. Since the universe is assumed homogeneous and isotropic, the spatial components of $T_{\mu\nu}$ do not provide further information. We, thus, compute the evolution on the time-time component of the energy-momentum tensor, $T_{00} = \rho$, and using

[1] $G = 6.67 \times 10^{11}$ m^3/kg/s^2.

eq. 2.5, we obtain the first Friedmann equation (Friedmann, 1922):

$$H^2 \equiv \left(\frac{\dot{a}}{a}\right)^2 = \frac{8\pi G}{3}\rho + \frac{\Lambda c^2}{3} - \frac{Kc^2}{a^2}, \tag{2.6}$$

where H is called the Hubble parameter.

We have to obtain the evolution of the density ρ to solve this equation. Due to conservation of energy, the energy-momentum tensor must have a vanishing divergence, hence:

$$0 = \bigtriangledown_\mu T_0^\mu = -\dot{\rho} - 3\frac{\dot{a}}{a}\left(\rho + \frac{p}{c^2}\right). \tag{2.7}$$

For a perfect fluid, density and pressure are related by an equation of state $p = w\rho c^2$ with a constant parameter w. Eq. 2.7 is, then, simplified to:

$$\frac{\dot{\rho}}{\rho} = -3(1+w)\frac{\dot{a}}{a}, \tag{2.8}$$

$$\rho \propto a^{-3(1+w)}. \tag{2.9}$$

From the first Friedmann eq. 2.6 differentiated in time and the substitution of equation eq. 2.7, a relation between density, pressure and the acceleration of the expansion of the universe can be found:

$$\frac{\ddot{a}}{a} = -\frac{4\pi G}{3}\left(\rho + 3\frac{p}{c^2}\right) + \frac{\Lambda c^2}{3}. \tag{2.10}$$

We have, hence, obtained the second Friedmann equation. Looking at eq. 2.6 we see that adding the Λ term has the same effect of introducing another component to the universe with density:

$$\rho_\Lambda \equiv \frac{\Lambda}{8\pi G}. \tag{2.11}$$

This component will be further discussed in the following sections.

2.2 Redshift definitions

Lets assume we are observing an object that emits light at a time t_e. We will observe this light, that traveled along a null geodesic ($ds^2 = 0$), at a time $t_\mathrm{o} \neq t_\mathrm{e}$. This simplifies eq. 2.2:

$$c^2 dt^2 = a(t)^2 d\chi^2, \tag{2.12}$$

If we consider that the time between the two emitted wavelength crests, as well as the time between the observed crests, is much smaller than the time needed for the scale factor to change, then $a(t)$ is constant over that time interval. When we rearrange eq. 2.12 and integrate it over time, we obtain:

$$\frac{\lambda_e}{a(t_e)} = \int_{t_e}^{t_e+\lambda_e/c} \frac{dt}{a(t)} = \int_{t_o}^{t_o+\lambda_o/c} \frac{dt}{a(t)} = \frac{\lambda_o}{a(t_o)}. \tag{2.13}$$

From eq. 2.13 we can relate the scale factor to the *cosmological redshift*, z, considering $a(t_o) = 1$.

$$1+z = \frac{a(t_o)}{a(t_e)} = \frac{1}{a(t_e)} = \frac{\lambda_o}{\lambda_e}. \tag{2.14}$$

It is called a "red-shift" because objects observed at high redshift show lines in their spectra shifted towards redder wavelengths with respect to the laboratory frame. This means that, as the universe expands, these objects look like they are moving faster away from us, and thus seem to emit Doppler shifted light described by:

$$z = \frac{\lambda_o - \lambda_e}{\lambda_e}, \tag{2.15}$$

where λ_e is the emitted wavelength and λ_o is the observed one.

2.3 Cosmological parameters and energy content

If one assumes that the universe is filled with non-interacting fluids, its energy density can be broken down into separate components that can be identified by their equation of state parameter w. The three basic components are: matter, radiation and cosmological constant. Eq. 2.9 holds for each single component since they are assumed to be non interacting perfect fluid. We can therefore obtain their evolution with the scale factor.

Matter All non relativistic particles ($v \ll c$) are part of this group. Such particles have zero pressure and therefore $w_m = 0$, which, when substituted in eq. 2.8, yields:

$$\dot{\rho_m} + 3\frac{\dot{a}}{a}\rho_m = 0 \Rightarrow \rho_m \propto a^{-3}. \tag{2.16}$$

The energy gets diluted as the volume expands. This is expected, since the energy is only proportional to the mass of the particles.

Radiation In this category are relativistic ($v \simeq c$) particles such as photons and neutrinos. The equation of state in this case is $p = \rho/3$, hence $w_r = 1/3$ and therefore:

$$\dot{\rho_r} + 4\frac{\dot{a}}{a}\rho_r = 0 \Rightarrow \rho_r \propto a^{-4}. \tag{2.17}$$

The energy is diluted faster than in the matter case since they are redshifted, as the universe expands, and lose energy ($E = h\nu \propto a^{-1}$, where ν is the frequency of the wave), as seen in sec. 2.2 (hence the additional factor a).

Cosmological constant As mentioned, this was introduced by Einstein to produce a static universe. The interpretation would be a so far unknown form of energy with constant density. The only way to satisfy eq. 2.7 with a constant energy density is with $p = -\rho$ which means $w = -1$. The negative pressure means that this energy accelerates the expansion.

It is possible to constrain w without necessarily involving the cosmological constant, considering a more general dark energy. From the second Friedman equation, 2.10, we derive a $p_{\mathrm{DE}} < -c^2\rho_{\mathrm{DE}}/3$, without considering the term Λ and under the assumption that the effect of such a density has to be the accelerating expansion of the universe. From this we find: $w_{\mathrm{DE}} < -1/3$ so it does not have to be exactly -1. The current main focus of cosmology is in exploring the possibility of a varying w_{DE} as function of redshift. A simple way of describing this variation is in a linear relation as:

$$w(z) = w_0 + w_a\left(1 - \frac{1}{1+z}\right). \tag{2.18}$$

More information on these cosmological parameters, and their values, can be derived from observations, to favor or disfavor some models, as will be explained in greater detail in the next chapter (sec. 3.1).

To compare the densities described above, it is useful to define a reference quantity. For a spatially flat universe, we can define a critical value, from eq. 2.6, for the density content as:

$$\rho_{\mathrm{cr}}(t) = \frac{3H^2(t)}{8\pi G}, \tag{2.19}$$

where ρ_{cr} is called the critical density. If we now include again the possibility of a non flat universe we find that for $\rho > \rho_{\mathrm{cr}}$ the universe is closed – dominated by gravity, which will cause the collapse on itself – and for $\rho < \rho_{\mathrm{cr}}$ it is open – dominated by the expansion, while $\rho = \rho_{\mathrm{cr}}$ is for a flat universe. ρ_{cr} is therefore the quantity that distinguish the different geometry of the universe and, consequently, its destiny. Considering that H_0 is the Hubble

parameter today (at time t_0) $H_0 = \dot{a}/a\,|_{t=t_0}$ (given in units of km/s/Mpc), we have:

$$\rho_{\mathrm{cr},0} = \frac{3H_0^2}{8\pi G}, \tag{2.20}$$

for the critical density today.

Cosmologists use this scale to define dimensionless density parameters for matter, radiation and cosmological constant as follow:

$$\Omega_m = \frac{\rho_{m,0}}{\rho_{\mathrm{cr},0}};\ \Omega_r = \frac{\rho_{r,0}}{\rho_{\mathrm{cr},0}};\ \Omega_\Lambda = \frac{\rho_\Lambda}{\rho_{\mathrm{cr},0}}. \tag{2.21}$$

Using these parameters, the first Friedmann equation, eq. 2.6, becomes:

$$H^2 = \left(\frac{\dot{a}}{a}\right) = H_0^2(\Omega_r a^{-4} + \Omega_m a^{-3} + \Omega_k a^{-2} + \Omega_\Lambda) \tag{2.22}$$

with $\Omega_k = 1 - (\Omega_r + \Omega_m + \Omega_\Lambda) = -Kc^2/H_0^2$.

Different components will come to dominate eq. 2.22 at different times due to the evolution of the scale factor $a(t)$. Eq. 2.22 is analitically solvable for a flat universe ($\Omega_k = 0$) and assuming a dominating density parameter:

$$a(t) \propto \begin{cases} t^{1/2} & \text{radiation dominated} \\ t^{2/3} & \text{matter dominated} \\ e^{H_0 t} & \text{cosmological constant energy dominated.} \end{cases} \tag{2.23}$$

The behavior of the different energy densities is shown in fig. 2.1 as function of redshift. We can see that after a radiation dominated initial epoch, the universe was dominated by matter and is now by the dark energy. The most appealing physical explanation for this unknown component is vacuum energy. However, the value computed in Quantum Field Theory for such energy disagrees by ~ 120 orders of magnitude with the current critical density of our universe (Rugh and Zinkernagel, 2000). Current studies are trying to test the validity of eq. 2.18. If w_a is found to differ from zero, vacuum energy would be ruled out as the source of the accelerating universe.

2.4 Observables: distances in cosmology

In the previous sections we have outlined the formalism describing the evolution of the universe. We now have to find appropriate observables to estimate the cosmological parameters from observations.

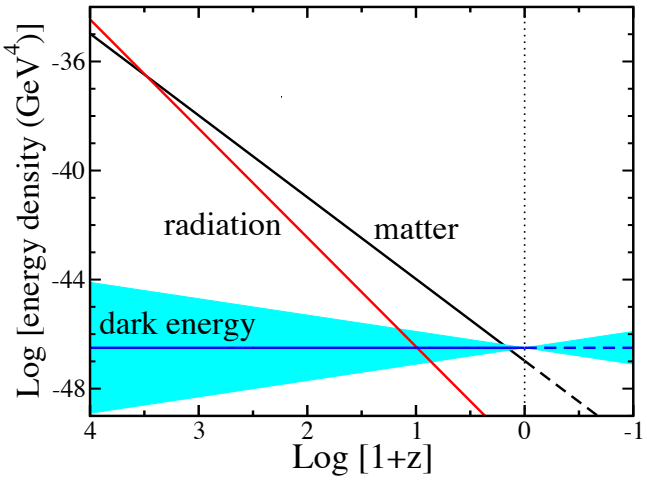

Fig. 2.1 Evolution of radiation, matter and dark energy densities with redshift. The blue area shows the different values depending on the model for dark energy. In this plot $H_0 = 100h$ km/s/Mpc ($h = 0.7$) and the convention for which g$= 5.62 \times 10^{23}$ GeV and cm$^{-1} = 1.98 \times 10^{-14}$ GeV have been used. From Frieman et al. (2008).

Since we are interested in the history of the universe, the observations concern distant objects. We have already described the cosmological redshift, z, in eq. 2.14 but this depends only on the scale factor and not directly on the cosmological parameters.

We can observe two kinds of distances: radial (or line-of-sight) and angular diameter distance (how large objects appear on the sky). The radial comoving distance d_C can be calculated by integrating over the Hubble expansion (eq. 2.22 written as function of redshift) since the time of emission at a redshift z:

$$d_C(z) = d_H \int_0^z \frac{dz'}{H(z')/H_0} = d_H \int_0^z \frac{dz'}{\sqrt{\Omega_r(1+z')^4 + \Omega_m(1+z')^3 + \Omega_k(1+z')^2 + \Omega_\Lambda}}, \tag{2.24}$$

where $d_H = c/H_0$ is the Hubble distance.

The ratio of the physical diameter, D, of an object to its apparent angular diameter, $\delta\theta$, defines the angular diameter distance d_A:

$$d_A = \frac{D}{\delta\theta}. \tag{2.25}$$

This ratio defines the separation between two objects at the same redshift (or the proper size of an object). It can be related to the transverse comoving distance by the scale factor:

$$d_A = \frac{d_M}{(1+z)}, \tag{2.26}$$

where, making use of eq. 2.4, d_M is:

$$d_M = \begin{cases} (d_H/\sqrt{|\,\Omega_k\,|})\sinh(\sqrt{|\,\Omega_k\,|}d_C/d_H), & \Omega_k > 0 \\ d_C, & \Omega_k = 0 \\ (d_H/\sqrt{|\,\Omega_k\,|})\sin(\sqrt{|\,\Omega_k\,|}d_C/d_H), & \Omega_k < 0. \end{cases} \tag{2.27}$$

d_A is used to determine the baryon acoustic oscillations scale for each redshift (see sec. 3.1.2): a category of standard ruler observed to obtain cosmological parameters constraints.

The luminosity distance d_L is another distance used with similar purpose. It is defined by the ratio of the observed flux S of a light source to its intrinsic luminosity L:

$$d_L = \sqrt{\frac{L}{(4\pi S)}}. \tag{2.28}$$

For a flat and static metric d_L and d_M would be equal. In an expanding universe, instead the flux is diluted because the photon energy diminishes and the time is diluted while the universe is expanding. Therefore the flux S is reduced by a factor $(1+z)$ in both effects leading to:

$$d_L = d_M(1+z) = d_A(1+z)^2. \tag{2.29}$$

This kind of distance is of particular interest for this thesis, since it is the one used for standard candles like Type Ia supernovae, described in the next chapter (sec. 3.2). It is therefore useful to further discuss the equations describing how to relate such distance measurements to the observed flux.

Magnitude is a common logarithmic unit to measure fluxes in astronomy. The absolute magnitude of an object is defined as:

$$M = -2.5\log_{10}\frac{L}{L_*}, \tag{2.30}$$

where $L_* \equiv 78.7\ L_\odot$ is the luminosity of the star Vega, historically used as reference, $L_\odot$ is the solar luminosity[2] and L is the intrinsic luminosity of the object. Since most of the time we do not know this intrinsic luminosity, another quantity is defined, the *apparent magnitude*:

$$m - m_* = -2.5\log_{10}\frac{f}{f_*} = -2.5\log_{10}\frac{L}{L_*}\frac{d_{L_*}^2}{d_L^2}, \tag{2.31}$$

[2] $L_\odot = 3.828 \times 10^{26}$ W.

where f_*, L_*, d_{L_*} and m_* are respectively flux, luminosity, luminosity distance and magnitude of the reference star, and f, L and d_L the observed flux, luminosity and luminosity distance of the star.

The apparent magnitude m can also be defined by comparing it to the absolute value, M, that it would have if the object were located at $d_L = 10\,\mathrm{pc}$[3]

$$\mu \equiv m - M = 5\log_{10}\frac{d_L}{10pc}. \tag{2.32}$$

The distance modulus μ is the quantity used to quantify the distances of standard candles (see sec. 3.2.3 in the next chapter). If a standard candle – object with constant M – is observed at different redshifts, we can study how μ evolves with redshift. This way through eq. 2.32 and 2.29 a set of cosmological model predictions for d_L can be tested.

Astronomical observations typically use broad-band filters (passbands wider than 30 nm), which means that their light passes through these filters and is therefore integrated in a certain range of wavelengths according to the filter transmission. The usual set of filters for the optical range consists of: U for ultra-violet (centred around 365 nm), B for blue (centred around 445 nm), V for visual (551 nm), R for red (658 nm), I for infra-red (806 nm) and Z (900 nm). An example of astronomical filters is shown in fig. 2.2 for the SDSS filter-set. All

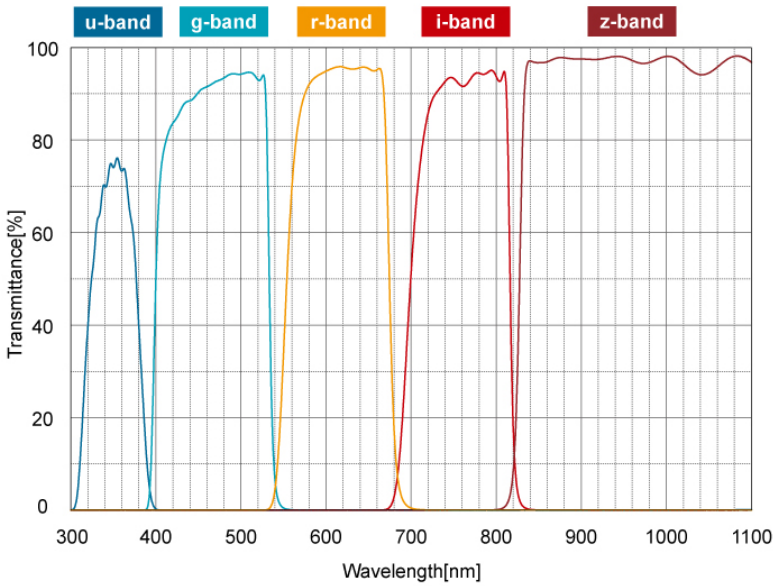

Fig. 2.2 Example of filter curves from filters produced for SDSS. In this case the effective central wavelengths are: 354, 477, 623, 762, 913 nm for u-, g-, r-, i- and z-band respectively. From http://www.asahi-spectra.com/opticalfilters/sdss.html (on the 08.01.2017).

[3] A parsec corresponds to $pc = 3.086 \times 10^{16}$ m.

the magnitudes (e.g. from eq. 2.32) observed, will be therefore integrated over these filters.

As the equation for the evolution of the universe have been laid out, we can focus, in the next chapter, on how the cosmological parameters are obtained from astronomical observations.

Chapter 3

Observational cosmology

In the previous chapter the formalism needed to explain the evolution of the universe was introduced and linked to quantities that can be measured from observations. We are now going to discuss some of these observations and their results.

3.1 Cosmological probes

We here present the major current cosmological probes: the Cosmic Microwave Background (CMB), Baryon Acoustic Oscillations (BAO) and type Ia supernovae (SN Ia). Later chapters will focus on SN Ia as their observation is the underlying science goal of this thesis.

3.1.1 Cosmic Microwave Background

In short, the CMB is a "relic radiation" from the time of recombination. According to the Big Bang theory, in the very early phases, the universe consisted of a hot and dense plasma of matter and radiation in thermal equilibrium. This plasma became colder and colder, while the universe expanded, until it reached a temperature of $T \sim 3000\,\mathrm{K}$. At this point, the energy of photons was not enough to ionize hydrogen and the thermal equilibrium was broken, allowing the formation of neutral light elements (H, He, Li). The CMB is the radiation from the last scattering photons with free electrons, when the universe was 380,000 years old (i.e. $z \sim 1100$, called the recombination time), and has propagated in and redshifted with the universe ever since.

The CMB was first detected by Penzias and Wilson (1965), and its predicted blackbody spectrum was measured with high accuracy by the COBE (Mather et al., 1994) satellite, which found a temperature of $T_{\mathrm{CMB}} = 2.726 \pm 0.010\,\mathrm{K}$. On top of the overall temperature, the CMB also shows temperature fluctuations at much smaller amplitudes. The latest results

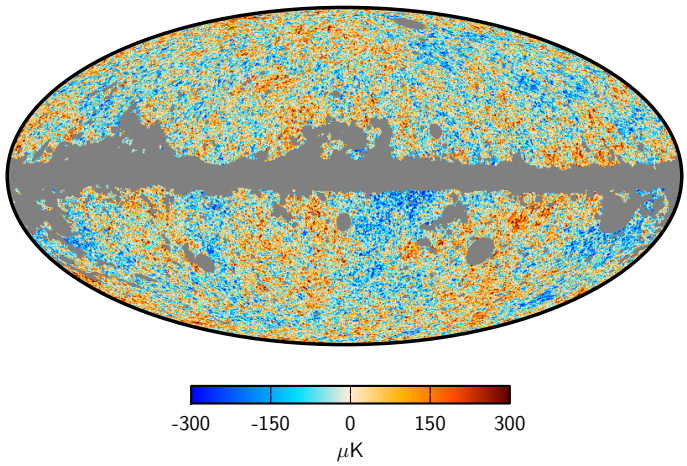

Fig. 3.1 CMB temperature map. The monopole and dipole contributions have been removed. From Planck Collaboration et al. (2016).

from the Planck mission show a CMB temperature fluctuation map of the universe with very high sensitivity and resolution, fig. 3.1.

The colder and hotter temperature fluctuations represents small anisotropies. The anisotropies were caused by the interactions between photons and barionic matter while it follows the gravitational potential wells of the dark matter. The perturbations propagated as acoustic waves in the initial plasma of matter and photons and after recombination they no longer oscillate. The CMB photons have, hence, imprinted a snapshot of the state of the fluid at that time. From the map in fig. 3.1 one can compute the power spectrum of these oscillatory mode, and the shape of its peaks is related to the content of matter of the universe. Fitting this power spectrum, Ω_k (the curvature of the universe) and Ω_b (the barionic matter content, i.e. visible matter) can be constrained and from these Ω_Λ is inferred. Some of these results are shown on the right plot of fig. 3.4 and will be discussed later.

3.1.2 Barion Acoustic Oscillations

As mentioned above, the CMB map tracks fluctuations of the photon-baryon density plasma and can be seen as a map of overdensities and underdensities of matter. These fluctuations are the seeds for formation of galaxies, stars and all the objects we can observe. The acoustic waves from which the anisotropies formed, traveled a comoving distance of about 150 Mpc before reaching the recombination and stalling. Therefore, there will be an overdensity at 150 Mpc from the original perturbation, which means that it will be slightly more probable to find a galaxy at such comoving distance from another. This BAO scale represents a standard ruler that can be used to measure the distance of objects at different redshifts. Since the

comoving distance between galaxies is constant, the physical distance becomes larger and larger while the universe expands (see eq. 2.26). Hence, measurements of the effective distances between galaxies allow to reconstruct the expansion history of the universe.

In the latest years many wide field redshift surveys, such as the 2dFGRS[1] (Colless et al., 2003) and the SDSS[2] (Alam et al., 2015), provided 3D maps of the galaxy distribution in the nearby universe. From these it is possible to find the BAO scale at each redshift (Eisenstein et al., 2007). The constraints on the cosmological parameter of interest for this thesis can be found in fig. 3.4 and will be discussed later.

3.2 Supernova cosmology

A supernova is an explosion of a star, either fully disrupting the object or leaving a small, dense remnant (neutron star or a black hole). When they explode, these objects are bright enough to be visible at very large distances and are therefore of great interest for cosmology. There are several types of supernovae which have been classified based on their spectral features. We here first discuss SN classification, after which we explain in detail how Type Ia supernova are used for cosmology.

3.2.1 Classification and origin of type Ia supernovae

The first distinction is between the SN that do not show H lines in their spectra, type I, and the ones which do, type II. Type I supernovae are further subdivided in: type Ia with strong Si II absorption lines, type Ib with He I, but no Si II, and type Ic without Si II and He I. The different spectra with their main spectral features are shown in fig. 3.2. Only SN Ia are currently used for cosmology. It is thus essential to determine the SN types. From now on we only consider type Ia.

There are two main scenarios that are believed to generate a SN Ia and both involve a thermonuclear explosion of a carbon-oxygen white dwarf (C-O WD). One of them is a binary system composed of a white dwarf (single degenerate scenario) which accretes mass from a companion (which can be a red giant). When the WD reaches and exceeds the Chandrasekhar mass limit $M_{\mathrm{Ch}} \sim 1.4 M_{\odot}$ (where $M_{\odot}$ is the mass of the Sun[3]), due to the accretion of mass, the electron degeneracy pressure is no longer able to balance the white dwarf's own gravitational self-attraction and the star collapses (Chandrasekhar, 1931). At this point the density of the core is such that an explosion is triggered initially as a subsonic deflagration that later turns into a detonation. In the second scenario the accretion of matter

[1] http://2dfgrs.net/
[2] http://sdss.org/
[3] $M_{\odot} = 1.98910^{30}$ kg.

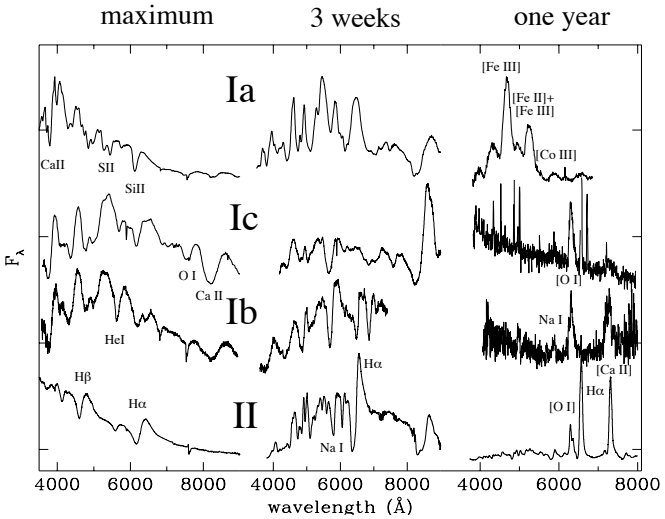

Fig. 3.2 Spectra of the main types of supernovae at three different epochs (time from explosion), and the main spectral features that distinguish them. From Turatto (2003).

would be due to two C-O WDs merging (double degenerate). However, the full explosion mechanic is not yet completely understood. There are many proposed models (Hillebrandt and Niemeyer, 2000), but they still do not fully describe the observations.

Whatever the explosion trigger is, the detonation of a "simple" C-O system creates light curves – the flux of the object as function of time – which are more similar between each other than the ones of the other subcategories of supernovae. This is what makes Type Ia supernovae particularly useful as standard candles (this concept will be further investigated in the next section). SN Ia light curves are powered by radioactive decay of elements produced during the explosion. During the thermonuclear disruption, ^{56}Ni is produced in an amount that depends on the explosion itself. For example in the well explored single degenerate scenario, the amount of Ni synthesized is found to vary between 0.18 and 0.81 $M_\odot$ (Blondin et al., 2013). The light curves are powered by energy generated as ^{56}Ni decay to ^{56}Co, which then decays to ^{56}Fe. There are also other radioactive ions produced, that come to play at the later phases.

3.2.2 Standardizable candles

We have now described how SNe Ia are classified and why they produce relatively uniform light curves. However, the maximum absolute magnitudes of SNe Ia have a scatter of about 0.4 mag that, while small for astronomical objects, corresponds to a 20% scatter in the distance measurement. With standardization this scatter can be reduced (to 0.17 mag; Hamuy et al., 1996) allowing high precision in the determination of the cosmological parameters.

The standardization is achieved empirically and it is based on two relations observed in the SN light curves: brighter-wider – the brighter the SNe appear the slower the light curves decline – and brighter-bluer – the brighter the SNe appear the less their light is affected by dust absorption.

The first relation for standardization, brighter-wider, was introduced by Phillips (1993) and it means that the slower the light curve declines (or the smaller the difference in magnitude in the B band is between peak and 15 days after it), the brighter the SN is at peak, as shown on the left-hand side plot of Figure 3.3. We also notice from the right-hand side plot that after applying the correction for this effect the scatter is reduced.

It is possible to define a color index of an astrophysical object by computing the difference in magnitude observed in two different filters. The second relation, brighter-bluer, therefore means that SNe with bluer SED, typically measured through a lower $B-V$ color, are found to be brighter. This relation is partially due to wavelength dependent extinction by dust. This effect makes the object appear redder, because bluer wavelengths are more absorbed in proportion to the amount of dust along the line of sight (Cardelli et al., 1989). To properly account for this effect, SN light curves are observed in more than one filter. Even if dust extinction can explain part of this relation, the extinction properties from SN Ia observations do not match with dust properties in the Milky Way (Hicken et al., 2009; Tripp, 1998). This suggests that part of the brighter-bluer relation is due to intrinsic effect.

There are several ways to parameterize these two relations in order to obtain the correction needed for standardization. Possible tools include SALT (Guy et al., 2005), SALT2 (Guy et al., 2007), MLCS (Riess et al., 1996) and MLCS2k2 (Jha et al., 2007). SALT2 is the one mostly used and make use of two parameters called *stretch* (x_1), which is for the brighter-wider correction, and *color* (c) for the brighter-bluer correction. In short, a time and wavelength dependent model, parametrized by x_1, is fit to the data together with an empirical color law, parametrized by c.

3.2.3 Hubble diagram

SNe Ia have already proved to be a great tool to study the evolution of the universe, since the discovery of its accelerated expansion by Perlmutter et al. (1999) and Riess et al. (1998).

After a light curve has been standardized, the distance modulus μ, defined in eq. 2.32, can be computed from the data. Using the SALT2 formalism, the distance modulus can be written as:

$$\mu \equiv m_B - \mathscr{M} + \alpha x_1 - \beta c, \tag{3.1}$$

where m_B is the light curve peak magnitude in rest-frame B band and $\mathscr{M}$, α and β are nuisance parameters which are fit together with the cosmological parameters. In $\mathscr{M}$ is also included a correction that allows a magnitude offset between the cases with high and low

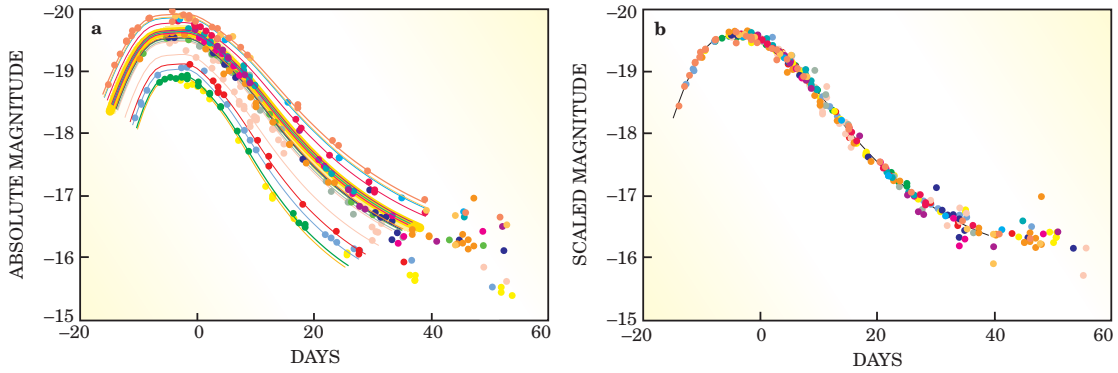

Fig. 3.3 Light curves of nearby, low-redshift type Ia supernovae, without correction (on the left), brighter-wider corrected and normalized to peak magnitude (on the right). From Perlmutter (2003).

host galaxy masses – galaxies where the SN exploded – (Childress et al., 2013; Kelly et al., 2010; Sullivan et al., 2010). From eq. 2.32 we see how the distance modulus is related to the luminosity distance, d_L, and hence to the cosmological parameters. Fitting the distance moduli from eq. 3.1 with the model from eq. 2.32, we obtain the Hubble fit which provides constraints on the cosmological parameters. This is plotted vs z in a Hubble diagram. On the left-hand side of fig. 3.4, the Hubble diagram of the joint light-curve analysis (JLA) is shown (Betoule et al., 2014). It is made with a total of 740 SNe from several low-redshift samples, high-redshift Hubble Space Telescope (HST) SNe, and from SDSS-II (Frieman et al., 2008) and SNLS (Astier et al., 2006) surveys.

Hubble diagram results

One of the goals of cosmology is to measure the equation of state parameter w. One would like to determine if its value is compatible with -1 and if it is evolving in time or constant. The models tested using the data are therefore: ΛCDM, which is a FLRW model where the acceleration is caused by a cosmological constant with $w_\Lambda = -1$, and the $wCDM$ where it is caused by dark energy with $w_{DE} < -1/3$, as previously discussed in sec. 2.3. The combination between the Hubble diagram results from the JLA sample and the other cosmological probes, such as BAO and CMB, provides more stringent constraints to the cosmological parameters. Betoule et al. (2014) find a matter density of $\Omega_m = 0.305 \pm 0.010$ and curvature consistent with zero $\Omega_k = 0.03 \pm 0.02$, and therefore the rest of the energy, $\sim$70%, is into dark energy. Fitting a flat $wCDM$ they determine $w = -1.027 \pm 0.055$ (and $\Omega_m = 0.303 \pm 0.012$), which is consistent with a cosmological constant. When they allow for an evolution of w, according to eq. 2.18, they do not find an evolution, with $w_0 = -0.957 \pm 0.124$ and $w_a = -0.336 \pm 0.552$.

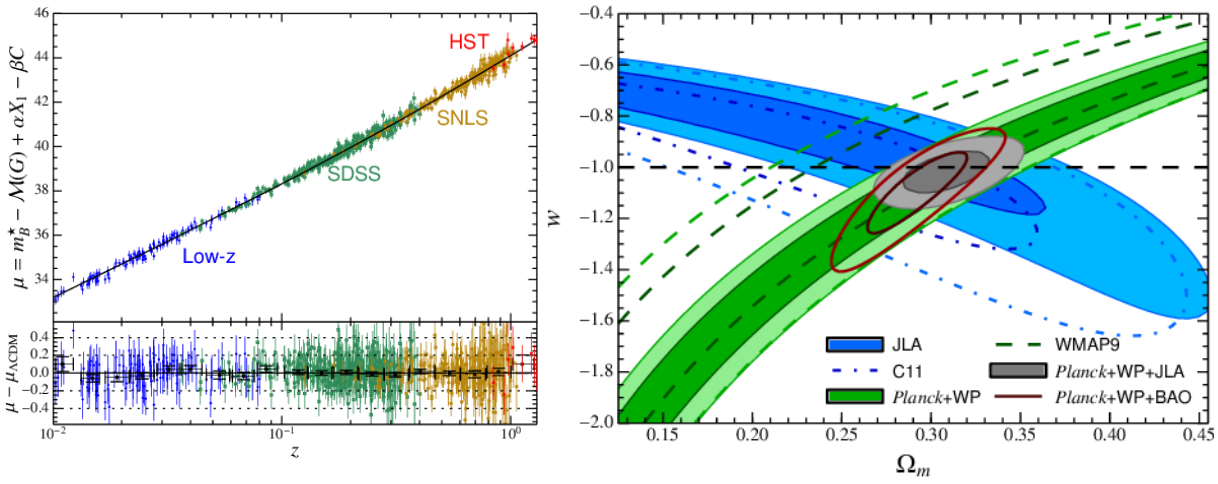

Fig. 3.4 Left: Hubble diagram of the JLA sample, with best-fit to Λ*CDM* cosmology (black line), and related residuals in the bottom. Right: Ω_m and w cosmological parameters for the flat *wCDM* illustrates the orthogonality of the results from different probes. The confidence contours are shown at 68% and 95% (including systematic uncertainty). From Betoule et al. (2014).

In the right plot of fig. 3.4, w is plotted against Ω_m using results from different probes (the CMB is noted as "Planck+WP"). From this plot we see the complementarity of these probes and the particular importance of SN Ia cosmology in the determination of w, since the CMB contours and the JLA ones are almost perpendicular to each other.

Hubble diagram systematic errors

Many are the improvements needed for better distance moduli measurements and better constraints on the cosmological parameters. In the following sections we will focus on some of these aspects and give a general overview of the current status of systematic errors for SN cosmology.

K-corrections A technical but important aspect of SNe light curve standardization is that the light observed from distant supernovae is redshifted and therefore must be shifted back to rest frame to compare their fluxes. This is further complicated since even a relatively small redshift difference means a different (rest-frame) wavelength region is measured. Thus, if one observes many objects at different redshifts, with the same filter, a correction factor must be applied to properly convert their fluxes and compare them. This correction has to be computed for each filter used for the observations and they are called *K-corrections* (Kim et al., 1996).

In fig. 3.5 we show an example of how a spectrum changes when redshifted. The dotted line in the left figure is the flux calibrated spectrum of SN2011fe observed 3 days before peak brightness (taken from Pereira et al., 2013). The black curve is the same spectrum multiplied with a generic detector efficiency in function of wavelength (in %) that rises up to 5000 Å, then is mostly constant until 6500 Å and decrease almost linearly reaching almost zero at 10000 Å. The spectrum is, hence, more suppressed in the blue side. Finally, the blue curve is the original spectrum redshifted to $z = 0.1$ and multiplied for the same detector efficiency as before. The two distorted spectra look very different from each other and this holds true even after we blueshift the blue curve so that it has the same z as the black one (right side of fig. 3.5). This happens because the SN spectra are observed in wavelength ranges where the detector has different efficiency.

In this example we considered only the simplified case where just the detector efficiency has an impact on the observed spectra. As will be explained in the next chapter, every optical element will have an influence on the transmissivity and for ground based observations one has to consider also the atmospheric extinction. Adding to this, there is an intrinsic variation in the SED of the SN Ia. In computing *K-correction*, assumptions are made for all those parameters (for the SN SED, e.g., this is usually the SALT template). As was shown in (Saunders et al., 2015), any error in these assumptions will directly propagate to systematic errors for SN cosmology. It is therefore essential to know the transmissivity of the system used to perform the observations well. These considerations become even stronger when comparing surveys that sample all the redshift ranges of the Hubble Diagram. In this case, many different instruments are compared with each other and different filters matched to each other making the error consequently bigger. Since the Hubble diagram is based on the ability to compare fluxes of SNe at different redshifts, limiting this uncertainty is a key aspect to improve SN cosmology.

As direct consequence of a mis-color-calibration (or mis-calculation of the *K-correction*), one would have a wrong estimate of the distance moduli, μ. An error of $\sim$1% on μ for high redshift SNe, would translate into an uncertainty of $\sim$2-3% on w (Amanullah et al., 2010) with respect to the case with $w = -1$. A fast and easy way to derive this result is to use several values for w and see which distance modulus value one retrieves as function of redshift for a fixed Ω_m. One can rewrite eq. 3.2 as function of w obtaining:

$$d_L(z,w) = d_H(1+z)\int_0^z \frac{dz'}{\sqrt{\Omega_m(1+z')^3 + (1-\Omega_m)(1+z')^{3(1+w)}}}, \tag{3.2}$$

where we neglected Ω_r, and compute the distance modulus for a SN at redshift z according to eq. 2.32.

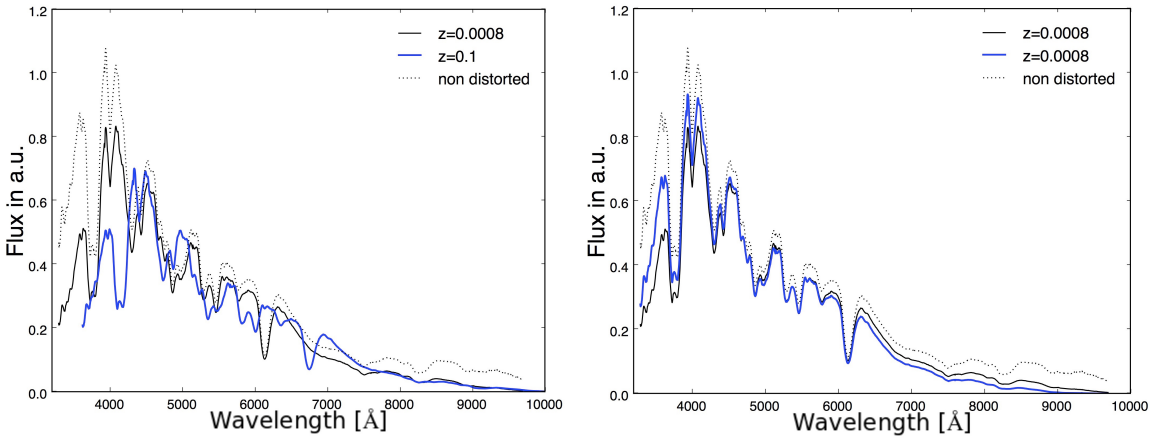

Fig. 3.5 SN2011fe spectra (from Pereira et al., 2013) at -3 days from peak brightness as it was emitted (dotted line in the left and right plot). Left: the spectra has been multiplied for a generic detector efficiency in function of wavelength (black line), and it has also been redshifted at $z = 0.1$ (blue curve) before applying the detector efficiency. Right: the dotted and black curve are the same as in the left figure, the blue curve represents the redshifted SN as it appears in the restframe ($z \simeq 0$). The difference in the three curves is due to the presence of the detector efficiency.

Low redshift sample From the Hubble diagram of the JLA sample (fig. 3.4) we also note that: there are not too many data-points in the low-redshift area. These ones are very important since they constitute the anchoring sample for the Hubble diagram and play a fundamental role in training the fitters used for standardization. Furthermore such a sample can be used to verify the homogeneity of the SNe light curves as well, checking for possible biases which would be harder to detect in a higher-z sample. Having a good anchoring sample can also significantly lower the statistical uncertainties, as exemplified in fig. 3.6 where a factor of two of improvement is reached when the nearby sample is included.

Current possibilities and limitation With almost 1000 SNe Ia observed to date, and big surveys planned to significantly increase their number, such as the Large Synoptic Survey Telescope (LSST) and the Zwicky Transient Facility (ZTF), the statistical uncertainties will be consequently reduced.

However, the dominant source of uncertainty is nowadays due to systematics. Tab. 3.1 lists the contributions to the error budget on Ω_m. The systematics contributions in the table from the second line on are mostly due to the knowledge of the astrophysical processes involved with supernovae explosions, e.g. possible bias due to differences in the brightness related to the progenitor environment (host relation), or difficulties in the classification (contamination), or in the light-curve fitter (light-curve model).

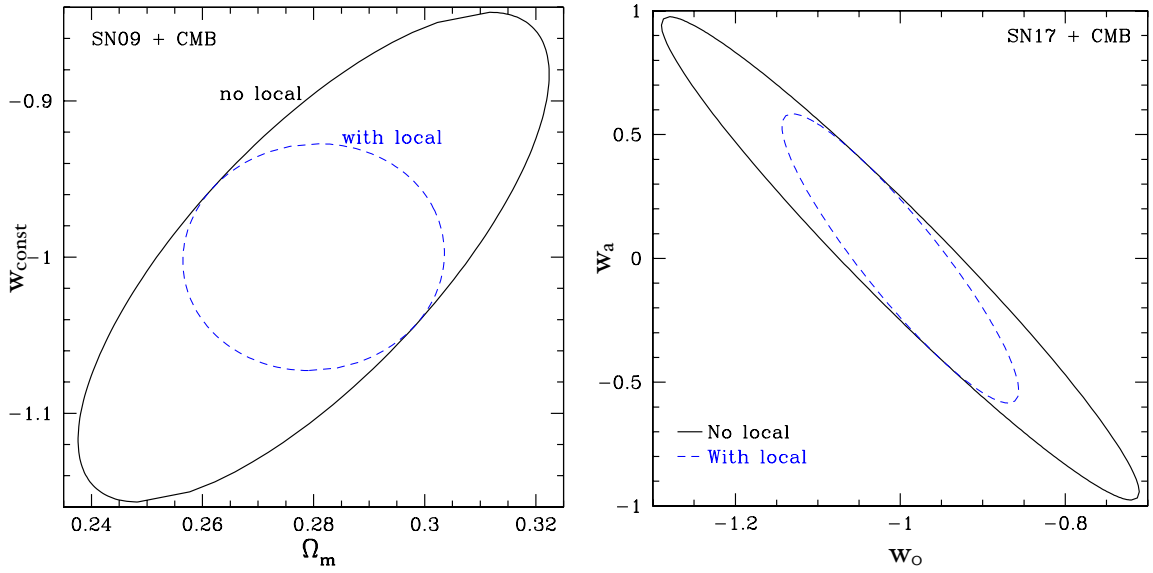

Fig. 3.6 Contours of w-Ω_m (left) from a data-set with $0.2 < z < 0.9$, and w_0-w_a (right) from a data-set with $0.2 < z < 1.7$. In both plots they are shown with and without a sample of 300 nearby SNe ($z \sim 0.05$). We see that the errors are twice smaller when the nearby sample is present. From Linder (2006).

Uncertainty sources	$\sigma_x(\Omega_m)$	% of $\sigma^2(\Omega_m)$
Calibration	0.0203	36.7
Milky Way extinction	0.0072	4.6
Light-curve model	0.0069	4.3
Bias corrections	0.0040	1.4
Host relation	0.0038	1.3
Contamination	0.0008	0.1
Peculiar velocity	0.0007	0.0
Stat	0.0241	51.6

Table 3.1 List of uncertainties on Ω_m of the JLA sample of SNe. From Betoule et al. (2014). Statistical uncertainties will decrease with Dark Energy Survey (DES) /LSST, and the error will be fully dominated by calibration systematics.

Even if these invoices are numerous they only contribute in small amount to the total error budget. The dominant component is in calibration errors, the first element of the list which accounts for $\sim$37% of the variance of Ω_m. The calibration error is itself a combination of any systematic uncertainties from the many steps where counts, on the detector, are transformed into flux observed. The importance of achieving an extremely precise calibration is therefore evident: even increasing the number of objects observed, the cosmological parameters determination will be anyway limited by this error.

It is therefore fundamental to improve the technique with which measurements are performed and build devices that help tracking down the different sources of errors and correct for them. This is the underlying motivation for this thesis work: to propose a new approach and take the first steps to implement it.

Before explaining this, we will in the next chapter describe how photometric calibration is currently performed.

Chapter 4

Calibration systematics

In astronomy, the detectors for optical light are Charge-Coupled Devices (CCDs). In this Chapter, these devices and their main characteristics are first briefly described (sec. 4.1). Then we will focus on how images acquired with CCD (hence CCD images) are reduced and the standard techniques employed for this purpose. This process will be described in steps: removing all counts from the image that do not directly belong to the science object, correcting for the instrumental artifacts that are directly caused by the set-up used for the observations (sec. 4.2) and, finally, converting the counts recorded on the image into physical flux (sec. 4.3).

4.1 Charge-Coupled Devices

Charge-Coupled Devices are arrays of silicon detectors (pixels). The functioning principle of CCDs is based on the internal photoelectric effect, which causes the production of electron-hole pairs within the semiconductor when it is hit by electromagnetic radiation within a certain frequency range. Silicon responds to photons with wavelengths between 3000 and 11000 Å. The pixel structure allows to hold the electrons in potential wells until *readout*. To measure the amount of charge in each pixel, they have to be transported across the full detector surface to an output amplifier, which is usually located at one of the four corners of the detector surface (or at each corner).

The charge packet transport across the detector surface is due to potential barriers applied to the pixels. By changing their voltages, charges can be transported from one pixel to the other during what is called parallel shift. The whole "charge image" is shifted by one row at a time which brings the lowest row into the output shift register (or serial register), that is just another row of pixels hidden from illumination. Before the parallel shift occurs again, each pixel in the serial register is shifted out in the output electronics. This whole process is schematized in fig. 4.1 using the famous analogy of CCD pixels with water buckets.

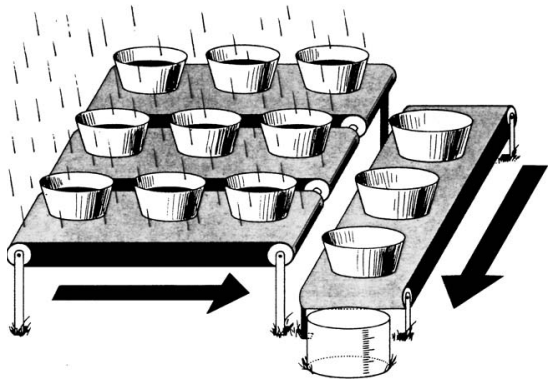

Fig. 4.1 Basic functioning of charge transfer for a CCD. We see the analogy of pixels with water buckets that unload their water content in the serial register buckets. Each of the serial register bucket, then, unloads the water in the final bucket that can measure the water collected. From Janesick and Blouke (1987).

At the amplifier, charge packets are converted to voltage. Amplification of these signals and conversion to digital numbers occurs in the CCD control electronics. The longer a CCD is illuminated, the more charges it accumulates. The illumination is regulated by a shutter (mechanical or electronic).

Two characteristic quantity describing a CCD detector are the Gain and Quantum Efficiency (QE). The former determines how the amount of charge collected in each pixel will be assigned to a digital number in the image, given in e^-/ADU (Analog to Digital Unit). The QE is the chip's ability to detect light: it is the ratio of produced electrons to the number of photons hitting the detector surface and depends on the wavelength of the incoming radiation. An example of CCD QE is presented in fig. 4.2 where we see that it is lower for small and large wavelengths (up to 4000 Å and from 8000 to 10000 Å), reaching a maximum around 5000-6000 Å.

4.2 Step one: extra counts removal and instrumental artifacts correction

A CCD image, unfortunately, does not only show the counts from the science object, but also extra counts, e.g., due to non-uniformity of the detector or the readout technique itself.

4.2.1 Image reduction

In order to properly account for and remove these effects, several steps are needed during the image *reduction* of CCD frames:

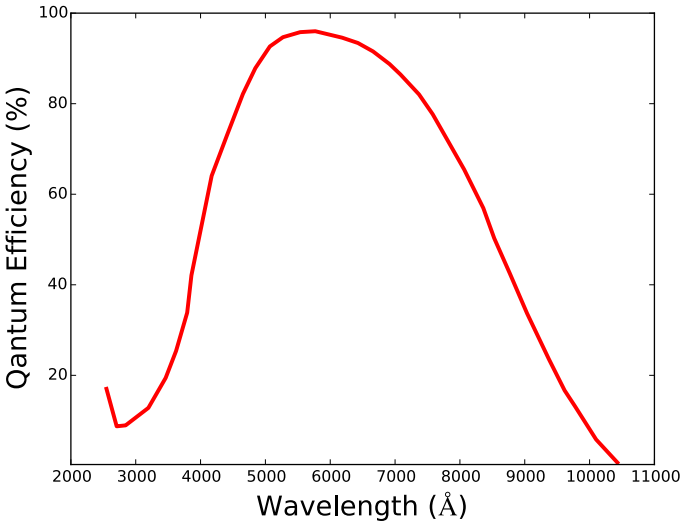

Fig. 4.2 Example of CCD Quantum Efficiency curve for an e2v CCD, from http://www.e2v.com/products/imaging/qe-curves/ (08.01.2017). The curve can be different depending on the model and producer, and sometimes between chips from the same batch.

- bias and dark subtraction;
- flat fielding;
- fringing correction;
- sky background subtraction.

In the following paragraphs, these steps are explained as applied to imagers. For spectrographs data reduction, the bias, dark and flat field steps are performed in an equivalent way. Fringing and sky background removal are obtained in a different way. These and the other additional steps required for spectrographs will be detailed in sec. 5.2 specifically for the case of SNIFS – the spectrograph used for this thesis work.

Bias and dark subtraction For each image acquired, the CCD electronics are set up to provide a positive offset value called the bias level, which prevents from recording negative numbers at the analog-to-digital converter (ADC). This level will, however, not be exactly constant for each pixel. There are two common processes that are used to evaluate it: bias frames and overscan regions.

Bias frames are made by exposing the CCD for 0 seconds with the CCD shutter closed. Ten or more bias frames are combined, and their median frame can be subtracted from all other images to create a proper bias-corrected image. The median bias frame is free from cosmic rays, that appear as brighter or saturated pixels, and random fluctuations that would

appear in a single bias frame. The bias frames represent any two-dimensional structure in the bias level.

Overscan strips are produced with every readout of a CCD frame, and are additional columns and/or rows of pixels located next to the exposed frame but not exposed to light. These pixels hence give information about the bias level in each frame, and are important when dealing with a CCD camera known to have a varying bias level. As the bias level varies throughout the day, the median value of the overscan stripes must be subtracted from all images first, including the individual bias frames. The overscan strips are then cut away from all frames (the frames are "trimmed").

Dark frames are also exposures acquired with the shutter closed, but the CCD is "exposed" for a time period equal to the longest exposure time used in the science images. These frames measure the dark current in the CCD. Dark current is due to the thermal agitation of the electrons within the semiconductor. This agitation can free the electrons which are, hence, collected in the potential wells of the pixels, becoming indistinguishable from the charges due to a direct illumination. The dark current has a strong dependence on the temperature. As CCDs are usually cooled with liquid nitrogen (LN2) a good camera reach temperatures in which the dark current is essentially negligible, which means that the need of dark frames strongly depends on the camera in use.

Flat fielding Each pixel in a CCD has a slightly different QE (mentioned in sec. 4.1) value compared to its neighbors. Flat field images are used to take these differences into account and *flatten* the relative response of each pixel. The next section (4.2.2) will be entirely devoted to discuss this basic concept and techniques for flat fielding, since it is a very complex task and extremely important for the purpose of this thesis work.

Fringing Photons with longer wavelengths might be reflected within a CCD chip, instead of absorbed by the silicon layer, and cause interference with the incoming radiation. This translates into a wave pattern due to constructive or destructive interference on the CCD chip. This phenomenon known as fringing is mainly visible for infra-red (IR) wavelengths. It is possible to create a model to remove this effect from the image data (it is an additive effect for the imagers). Fringes in spectrographs, instead, modulate the detection efficiency depending on the wavelength and can be removed by applying the flat field (it is a multiplicative effect for spectrographs).

By applying these corrections according to:

$$\text{corrected image} = \frac{\text{raw image}_1 - \text{overscan}_1 - (\text{bias}_2 - \text{overscan}_2)}{\text{flat field}_3 - \text{overscan}_3 - (\text{bias}_2 - \text{overscan}_2)}, \tag{4.1}$$

and masking out bad pixels and columns, which are either saturated or dead, it is possible to considerably reduce the impact of miscounting due to artifacts in the camera used. The index 1, 2, and 3 in eq. 4.1 indicate the type of image – science, bias or flat field – and the overscan value belonging to it.

Sky background subtraction Even if the night sky is mostly dark, there are still counts, in the empty part of the sky, that might belong to unresolved sources, scattered light by the Moon, emissions from N_2, O_2 and OH. These extra counts are also overlapping with the science object and have to be removed. One way to do that is to select some pixels (few hundreds) around the object and use their values to compute an average sky background. This is then subtracted from the total number of counts in the science object.

4.2.2 Flat fielding techniques

As previously mentioned, flat fields corrects for the different QE of each pixel. However, they do not only monitor the CCDs response. The CCD chip is in fact the last part of a complex optical system: in case of astronomical observation, we also have a telescope (with primary, secondary and, possibly, tertiary mirrors) and likely several additional correcting optical elements. Usually there are also filters, to perform observations in many wavelength bands, as mentioned in sec. 3.2.2, or spectrographs.

Every optical surface the light crosses will have an effect on the image produced on the CCD, modifying the way the flat fielding image would look. It is, however, difficult to disentangle the contribution of each one of them, since they will overlap in the final image. Sometimes dust grains stick to the optical surfaces, such as mirrors, lenses, filters, entrance windows and even CCD chips, and absorb part of the light creating "donut" like darker regions on the images. One can use the flat field to remove these features too, since they appear in the science exposure and in the flat field images.

An example of that is in fig. 4.3, where in the upper left image we notice the darker corners, due to vignetting – reduction of brightness in the edges of the image with respect to the center – and the presence of donut regions, due to dust grains, on the image. These are corrected by applying the flat field (lower left image), usually normalized to 1, to have a resulting corrected image on the right. A flat field is therefore essential to correct for all these effects and its importance becomes even more evident when considering that the object of interest, in the science image, might lay below one of these features, thus leading to a wrong estimate of its counts.

Ideally, a flat field is a uniform illumination of the CCD such that every pixel sees the same amount of light. Any measured difference between pixels would then be due to the characteristics of the pixels themselves. As seen above in fig. 4.2, the QE of CCDs depends

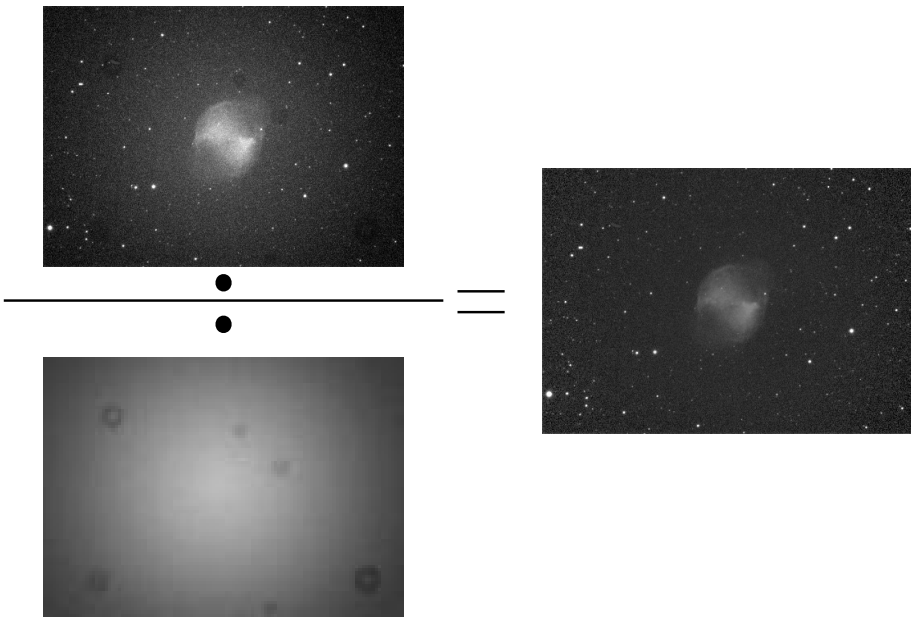

Fig. 4.3 Upper left: science image. Lower left: flat fielding image. Right: corrected image resulting from the ratio of the science image and the flat field. The images are from http://www.astropix.it/appunti/ripresa-ccd.html (at the 08.01.2017).

on wavelength and different filters have different sensitivities. It is, therefore, necessary to produce these calibration images in several bands.

An even more ideal flat field has another important characteristic: it should illuminate the system – telescope+instrument – in the same way as the science object, so that the optical path of the light is the same in both cases. Hence, there is no scattered light detected which is not present in the science observation as well, and the calibration is not contaminated by any artificial effect introduced by the flat field itself.

Standard techniques

Building a calibration system that can illuminate the entire field of view and mimic the science cases is extremely difficult. This ideal system should illuminate the entire primary mirror of a telescope (few meters) as a star would, i.e. parallel beam. However for practical reasons the flat field system has to be at a finite distance from the telescope, since it would be placed in the dome. The standard technique for flat fields are based on illumination of white *screens* with lamps. Such screens scatter light in all directions and are observed by the telescope. In the flat field image of fig. 4.3, for example, a white fabric was illuminated from the back. This technique has evident limitations since it is very difficult to predict the real uniformity with which the screen scatters the light. Furthermore, the random light produces

stray light in the optics of the instrument, generating unwanted ghosts – internal reflections on optical surfaces – and features difficult to eliminate.

A visual summary of the flat fielding techniques compared to the science case is shown in fig. 4.4. Even if features like ghosts can be present in science images as well, from fig. 4.4, we easily see that the optical path of the standard flat field is very different from the one of the science object, and, therefore, the ghosts in the flat field might be brighter and in different places, leading to a wrong correction.

Additionally, the Spectral Energy Distribution (SED) of the scattered light is usually unknown and possibly very different from the science object one, making the color calibration (calibration as function of wavelengths) precision difficult to evaluate.

It is thus extremely important to have a calibration source with known SED, or at least very similar to the science object, because it weights the spectral features of the instrumental response. For example: imagine we are observing a calibration lamp whose spectrum has some emission lines in a certain wavelength range where the filter used is sensitive. We don't know its SED and we just consider it continuum. With the same system, we now observe a science object which has no emission lines in that wavelength region. When we flat field the science image with the calibrating image obtained before, we scale it with a wrong number by assigning to the system used for observation an incorrect transmissivity as function of wavelength. If we want to observe the same object with many filters, having every time a different offset, the color calibration of these measurements will have large systematics.

The same kind of consideration holds for another typical flat field technique: the *twilight flats*. Astronomers sometimes observe the sky just after sunset and before sunrise, during the brief period when the stars are not visible and the sky is relatively uniform, to obtain flat fielding images. This is again a scattered light source which can create artifacts and has an unknown spectrum. Again, this makes any precise color calibration very hard as also in this case the science object spectrum is different from the twilight one.

Another method, the *star flats*, can be used to build corrections for large scale variations on the detector plane. A star flat is obtained by observations of crowded fields (patches of sky with many stars) dithering the exposures (moving the telescope to have a new image where the star positions are shifted with respect to the previous one) in such a way that the (nonvariable) stars are observed across the entire field of view of the instrument. This operation has to be performed for each filter used for observations, and the measured brightness at different positions can be used to map the instrumental response over large detector scales. This technique is, for example, used by Betoule et al. (2013) to calibrate the MegaCam imager, allowing a correction to the twilight flat depending on the distance from the center of the image. Even if these flat field corrections are telescope time-consuming, they can be performed just a few times per year, under the assumption that the calibrated

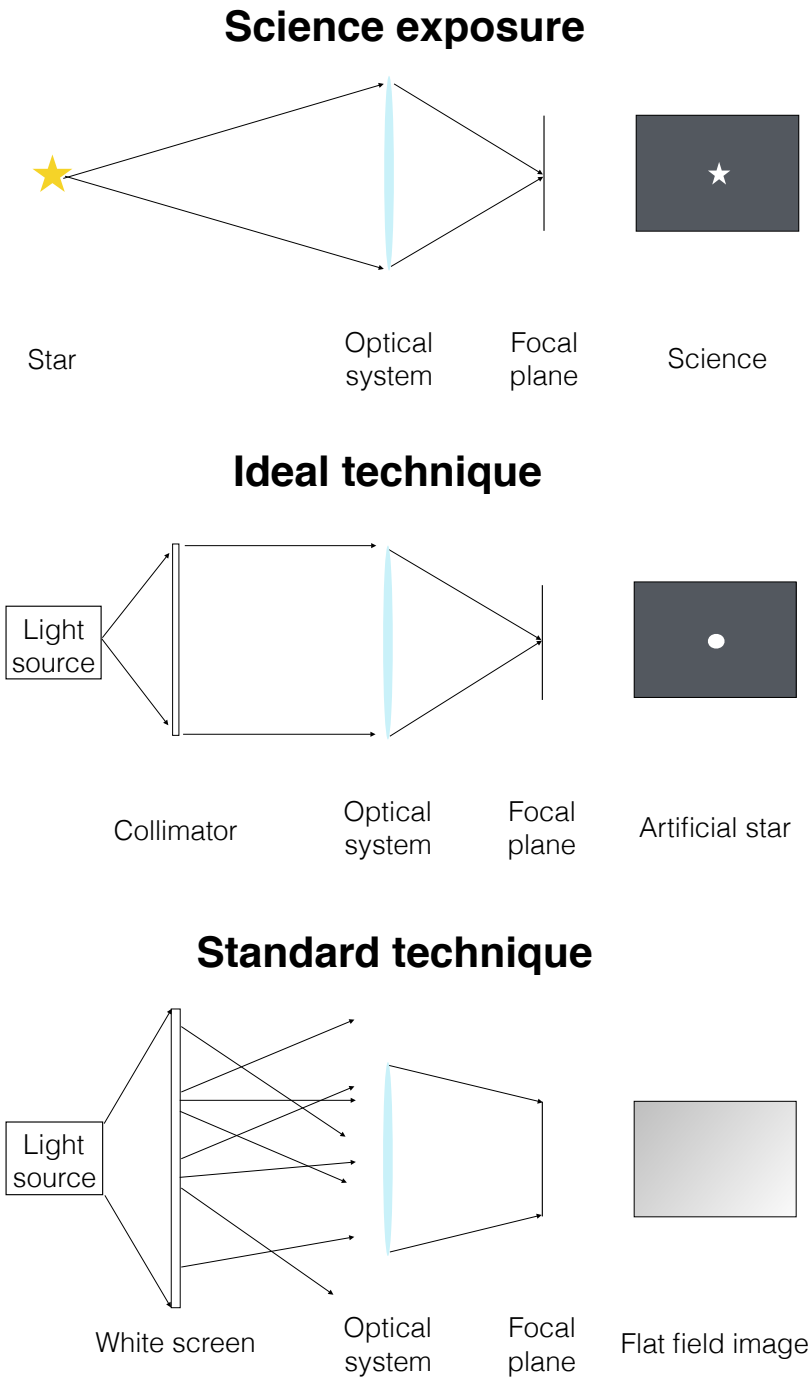

Fig. 4.4 Top: a star, at infinite distance, illuminates an optical system which focuses the light into a spot on the CCD chip generating the image on the right side. Middle: ideal flat field, it mimics the science image producing an artificial star. Bottom: standard flat fielding technique performed with a screen that scatters the light in all directions.

system is stable over long time scales (years). In that case, the twilight flats would correct all the other variations on a night-by-night basis and on small pixel-scales.

Once the initial reduction steps have been performed and the flat field has been applied to the science image, as in eq. 4.1, we can finally assume that the counts on the CCD belong to the science objects in the image, assuming that the previous steps were correct. The next step is to convert the counts into fluxes.

Ideal flat field To summarize, these are the characteristics of an ideal flat field:

- same light path of the science objects;
- same SED of the science object;
- not too time consuming, or allows calibration during daytime.

4.3 Step two: flux calibration

After ensuring that each exposure has a constant sensitivity, the next step is to convert the observed quantities, i.e. counts or electrons, to physical quantities such as fluxes. A way to perform this step is observing a non-variable star of known Spectral Energy Distribution (SED). If we observe a standard star of known flux F and measure J electrons per second (the Gain of the CCD has already been applied to convert counts in number of electrons) with a spectrograph – as we are, for this example, interested in observing its spectrum – we obtain the response of the instrument as $S = F/J$. We then use the same instrument to observe a science object, with j electrons per second. The relation $f = Sj$ gives the flux, f, of the object. In this case we implicitly assumed that the reference flux F is known with the same spectral resolution of the measurements performed, and that the system is linear (direct proportionality between counts and flux) and stable. This is very far from being as trivial as it first might sound, as knowing a star's SED with the precision required is rather hard.

To understand why, we first need to make a more general distinction between the categories of flux standards: there are primary and secondary flux standards. The primary are sources calibrated against calibrators whose properties can be described by basic physics, such as black-bodies[1] or stellar atmosphere models whose errors are limited only by the knowledge of the physics involved. The primary standards are also quite bright. The secondary standards are calibrated against the primary and are usually fainter, to be closer to the science objects and not saturate the instruments used.

[1]The power radiated per unit area of emitting surface in the normal direction, per unit solid angle and per unit frequency is described by the equation: $I_\nu = \frac{2h\nu^3}{c^2}\frac{1}{e^{h\nu/kT}-1}$, where h is the Planck constant, c is the speed of light and k is the Boltzmann constant. It is characterized by the temperature T (for the shape of the spectrum) and the area of the cavity aperture which sets its absolute flux.

4.3.1 Past lab standards and comparison with primary standard stars

The star originally assumed as primary standard is Vega (Alpha Lyrae), and there have been many observational campaign to obtain absolute flux calibrated measurements of its spectrum. Some of these, in the optical wavelength range, involved the usage of laboratory flux standards based on calibrated black-body cavities and Tungsten ribbon filament lamps, whose main property was that their spectrum was considered known. Such lab standards were calibrated by different standards laboratories one of which was the National Bureau of Standards (NBS), today known as National Institute of Standards and Technology (NIST).

The experiments were usually planned as follows: the calibrated light source was mounted at a known large distance (few km) from the telescope used for observations, during the same night observations of both the laboratory standard and of the stars to calibrate were performed. Oke and Schild (1970), Hayes (1970) and Hayes and Latham (1975) produced several independent measurements of the flux of Vega for different wavelengths with this method, obtaining an averaged value at 5556 Å of $3.39 \times 10^{-9}\,\mathrm{erg\,cm^{-2}\,s^{-1}\,\AA^{-1}}$ with a precision of 2%. The biggest source of uncertainties was due to the atmospheric extinction correction applied to the measurements.

However, with the technological development of the last decades and the increase in sensitivity of modern telescopes, fainter objects are easily accessed, and observations of Vega are difficult because of its high brightness (it saturates the detectors). Additionally, even if it is still considered the primary standard (at least from visible wavelengths up to NIR), its non-variability has still to be proven through observations. As consequence of all of this, it is essential to find other primary flux standards.

4.3.2 Today's primary star and standard star network

There have been many attempts to define other primary standard stars. Computing models of stellar atmospheres is less complicated when dealing with only one element. Therefore Holberg et al. (1986) and Finley et al. (1990) proposed to use atmospheric models of pure hydrogen White Dwarfs (WD) to refine the UV calibration of the International Ultraviolet Explorer Satellite (IUE). These models, and subsequently updated versions with non-local thermal equilibrium model atmospheres' (NLTE, Rauch et al., 2013), were used to perform the calibration of the instruments on board of the Hubble Space Telescope (HST). Using a satellite to observe stars has the advantage of eliminating the error from the terrestrial atmospheric extinction.

Three WDs were selected as primary flux standards: G191B2B, GD153 and GD71. Observations of these three standards, together with their NLTE models, provided the relative calibration, as function of wavelengths, of the STIS and other instruments on the HST. Their absolute flux level is obtained from the spectrophotometry of Vega (Bohlin, 2007; Bohlin

and Gilliland, 2004), measured with the same instrument and compared to the WDs, and its absolute flux at 5556 Å of 3.44×10^{-9} erg cm^{-2} s^{-1} Å^{-1} (with an uncertainty of 0.5%, Bohlin, 2014). A possible source of error in this methodology would arise if the response of the instrument is non linear over the large range of magnitude required to observe the WDs and Vega (about $\sim 4 \cdot 10^5$ in flux), for which there is currently no evidence, and if Vega is variable.

After having calibrated the HST instruments in this way, many other stars – selected to be the secondary flux standards – have been observed with the same instruments and thus calibrated against those three primaries. These secondary stars, which together with the primary form the standard star network, are necessary, since there are just three primaries and they are not always visible everywhere on Earth. Furthermore, it is very important to calibrate the science object against stars with similar magnitudes and SEDs, as detectors often have some amount of non-linearity or color error. Ideally one should observe the secondary stars in the same image where the science object is, but as their number is also limited, this is not always possible.

The CALSPEC[2] archive contains the spectra of the standard star network from HST observations, including the models of the three primary stars. It is currently the best set of flux standards available and it is the most used one. Modern surveys observing SNe Ia for cosmological studies are calibrated against the CALSPEC standard star network. Since SN cosmology is based on comparison between fluxes in different wavelength ranges (sec. 3.2), depending on the redshift of the object, we see that the CALSPEC color calibration is fundamental to reducing the systematic uncertainties. It is very difficult, however, to estimate the error in the models of NLTE of the primary standards precisely, and any error into the calibration chain is propagated to the next steps.

In many cases, for imaging surveys, the calibration chain does not end with the secondary standard stars, but continues to tertiary stars. These stars are observed in the same field as the science object and their fluxes are compared to the ones from other surveys (typically SDSS because of its extended standard star catalog and precise calibration), which, in turn, have been calibrated against HST primary and secondary stars. The comparison of the tertiaries with their reference values provides what is called *zero point*, *zp*, correction, for each image. This *zp*, computed for each filter used, has to be applied to the measured science object magnitude and represent a correction for instrumental response (it is an absolute scaling in flux space). The color calibration of the instrument would, hence, depend on the different SEDs of the tertiary stars used, which might be very different from the science object ones. The SEDs would in fact act as weighting function for the instrumental response spectral features as explained already in sec. 4.2.2. Therefore, the web of the error propagation on

[2]http://www.stsci.edu/hst/observatory/crds/calspec.html

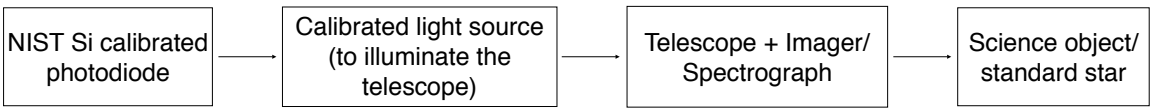

Fig. 4.5 Metrology chain to transport the NIST calibration to the imager or spectrograph, with which standard stars and science objects are observed.

the calibration chain, mentioned above, is usually more extended and complicated (and, as mentioned, contributes to 36.7% on the variance of Ω_m for the JLA).

The precision of the absolute physical flux measurable with modern laboratory standards can be lower than 1%. It would be in principle possible to verify the NLTE model precision by relating the stars calibration to such flux laboratory standards, or eliminate the need for primary standard stars (since in the case of SN Ia observations only color calibration matters). Even if the current WD models are absolutely accurate, reducing systematic uncertainties in SN Ia cosmology requires us to prove that this is the case.

The advancements in precision for laboratory fluxes, together with the consideration that with modern telescopes and photometric technique one can achieve a measurement of flux of bright non-variable stars with repeatability (obtained with current flat fielding techniques) better than 0.6% (Astier et al., 2013; Betoule et al., 2013), would in principle allow a 1% photometry precision. This has been set as the goal for next decade photometric surveys to lower the uncertainty in SN Ia cosmology (discussed in sec. 3.2.3) and improve the cosmological constraints.

4.3.3 Modern laboratory standards

NIST calibrates several flux standards traceable to a Primary Optical Watt Radiometer (POWR). This primary standard relates optical power to well defined electrical power, by comparing the temperature increase due to the light absorbed in a 100% absorbing light trap to the one needed to cause the same rise by heating up a resistor with current (Larason and Houston, 2008). The precision reached for the final products, Si photodiodes in the case of interest for this thesis work, is around 0.2% in the wavelength range 2000-10000 Å. The main goal of the calibration efforts, can be summarized by the scheme in fig. 4.5. Ideally, one would like to transfer such precise absolute calibration from NIST standards to a light source used to illuminate the telescope. With this source one calibrates the telescope and the instrument (imager or spectrograph), and then with such a calibrated system it would be possible to refine the calibration of the standard star network and/or the science object directly. For ground-based surveys one has the difficulty of additionally computing the atmospheric extinction with high precision, in order to recalibrate the objects of interest.

Several calibration devices have been built in the past years to provide in-situ measurements of the passband shapes, mostly featuring a diffusive screen illuminated by a lamp-monochromator system or tunable laser (Marshall et al., 2013; Stubbs et al., 2007, 2010), constantly monitored by a NIST calibrated photodiode. These systems have the big advantage of illuminating the entire entrance pupil at once as well as producing enough light to keep the calibration time short, thus, allowing their usage on a daily basis. However the amount of stray light produced is often very difficult to correct for and, with screen non-uniformity, constitute the limiting factor of these systems (precision around 5%).

Regnault et al. (2015) have built a device (SNDICE) that produces a quasi parallel beam in the focal plane of the telescope, by illuminating one small region of the telescope pupil at a time. Their goal is to transfer the NIST calibration to the MegaCam imager and with this calibrated system, recalibrate the CALSPEC standard star network to close the metrology chain. This system is highly stable and controllable. The extended and diverging beam produced, however, generates chromatic ghosts, the removal of which can be challenging. Currently these are being investigated through demanding ray-tracing simulations - it is still unclear whether these will be accurate enough to remove the ghosts sufficiently. However, even with a perfectly calibrated system the recalibration of standard stars will only be valid for the MegaCam imager at that time since the stars SEDs is integrated in the filters bandpasses. This consideration holds for all imaging surveys. An imager, in fact, produces images of the field observed using different filters, which means that the spectra of the sources are observed already integrated over a certain wavelength range (specific for the filter used). Even knowing the exact spectral behavior of the filters and of the whole system used for the observations, it would not be possible to reconstruct all the spectral features (emission and absorption lines) of the standard star spectrum.The recalibrated star spectrum would thus be different for different instruments (with different filter curves, etc.) and at a different time for the same instrument, in case the filter has degraded and/or changed

Albert (2012) focuses on a more radical approach where the new flux standards are built onto balloons or satellites to calibrate several telescopes with only one system. This approach has another interesting advantage: the possibility to calibrate the atmospheric extinction at the same time which is, for ground based telescopes, another source of uncertainties in the flux calibration. The flat field produced by this system will be closer to the ideal one mentioned in sec. 4.2.2 (as it is an artificial star), but it will not be able to produce an uniform illumination of the detectors to calibrate. Thus, this means that one would have to illuminate with this device every region of the instrument where the image of the science objects will lie.

One way to completely avoid atmospheric extinction is to build a small telescope with spectrograph and imager, fully calibrate it against NIST standard in the lab, and deploy it in space to observe a set of standard stars. This is the current plan for the Absolute Color

Calibration Experiment for Standard Stars (ACCESS Kaiser and Access Team, 2016; Kaiser et al., 2008) which will cover a wavelength range of 3500-17000 Å with an accuracy goal of 1%. Unfortunately, it will be able to observe just few stars as bright as Sirius (lowest observable magnitude 9.5 mag in V), too bright for future surveys such as LSST.

All the calibration devices described above provide not only a laboratory flux standard to obtain color calibration, but also a finer flat field. With such systems one can, in principle, produce a flat fielded and flux calibrated image in one step. The goal of this thesis work is to provide an alternative device to refine the standard star network. A reader interested in more information regarding astronomical flux standards can find them in the reviews from Bohlin et al. (2014) and Deustua et al. (2013).

Ideal flat field with flux calibration To summarize this section we can just say that an ideal flux calibration source is one for which its SED is known better than the precision level of the flux calibration goal. The perfect calibration device would provide both flat field and flux calibration at the same time. Its characteristics are similar to the ones of the ideal flat field:

1. illuminates the detector uniformly both spectrally and spatially;
2. same light path of the science objects (as alternative to 1 and preferred to it);
3. known SED (in case of spectral non-uniformity);
4. highly stable (over time) or has a monitoring system;
5. not too time consuming, or allows calibration during daytime.

If one would like to produce calibrated flux measurements that can be used by every other surveys, then we have to add an item to the list: one would have to build this calibration device for a spectrograph. Based on these, we designed SCALA, the only device that can potentially address all these goals. Before detailing how, we will in the next chapter describe the telescope instrument used, SNIFS.

Chapter 5

The Nearby SNfactory project and SNIFS

The Nearby Supernova factory (SNfactory) was created with this purpose: observing many SNe Ia at low redhift range, $0.03 < z < 0.1$, to provide an anchoring sample for cosmological studies and to improve SN standardization. The greatest difference to other surveys is that this one employs an Integral Field Spectrograph (IFS, sec. 5.1), which allows a set of new and different studies, as described in sec. 5.3. An IFS allows, for example, to have at the same time spectral and spatial information of the field observed. Also the study of the SN spectral features and their evolution through the full light curve is allowed by an IFS. All these qualities, which will be better described in sec. 5.3, make this kind of instruments very interesting, also in the case one wishes to obtain calibrated standard star spectra, as for this thesis.

5.1 SNIFS design and characteristics

The Supernova Integral Field Spectrograph (SNIFS, Lantz et al., 2004), located at the direct bent Cassegrain port of the University of Hawaii 2.2 m telescope (UH88), consists of three channels: two spectroscopic (blue and red, respectively) and one imaging[1]. The dual-channel spectrograph simultaneously covers 3200–5200 Å (*B*-channel) and 5100–10 000 Å (*R*-channel) with standard deviation values of the line spread function of 2.22 and 3.07 Å respectively.

The spectrograph samples a 6.4" $\times$ 6.4" field-of-view through a combination of a micro lens array made of 15$\times$15 lenses, a collimator, a grism and a camera. Each of the 225 0.43" $\times$ 0.43" spatial elements is called a *spaxel*. In fig. 5.1 a schematic representation of

[1] It is called imaging, and not photometric, because the images are not calibrated

SNIFS is shown, and, in the following subsection, its working principle and its main data products will be described. In the bottom figure of fig. 5.1 we can see the pick-off prism (called pick-off mirror in the image). This is the element that redirects part of the light (the 6.4" $\times$ 6.4" field-of-view) towards the spectroscopic dual channel. This light would otherwise reach the imaging channel. On the left hand side of the pick-off prism is the calibration unit, composed of two lamps used in combination with an integrating sphere to mimic the entrance pupil of the telescope and illuminate the spectrograph. These lamps, arc and continuum are necessary to ensure a proper calibration of the spectrographic channel, as detailed in sec. 5.2. The imaging channel covers a $9.4' \times 9.4'$ field-of-view with two CCDs. It is equipped with a filter wheel containing *ugriz* (SDSS-like, fig. 2.2) filters, a pin-hole grid, a multiple-band filter, which is a mosaic of filters – centered at 4000, 5900, 7250, 8500 and 9500 Å – covering the area of one of the CCDs and a V filter covering the remaining CCD. In regular SNIFS observations, the filter-wheel is set on the multiple-band filter + V filter and the non-calibrated photometric images are used for guiding and relative flux calibration during non-photometric nights – when the atmospheric trasmission is variable during the night because of, e.g., clouds. As discussed in sec. 10.2, in the context of this analysis, we also use the imaging channel for systematic tests of SCALA.

The working principle of SNIFS is illustrated in fig. 5.2 where we see two objects observed in the focal plane. After crossing the enlarger doublet, the dichroic mirror and the field doublet, the light passes through the micro lens array which splits the field of view in 225 elements (spaxels). The light from each lens is then dispersed by a grism and focused on the CCD, where all the 225 spectra are visible as vertical lines. Using an optical model that maps the wavelengths belonging to each spaxel on the CCD, the pipeline software is able to reconstruct the spatial and spectral distribution of the light (like it was in the focal plane of the telescope) assigning to each spaxel the correct spectrum. The end product is a *datacube* in which there is an image of the field observed for each wavelength.

5.2 Current calibration pipeline and atmospheric extinction

The pipeline for processing the data and transforming the CCD images into datacubes is a complex net of scripts, mostly developed and updated since the beginning of the SNfactory project by Dr Yannick Copin (Copin, 2013). Since the main goal of this thesis work is to build and to characterize a calibration device for SNIFS, understanding the steps and the data produced by this pipeline was required and several pipeline steps needed significant modifications to process SCALA observations. The SNIFS calibration pipeline is shortly described in the following section.

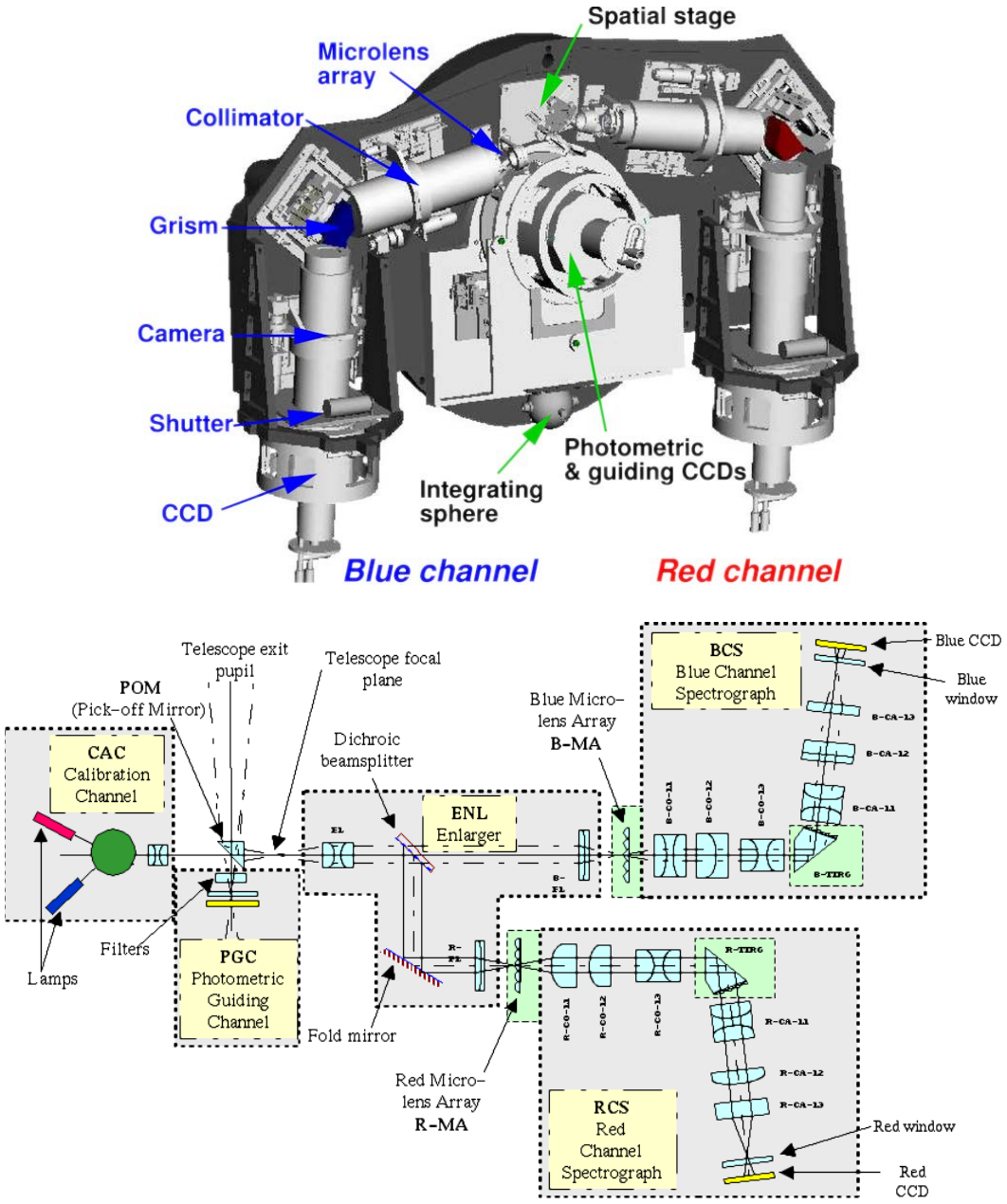

Fig. 5.1 Top: general schematic for SNIFS. From Pereira et al. (2013). Bottom: detailed schematic for the SNIFS optics. From Copin (2013).

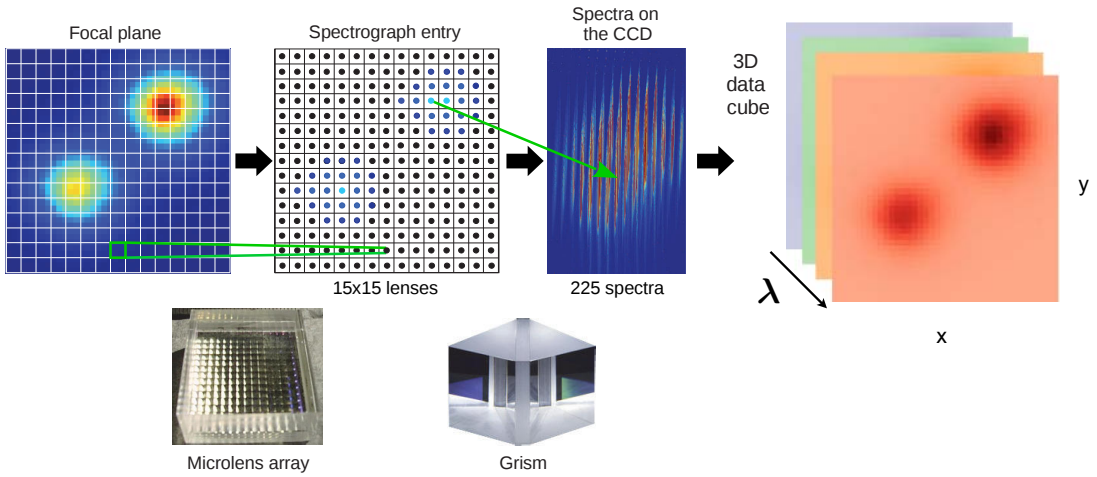

Fig. 5.2 SNIFS concept: the focal plane image is split in 225 parts by a micro lens array. The light from each of these lenses in then dispersed by a grating, leading to the reconstruction of a datacube where there is an image of the field observed for each wavelength. From Buton (2009).

The internal calibration unit of SNIFS has arc and continuum lamps to illuminate both the red and blue channel of the spectrograph. The arc provides discrete emission lines which are used to derive the wavelength calibration, typically used to calibrate a spectrograph. Calibration exposures with the arc lamp are needed for each science exposure that is acquired, as the position of the entrance pupil images slightly changes for each wavelength and at every telescope pointing. Even with the optical model, a small adjustment is required to correct for these movements. The comparison of the positions of the observed arc emission lines on the CCD with their known central wavelengths allows this correction.

The continuum lamp produces a spatially uniform continuum-like emission, and is used as spectro-spatial flat field to compensate for spaxel-to-spaxel variation of the spectrograph and spectral non-uniformity. In this case the flat field does not correct directly pixel-to-pixel effects, as described in sec. 4.2.2, but these variations will anyway be partially corrected, and consequently reduced, as a spaxel contains a group of pixels (and it is integrated over them). It is also used to remove fringing patterns, which become non-negligible from 8500 Å. The element splitting the light between blue and red channel is a dichroic, the transmission of which depends on humidity and temperature. These variations are largely confined to some small regions of the spectrum and a continuum exposure is acquired to correct them, for each science acquisition. Since only small regions of the spectra are needed, a small portion of the CCD is read out to save time (a raster image). Full continuum exposures, for spatial and spectral flat fielding, are acquired at the beginning, middle, and end of each night of observations since the SNIFS' transmissivity is assumed to be very stable.

In fig. 5.3 the different kinds of illumination are shown, from an arc, a continuum, and a star, with the images they would produce on the CCD. We can see how calibration images differ with respect to science observations.

5.2.1 Calibration pipeline

A usual SNIFS observation night is split into science observations (e.g. SNe or host galaxy references) and a set of standard stars which are observed throughout the entire night to trace the atmospheric extinction evolution and to provide the flux calibration. The SNIFS calibration pipeline performs the following steps:

1. Preprocessing: bias and dark subtraction.

2. Background subtraction: diffuse scattered light is subtracted by fitting a polynomial to regions of the CCD where no light is expected (between the spaxels).

3. From the arc exposure of the related science exposure, an optical model is computed and the obtained mask is used to extract the spectrum from the CCD (i.e., each CCD pixel is mapped to a wavelength in a spaxel). After this, the wavelength calibration is performed, producing a wavelength calibrated datacube.

4. A spectro-spatial flat fielding cube is computed from the composition of the several continuum exposures of the night and, after correcting the dichroic features with the raster exposure, it is applied to the wavelength-calibrated science cube to correct for spaxel-to-spaxel variations and spectral features, that belong to the instrument used rather than to the science spectrum observed.

5. The cosmic rays are then removed using sigma clipping. This method consists in computing a spatial median on the spaxels, after renormalization, and subtract the median from the input datacube and then flag the values which are ten times bigger than the standard deviation of the data.

6. For the flat-fielded datacube of the observed standard stars, a 3D (where x and y are along the spaxels and in the third dimension are the wavelengths) Point Spread Function (PSF) model is fitted to extract their spectra. In case of standard stars observations, the tails of the PSF are assumed to be the sky background component. While the light from an astrophysical source crosses the Earth atmosphere, it undergoes an effect called Atmospheric Differential Refraction (ADR, Filippenko, 1982), which displaces the observed light chromatically (the center of the object is shifted as function of wavelengths) and another effect called a *seeing*, for which the dimensions of the object increase for the bluer wavelengths (see sec. 5.3). SNIFS field of view is large enough to

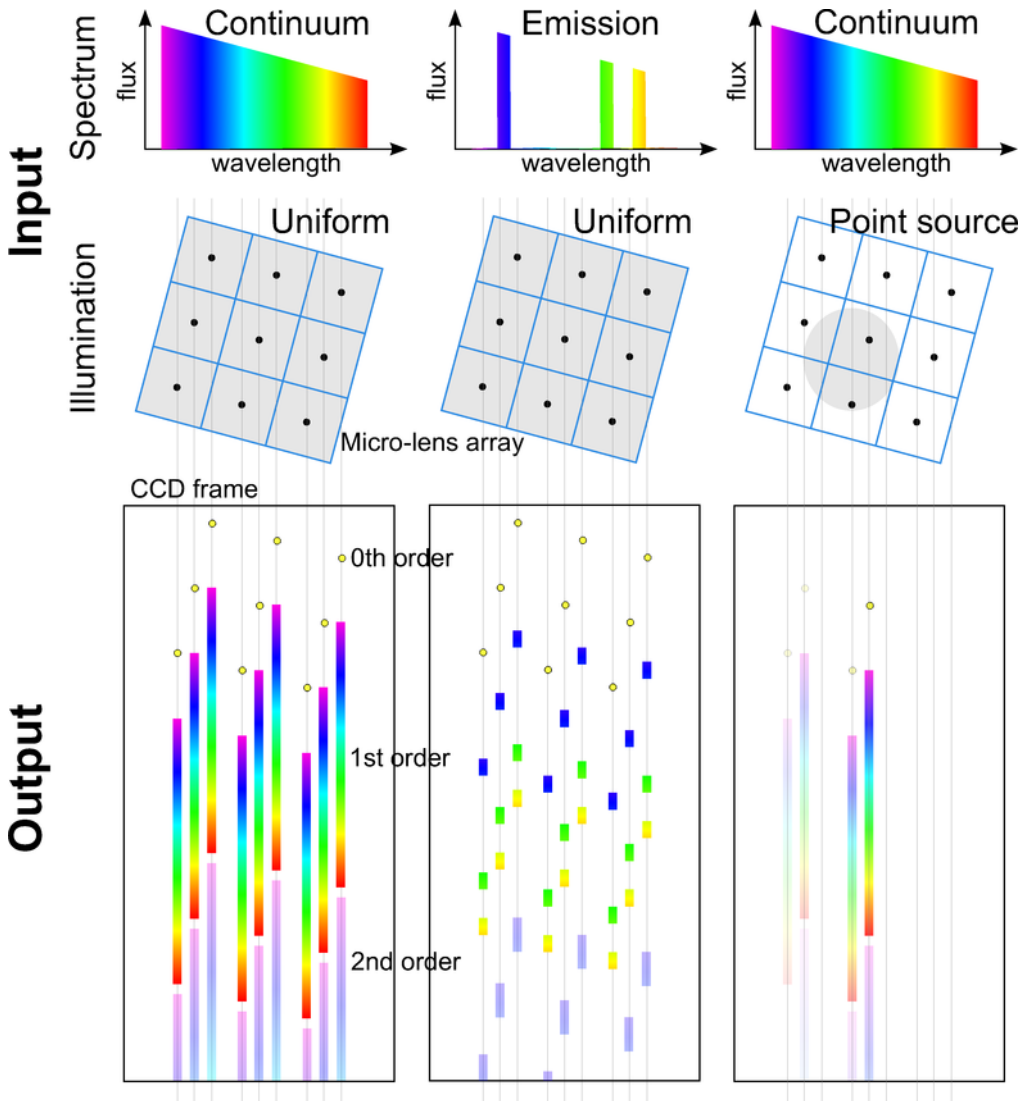

Fig. 5.3 Working principle for the IFS under several forms of illumination. Left: spatially and spectrally uniform illumination, for example with the continuum calibration lamp. Middle: spatially uniform illumination with emission lines, for example with the arc lamp for wavelength calibration. Right: continuum spectrum point like source, as for example from a standard star. From Copin (2013).

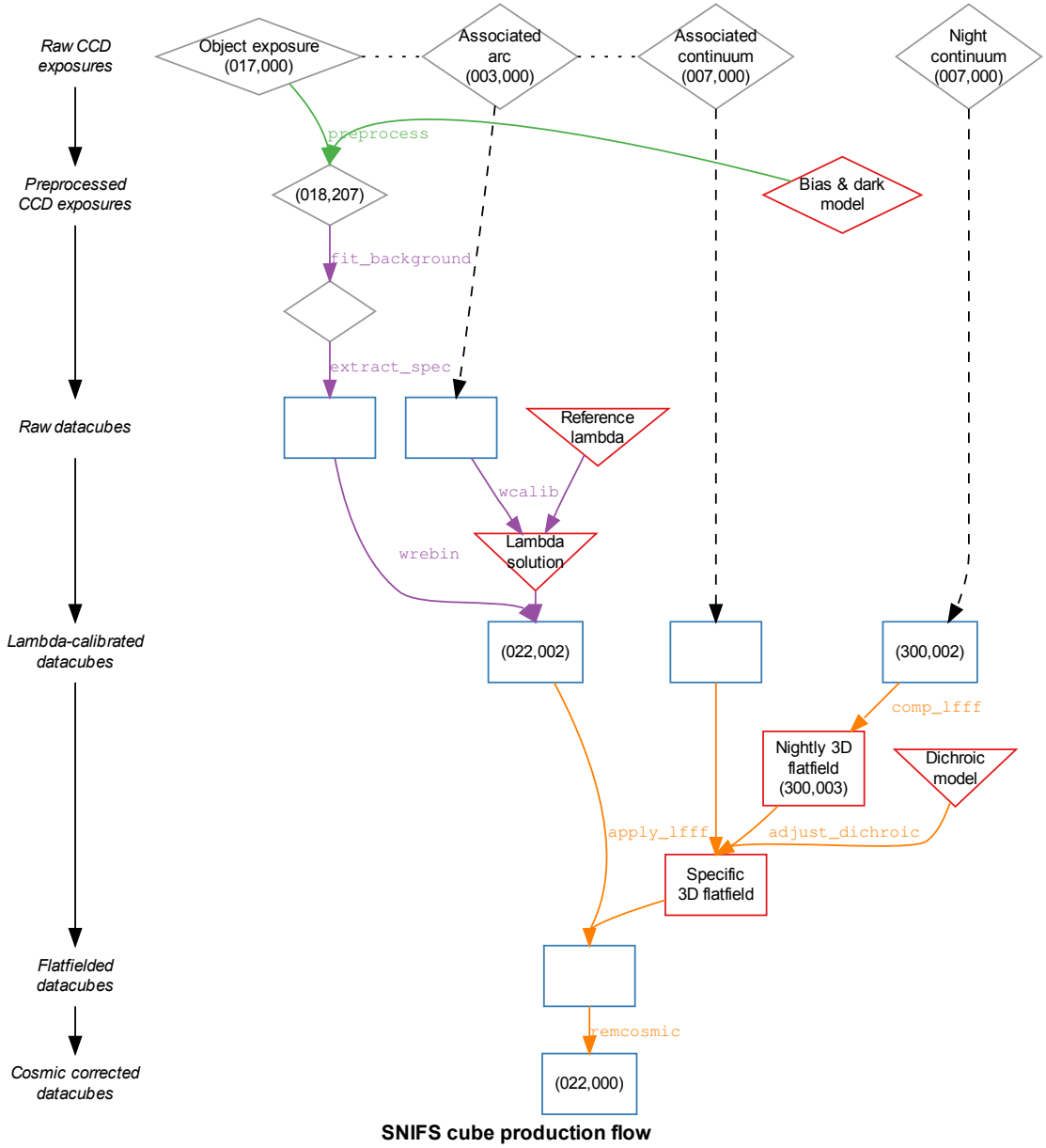

Fig. 5.4 Calibration scheme with pipeline steps from 1 to 5 (sec. 5.2.1). From Copin (2013).

observe the entire star at all wavelengths and its PSF model accounts for this changed size due to these effects, as the model is fitted for each wavelength. This step allows to extract the flux of the star and obtain a spectrum from a 3D datacube.

7. A nightly flux calibration is computed through comparing the extracted spectra of all the standard stars observed with their reference fluxes. It corrects for the instrumental response and the atmospheric extinction (see sec. 5.2.2).

8. Now flux calibrated datacubes can be obtained by applying the flux calibration on flat-fielded datacubes.

9. Finally the science object spectra are extracted (again fitting a PSF model as before) and they are now in flux units. In the case of SNe or host galaxy spectra the extraction procedure is more complex, as the sky and galaxy contributions have to be separated from the star one. This is outside the scope of this thesis.

In fig. 5.4 a schematic of the SNIFS calibration pipeline is shown, performing the steps from 1 to 5.

5.2.2 Atmospheric extinction

The SNfactory atmospheric extinction correction is described in detail in Buton et al. (2013) and summarized here.

The dominating contributors to the total extinction as function of wavelength are: Rayleigh and areosol scattering, ozone absorption and telluric lines. Rayleigh scatters is due to light scattered by molecules and atoms in the atmosphere, whose dimensions are smaller than the incident wavelength. Its value as function of wavelength depends only on the surface pressure for a given observing site, which in our case is always measured.

The areosol particles expected at Mauna Kea are mostly sea-salt particles with the same dimensions as the scattered wavelengths. Their amount is expected to be very small at the summit (assumed constant through the night) and their scattering amplitude follow a power law with the inverse of wavelength. The parameters of this trend are adjusted in the fit of the atmospheric model.

The ozone component of the atmosphere is responsible for absorption. Its behavior with wavelength is given by a template in fig. 3 of Buton et al. (2013). The scale factor of this template is a parameter of the fit, as well.

Buton et al. (2013) verified that the scattering due to water (clouds) is grey and hence only its time variability is evaluated. If there is no time variability, the night is considered photometric and non-photometric otherwise. In fig. 5.5, the median atmospheric extinction in units of airmass from SNIFS observations (using 7 years of observations) and its median

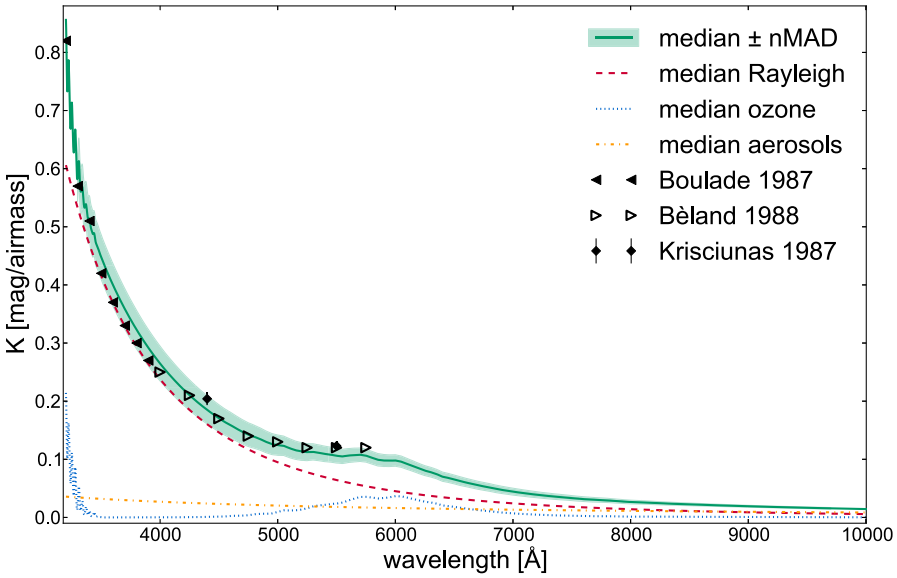

Fig. 5.5 Median atmospheric extinction on Mauna Kea (full line) and the single physical components (dotted lines). The model is compared with older observations (triangular and circular markers). From Buton et al. (2013).

contributions are shown. The airmass measures the optical path length of the light observed through the atmosphere along the line of sight (line between observer and star) and it depends on the distance from the object observed to the zenit. The minimum airmass value achievable with ground observations is 1. Usually observations are performed at airmasses between 1 and 2, corresponding to 90° and 30° altitude.

The telluric lines are due to the presence of O_2 and H_2O in the atmosphere. Their absorption affects only small wavelength regions and therefore it is not evaluated in the fit of the atmospheric extinction model, but on a separate step. A mean value of the absorption width of these lines is computed from all the SNfactory observations, for O_2 and H_2O separately. Then, once the nightly smooth atmospheric extinction and the reference spectrum is divided out from the observed standard star spectrum, only those lines are left in the residual spectrum. These lines are then integrated, and their values show a linear trend in function of airmass. This trend is fitted using the mean values (over all SNfactory data), computed before, as slope and the intercept from the fit provides the intensity of the lines for the night. Having the width and the intensity of the lines, they can be removed from the spectra observed.

The atmospheric extinction evaluation is, hence, based on the comparison between standard stars observations with their known SED values, as in:

$$X_{\rm obs}(\lambda,\hat{z}) = X_{\rm int}(\lambda) \times T_{\rm snifs}(\lambda) \times T_{\rm tel}(\lambda) \times T_{\rm atm}(\lambda,\hat{z}), \tag{5.1}$$

where $X_{\rm obs}(\lambda,\hat{z})$ is the standard star spectrum observed at airmass $\hat{z}$, $X_{\rm int}(\lambda)$ is its intrinsic value, $T_{snifs}(\lambda)$ is the throughput of SNIFS (including the QE of the CCD), $T_{\rm tel}(\lambda)$ is the throughput of the telescope and $T_{\rm atm}(\lambda,\hat{z})$ is the atmospheric transmission for that specific observation, composed of the parts mentioned above. The system throughput and atmospheric extinction are evaluated at the same time and cannot be measured independently with the current pipeline – any variability not captured by the components above is incorporated into the instrumental response.

When the atmospheric conditions are considered stable across the night (photometric) the throughput of the system – $T_{\rm snifs}(\lambda) \times T_{\rm tel}(\lambda)$ – can be estimated by the pipeline. In this case the instrumental response (from the flux solution in the case of airmass $\hat{z} = 0$) is divided by the flat fielding datacube (steps 4 and 7 of sec. 5.2.1) and a datacube with the throughput of the system is then derived. The pipeline, then, stores a median instrumental response of the "SNIFS+telescope" system, which we call S_λ. We will use this to compare it with our calibration results as will be described in sec. 9.2.3. In SNfactory collaboration, S_λ is only used to measure large scale evolution of the system over timescales of years and never directly applied to the data.

5.3 Integral Field spectrophotometry and SNfactory

Splitting the field of view in many spaxels allows to have a spectrum for each one of them. With respect to the more common slit spectrographs, where only the light from a slit is dispersed, this approach can provide a cleaner way to remove the sky and galaxy contribution from the SN spectrum. In fact SNIFS' field of view is centered on the SN and includes part of the host galaxy and the sky, simplifying the difficult task of disentangling the contributions of each of them. In the slit spectrograph case, on the other hand, the spectrum of the galaxy can only be removed using templates, and the light collected from the SN depends on the precision with which the slit is centered on the object. All the cases in which the SN is located near the center of the galaxy are even harder to treat since the galaxy component is brighter. However, slit spectrographs are generally used to observe galaxies and study their properties (hence they do not need to remove SNe spectra). For ground based observations one has to consider also the ADR (described before) and the seeing. Due to the ADR (which is a static and predictable effect), the position of the object with respect to the slit will vary with wavelength and airmass. The seeing, on the other hand, is due to changes in the refractive

index of the atmosphere caused by turbulence in its layers. It is therefore different from night to night, and also within the same night. The overall effect is that the position of the image of the object will slightly move while acquiring the image, hence, blurring the final image. The total dimension of this effect depends on the amount of turbulence. This phenomenon makes the observed size of the object grow with airmass, and with the inverse of wavelength. One would have to fix these issues in order to avoid light losses from some wavelengths when observing an object with a fixed slit dimension. In the case of SNIFS, the 3D PSF model fit to the data (step 6 in sec.5.2.1) allows more flexibility as it extracts the flux of the star specifically for each wavelength and SNIFS field of view is sufficiently big to fit the entire PSF for each wavelength.

SNfactory collected several hundreds SN Ia spectra over the last 10 years. Large field surveys, such as Palomar Transient Factory (PTF) or LaSilla-Quest (LSQ), observe the sky every night and as soon as they find a new transient, comparing images of patches of sky with older ones, they send alerts to several other telescopes. After receiving such an alert, SNIFS observes the object and, if the transient is a spectroscopically confirmed SN Ia, a follow up campaign starts. The SN is observed at regular time intervals, thereby building a spectropotometric time series of its evolution in time. One example of this is the series from the explosion of SN 2011fe shown in fig. 5.6. From top to bottom the spectral evolution of the SN light is shown from 15 days before to 97 days after peak brightness. Light curves can be produced by integrating the spectra in different bandpass filters. From the time series in fig. 5.6 we obtain the light curves shown in fig. 5.7 in the U, B, V, R, I SNfatory filters. These filters are simple top-hat functions with sensitive wavelength range between: $3300 - 4102$ Å, $4102 - 5100$ Å, $5200 - 6289$ Å, $6289 - 7607$ Å and $7607 - 9200$ Å respectively. One can also obtain the light curves by integrating the spectra with any other filter curves. This allows to compare results with other programs.

The great advantage of using SNIFS is the possibility to perform spectral analysis simultaneously with the usual photometry. The additional information provided by the spectra can be used to improve the standardization of SNe by studying their spectral features. Since the progenitors and the explosion mechanism are not entirely understood yet, the spectral behavior of SNe can be very different for each of them, also depending on the phase and redshift (Fakhouri et al., 2015). Monitoring their evolution in detail has proven to be a very strong tool for assessing possible biases in future surveys targeting high redshift objects.

Furthermore, as SNIFS observations are always accompanied by spectra, K-correction errors (see sec. 3.2.3) are by definition zero, removing a major source of error for most surveys (Saunders et al., 2015). All these qualities, that an IFS has compared to a regular imager, are the reasons why a similar design has been proposed for future satellite mission for high-z sample, such as WFIRST[2].

[2]https://wfirst.gsfc.nasa.gov/index.html

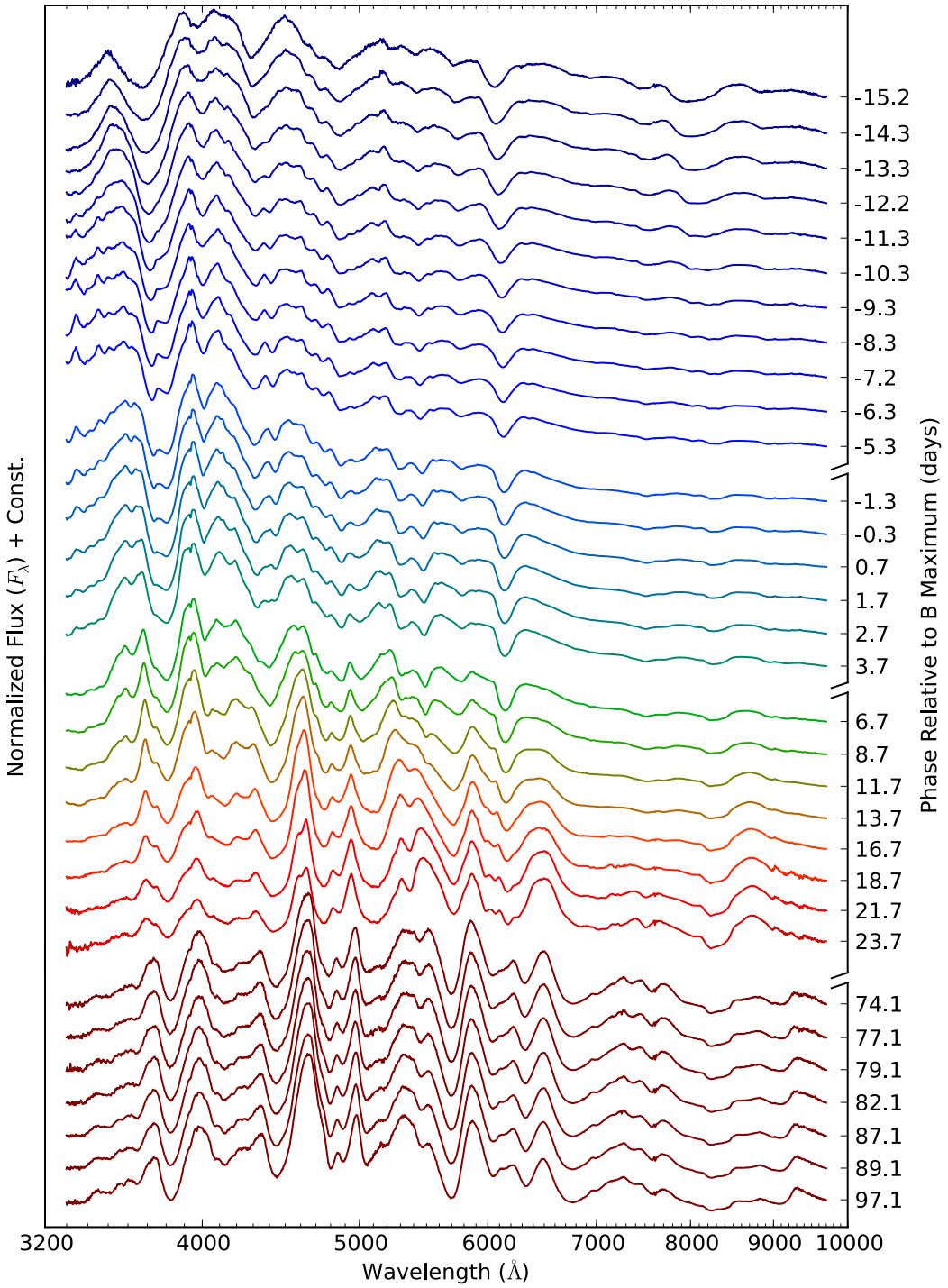

Fig. 5.6 SN2011fe time series observed with SNIFS. From top to bottom is the spectral evolution in time. From Pereira et al. (2013).

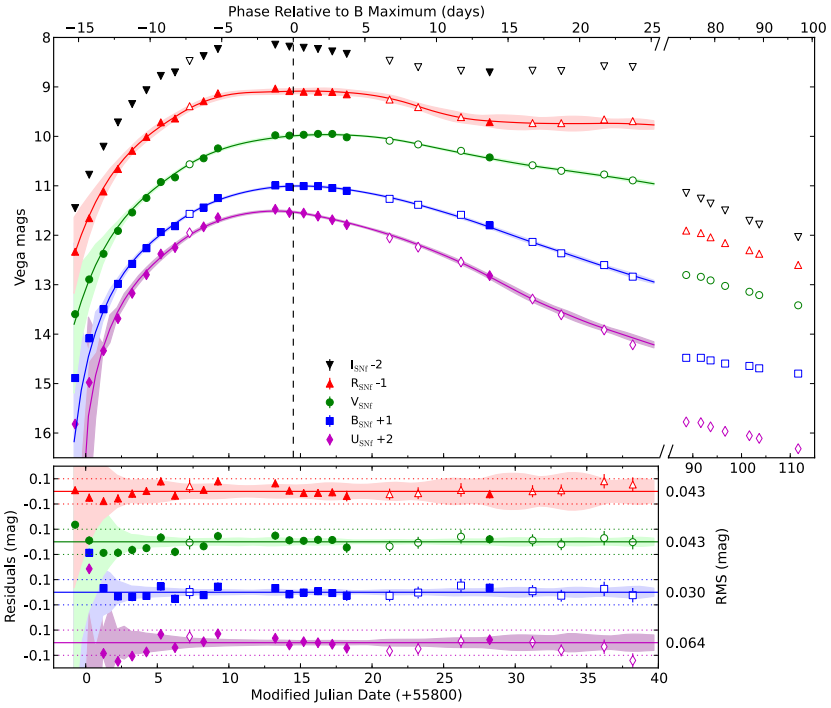

Fig. 5.7 Light curves in different filters obtained by integrating SN2011fe time series observed with SNIFS. From Pereira et al. (2013).

Chapter 6

SNIFS CALibration Apparatus

As mentioned, this thesis focuses on the development and test of a flux calibration device to lower the systematic uncertainties on calibration, that limit SN Ia cosmology (sec. 3.2.3). In this chapter a general overview of the SNIFS CALibration Apparatus (SCALA, Lombardo et al., 2014) design and components is given. SCALA's goal is to provide a precision (to within 1%) calibration of the "SNIFS+UH 88" system to then recalibrate the standard star network. As previously mentioned at the end of sec. 4.3.3, by calibrating a spectrograph such as SNIFS, the calibrated standard star spectra can be ideally used by every other observer and not just by SNfactory.

The final design of SCALA came about through a long series of developments from the one proposed initially. Before building the components (described in sec. 6.2), an intense optical simulation phase helped optimize and prove the design (sec. 6.3.1 and 6.3.2). After the construction of the individual parts, they were tested in the laboratory environment to characterize their response as function of wavelength before the assembly in the final configuration. In sec. 6.4 there is a description of these tests and their results.

Tests performed on the final configuration using the calibrated reference photodiodes (which are SCALA's flux standards), to establish a reliable data taking technique in combination with SNIFS, can be found in the next chapter.

6.1 Requirements: from SNIFS to SCALA

From the description of SNIFS in the previous chapter, we can deduce a series of requirements that the calibration unit has to fulfill, to reach our goal. These are also based on the characteristics that an ideal flux calibration instrument should have as seen in sec. 4.3.3:

1. Capability to uniformly illuminate a field of view larger than $9' \times 9'$. The device can, in this way, be used also to calibrate the imaging channel and its filters (number 1 of the list in sec. 4.3.3).

2. The device must be able to scan the 3300–10000 Å range, to ensure coverage of SNIFS range of usage (3300–9700 Å).

3. Its light has to be continuously monitored to check for intensity variations or irregularities (number 4 of the list in sec. 4.3.3).

4. The device has to illuminate the entire telescope entrance pupil, or at least a good fraction of it, to sample possible achromatic large scale gradients across it. It also has to have an illumination close to the science object one (number 2 of the list in sec. 4.3.3).

5. It should be fixed to the telescope dome at an elevation that is within the range of normal science operations in order to have the ability to account for the gravitational load on the telescope optics + baffling that could, in principle, affect flux calibration.

6. It has to be fully remotely controllable. These last two qualities permit its usage at any time.

All these requirements, combined with the limited space available in the dome and safety concerns, have brought us to SCALA final design as presented in the next section.

6.2 SCALA Design

SCALA consists of 18 $f/4$ (i.e. focal length of 80 cm) parabolic mirrors with diameters of 20 cm each, distributed over the entrance pupil in a nearly hexagonal arrangement (see Fig. 6.1, top panel). Integrating spheres fed by a wavelength-tunable light source (from UV to IR) illuminate the mirrors producing 18 collimated beams with small divergence of 1° – the beams are not perfectly parallel. This is the characteristic that allows us to fulfill the number 1 and 2 requirements in the list in sec. 4.3.3, which would normally exclude each other.

To monitor the stability of the light source, as well as the flux produced by the device, we installed two Cooled Large Area Photodiodes (CLAPs) in front of two of the 18 $f/4$ mirrors, in such a way that they can measure part of the reflected light. These photodiodes are the flux standards meant to transfer NIST calibration to the light source (SCALA light-beams), according to the scheme shown in fig. 4.5. Finally, because the light-beam of SCALA does not illuminate the entire UH 88 mirror, a mask was created that can be mounted at the top of the telescope. With the mask mounted, the standard stars observed illuminate the same

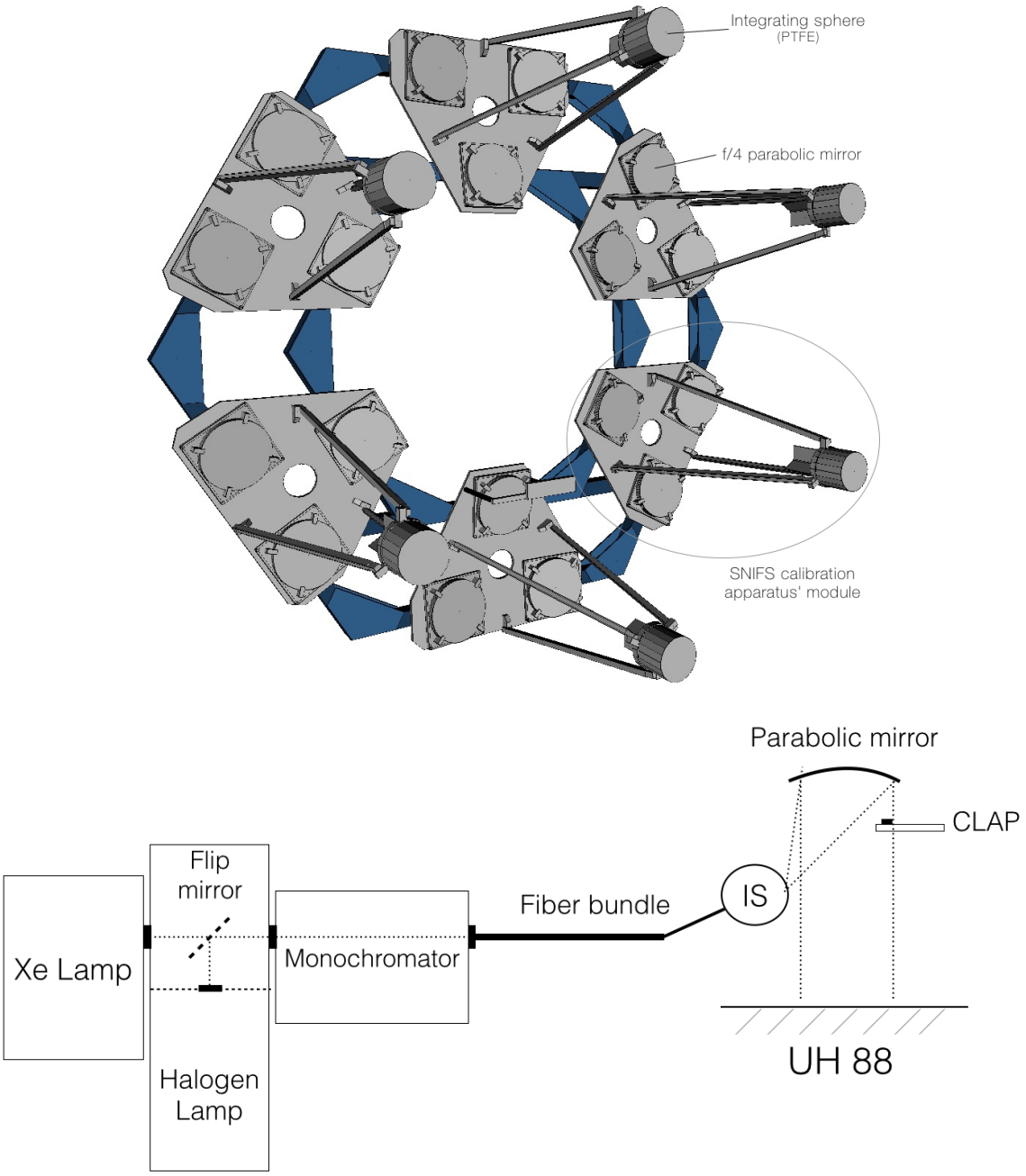

Fig. 6.1 Top: hexagonal arrangement of the six submodules of SCALA. This structure is mounted in front of the entrance pupil of the telescope. Bottom: SCALA scheme showing the lamp system and the flip mirror which allows to select the lamp output illuminating the monochromator entrance, the fiber bundle that feeds the IS, and the calibrated photodiode (CLAP), which faces the parallel beam reflected by the mirror. The dotted lines represent the light path. The flipping mirror is placed in the same housing as the Halogen lamp to avoid light leaks. From Lombardo et al., 2017 (in prep.).

region of the primary mirror calibrated with SCALA. A conceptual scheme summarizing the device is shown in the bottom of fig. 6.1 (for the simplified case with only one mirror). In the next subsections we provide a more detailed description of each component of SCALA: the lamp system, the modular composition and the light monitoring system.

6.2.1 Light sources

Input light for SCALA is generated by either an APEX-Illuminator with a 150 W Xe lamp, for calibration of the wavelength range 3300-7020 Å, or a halogen lamp used between 7020 and 10000 Å. As shown in fig. 6.2 the Xe lamp shows strong and narrow emission lines above 7020 Å that would be difficult to calibrate. The dual-lamp solution enables to create an emission-line free light source and avoid these issues.

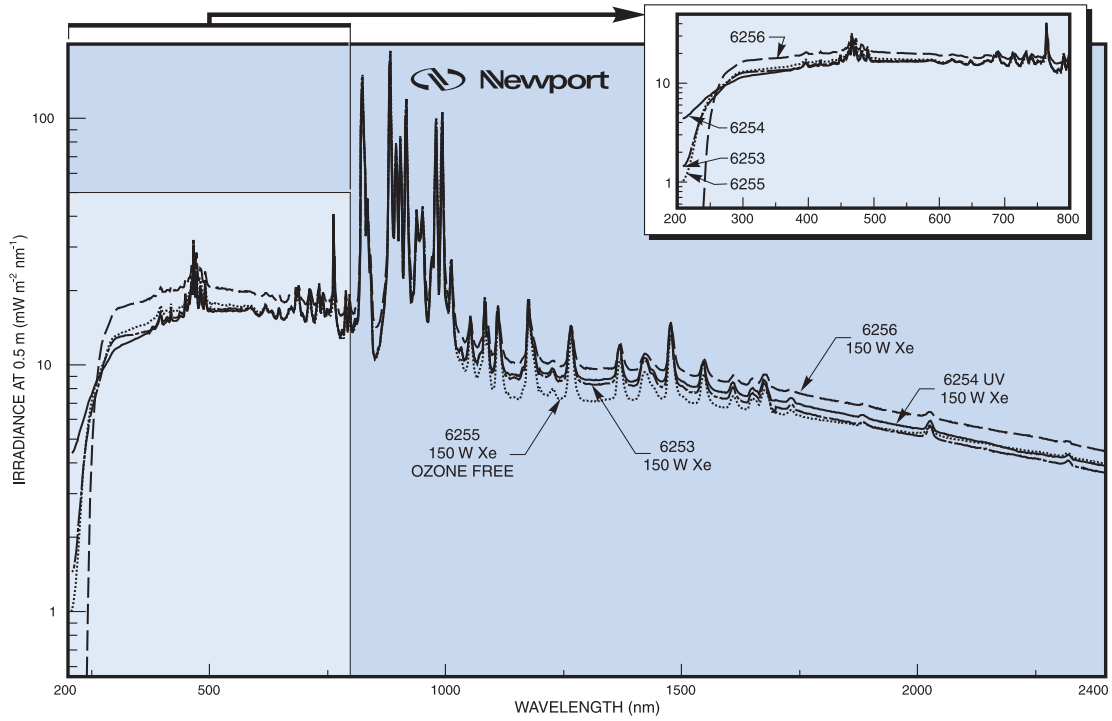

Fig. 6.2 Xe lamp spectra for three different lamp models from the Newport catalog: https://www.newport.com/medias/sys_master/images/images/hfb/hdf/8797196451870/Light-Sources.pdf. The one selected for SCALA is the Ozone free lamp (dotted line). The high and narrow emission lines above 700 nm prevent its usage in the redder wavelength range.

The combined SCALA spectrum with the Xe+halogen lamp will be shown in the next chapter (sec.7.3). The spectral resolution of SCALA is about 35 Å, in order to have a good balance between spectral resolution and light level. It is set by the dimension of the entrance

and exit slit of the monochromator (Cornerstone 260, Newport) used in the configuration with two gratings, of 1200 l/mm and blaze wavelength of 3500 Å and 7500 Å respectively. The two gratings are selected separately depending on the wavelengths range to calibrate.

The lamp system is also equipped with order sorting filters, to prevent the light, that will be dispersed as second order, from entering the monochromator. Even with these filters, one with cut-on at 3090 Å, and the other with cut-on at 4950 Å, we still observe second order light starting from 9000 Å. We can see from SNIFS exposures that its effect is subdominant until 9700 Å, but we conservatively limit our calibration range up to 9000 Å. Future works could, in principle, model this contribution and extend the calibration range to higher wavelengths.

In Table 6.1 the different configurations of lamps, gratings and filters, used in the wavelength range ($\Delta\lambda$) during regular calibration, are shown. For gratings and filters the value reported are the blaze and cut-on wavelengths respectively.

λ Range [Å]	Lamp	Grating [Å]	Filter [Å]
3200-4500	Xe lamp	3500	none
4500-5220	Xe lamp	3500	3090
5220-6240	Xe lamp	7500	3090
6240-7020	Xe lamp	7500	4950
7020-10000	halogen lamp	7500	4950

Table 6.1 Configurations of lamps, gratings and filters, used in the wavelength λ range during SCALA operations. Table from Lombardo et al., 2017 (in prep).

6.2.2 Fiber bundle and integrating spheres

A Ceramoptec (Optran WF[1]) fiber bundle brings the light from the monochromator to the six integrating spheres (ISs), splitting into six different arms, as shown in the technical drawing in fig. 6.3. The fibers inside these arms are composed in such a way that every arm has 33 fibers distributed across the exit slit of the monochromator to guarantee a homogeneous sampling of the entire slit (fig. 6.4).

The beam produced by SCALA and imaged in the focal plane of the telescope is an image of the light emitted by the integrating spheres. An integrating sphere is a spherical cavity coated with white and diffuse reflecting material, usually made of barium sulfate or PTFE (teflon) for use in the visible spectrum. Due to its characteristics the light entering from an input port is scattered inside the sphere many times before reaching the exit port, which is hence uniformly illuminated.

[1] http://www.ceramoptec.de/products/fibers/optran-uv-wf.html

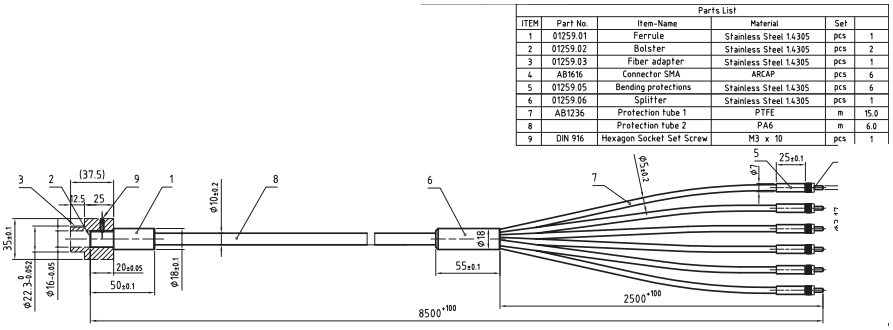

Fig. 6.3 SCALA's fiber bundle technical drawing: we can see the fiber input on the left and the six outputs on the right. The dimension on the drawing are in mm and the table on the top right corner specifies its construction details (private communication with Ceramoptec).

Fig. 6.4 SCALA's fiber bundle input, designed to match the monochromator output slit. Fibers represented with the same color belong to the same fiber arm. From Küsters 2014.

SCALA's ISs (fig. 6.5) have been designed and produced to achieve a flat field with variations $< 1\%$. They have three 1.4 cm exit ports, each illuminating one mirror. They consist of an outer housing of black anodized aluminum with a cylindrical shape. Within this housing we placed the massive PTFE cylinder, constructed by cutting the cylinder in half, machining hemispheres (8 cm inner diameter) on the abutting faces, roughening the hemispheres' surfaces to improve the diffusion properties, and reconnecting the cylinder.

6.2.3 Projector module

SCALA is composed of six projector modules, as the one shown in Figure 6.6, arranged in a hexagonal pattern (see fig. 6.1).

As already mentioned, the fiber bundle feeds the light from the monochromator to the ISs, which illuminate the $f/4$ parabolic mirrors. The mirrors are in an off axis configuration, which allows to reflect the light into collimated beams – with 1 degree divergence due to the dimension of the ISs exit ports – without being obstructed by the IS itself. The flux of the reflected beam varies across the mirror due to the asymmetric illumination introduced by the off-axis configuration. This flux gradient is canceled by the other two beams of the same projector module placed symmetrically with respect to the first one. The other projector

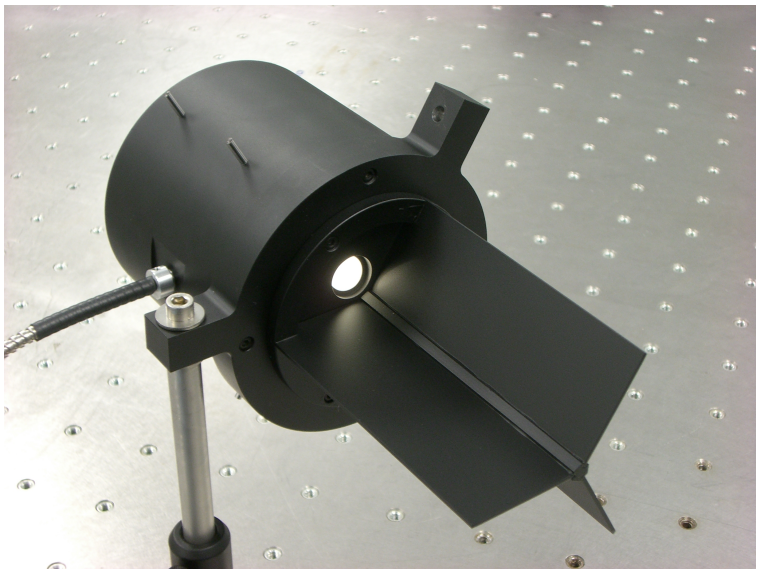

Fig. 6.5 One of SCALA's integrating spheres. The cylindrical aluminum housing and the white PTFE inside can be seen through one of the exit ports. The rectangular aluminum plates extending from the cylinder are the light baffles discussed in sec. 6.3.1. On the side it is also visible the entrance port for the fiber bundle.

modules are placed symmetrically (with an hexagonal arrangement) in front of the entrance pupil of the telescope, providing further cancellation of potential residual gradients.

Most components of SCALA are constructed from aluminum (for a total weight of 150 kg), and the hexagonal aluminum profiles that hold the projector modules are attached to a steal ladder in the dome of the telescope. This construction is sufficiently robust that SCALA can, in principle, preserve its position in an environment exposed to wind loads and earthquakes.

6.2.4 Reference system

The reference system continuously monitors the light produced. For this task we use two CLAPs (Cooled Large Area Photodiode), which were, in turn, directly calibrated to photodiodes calibrated by NIST (National Institute of Standards and technology). The CLAPs (Hamamatsu S3477-04) have a sensitive area of 5.8×5.8 mm and are equipped with a Peltier cooler (that is an electrified junction made of two different semiconductors in which the current flowing cools one surface and heats up the other where a heat sink dissipates the heat) that keeps them at a temperature of $-14°$C in the UH 88 dome.

During operations, one photodiode is used to monitor the light emitted by SCALA. The second photodiode is used for calibration and system monitoring. More details about them

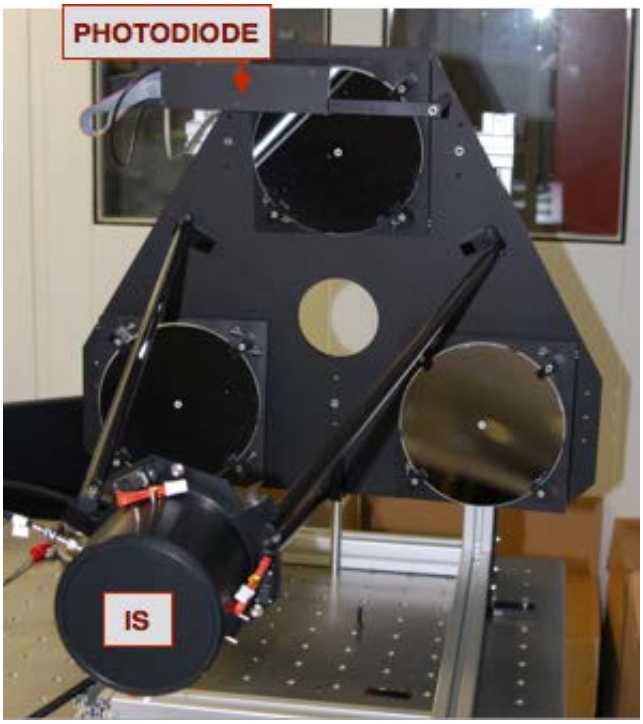

Fig. 6.6 One of SCALA's projector module. The triangular shape of the mounting with the three mirrors facing the integrating sphere is visible. The calibrated photodiode (CLAP) is mounted in front of one of the mirrors. From Lombardo et al. (2014).

are given in the next chapter where we exclusively focus on their description and on how their data look like.

6.2.5 Mask

The 18-mirror design of SCALA only illuminates 17% of the primary mirror, which could produce calibration offsets if the mirror reflectivity varies with wavelength and position. To eliminate such errors, we designed a mask to cover the non-illuminated 83% (plus a little more – up to 90% – for safety). This mask is used both when calibrating the "telescope + SNIFS" system's response and when observing the standard stars to calibrate them. This way, the effective optical path of the celestial targets will be calibrated. Once the stars are calibrated, the mask can be removed for standard observations.

The mask is mounted at the top of the UH 88 telescope tube. It is made of ALUCORE painted with a matt black finish and has holes of 16 cm of diameter aligned to match the SCALA beams, as shown in fig. 6.7. Being undersized allows a position tolerance of ± 2 cm transverse to the beams. The mask is further described in Küsters et al. (2016).

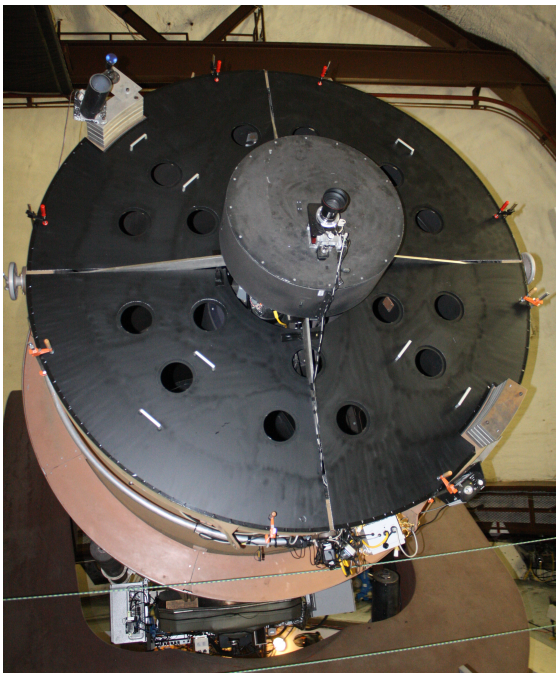

Fig. 6.7 Entrance pupil mask used when observing standard stars in combination with SCALA.

6.3 Simulating the design

Before constructing SCALA, the design has been extensively simulated with the photon engineering software FRED[2]. Refinement and optimization of many design details (an example is discussed in sec. 6.3.1) and a theoretical proof of concept (sec. 6.3.2) were made before construction. Only a selection of the simulations performed are shown in this section.

6.3.1 Refining the design: baffles for integrating spheres

The original plan for SCALA was to build a set of 4 projector modules to be placed in a horizontal, or vertical configuration. Such projecting row (or column) was meant to be moved in front of the entrance pupil of the telescope to ensure full illumination, as schematically illustrated in fig. 6.8.

Hexagonal masks for each of the mirrors were planned to avoid over- or under-exposing the primary, due to overlapping regions of the beams while scanning the primary mirror of the telescope. The illumination generated by the projector modules summed along one direction – y axis if we consider a row of projector modules – is illustrated in fig. 6.9 in the case without hexagonal masks applied. This would produce a non uniform pattern (on the

[2]http://photonengr.com/software/

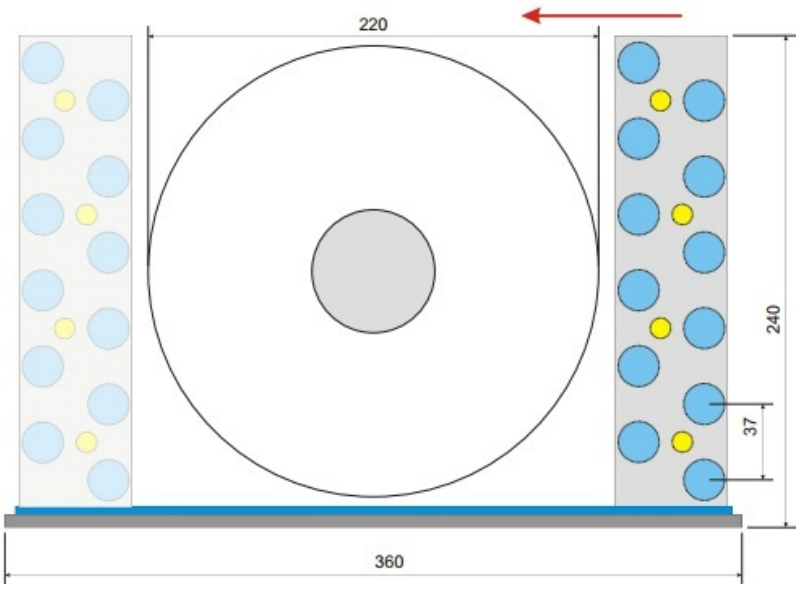

Fig. 6.8 Original design for SCALA with a column of 4 projector modules placed one next to each other on a moving stage. The middle grey circle represents the obscuration due to the secondary mirror, the light blue circles are the SCALA mirrors and the yellow ones the integrating spheres. The dimensions shown are in cm.

entrance pupil) due to the overlapping regions illuminated by the SCALA beams. The usage of masks allows a more homogeneous and *flattened* illumination of the primary mirror of the telescope. Among the simulations performed to refine the design, also the shape and dimensions of the masks were simulated to obtain a more uniform illumination of the primary mirror.

Simulations were crucial to introduce elements for baffling and reducing the stray light produced. The integrating spheres illuminate a much wider area than the mirror, and it is possible that some of the light from an output port also hits the other two mirrors of the same projector module or of other modules, this way increasing the amount of stray light directed to the telescope. We limit this unwanted feature by mounting some light baffle around the exit port of the IS, as shown in the IS picture in fig. 6.5. This construction was used for the final SCALA design.

Simulations of the entire SCALA system, including the hexagonal masks applied on the mirrors (as in fig. 6.10), provide an excellent tool for analyzing the system performances. The results of the simulations of the set-up shown in fig. 6.10 are presented in fig. 6.11 where the module row is centered with respect to the primary mirror of the UH 88 (the central obscuration due to the secondary is shown as well). The effect due to IS baffles can be seen through comparing the left panel (illumination without baffle) with the right (with baffle) of fig. 6.11. The figures show the pattern created on a plane surface, placed in the immediate

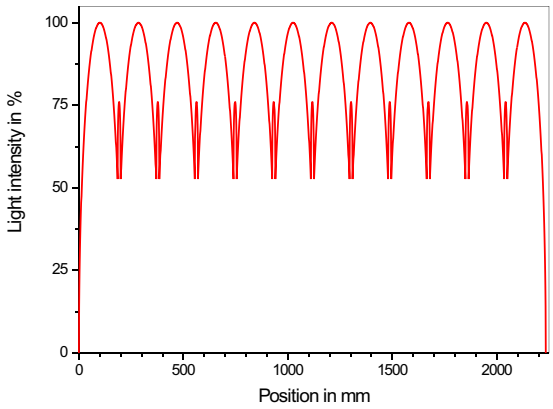

Fig. 6.9 Projected sum along the x axis of the UH 88 primary mirror of the 12 mirrors illumination from SCALA without hexagonal masks.

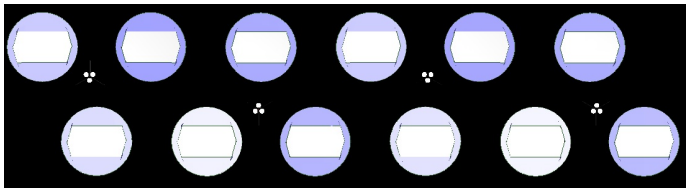

Fig. 6.10 SCALA –original– full set-up reproduced in the simulations. The 12 mirrors with hexagonal masks are visible. The small white circle in the middle of every projector module are the simulated integrating spheres holes.

vicinity of the primary mirror, by the propagation of the rays reflected from the SCALA mirrors. Every SCALA beam has a different color and in the case without baffles (left figure) the light from the ISs holes clearly illuminates more than just one mirror. Introducing the light baffle (right plot of fig. 6.11) greatly reduce the unwanted reflections and scattered light, ensuring that only the collimated beams from SCALA hit the primary mirror.

These simulations are only strictly true for the ideal case where the structures holding SCALA, its components and the dome environment (where it is mounted) are absorbing light at a 100% level, without any scattering. Unfortunately all surfaces and coatings have different reflection properties, and very rarely they are close to zero. Therefore there will still be some light scattered as function of wavelengths as discussed in sec. 10.2. In the simulations the idealistic approach of perfectly absorbing surface was kept for simplicity, and therefore the holding structures of SCALA and the mounting of the UH 88 optics were not simulated.

We eventually decided not to use the moving design outlined above, as we could not guarantee the stability of the system (which has to be tilted to be observable by the telescope). We thus opted for a safer, static and more compact design. We were able to cover a more extended part of the entrance pupil by increasing the number of projector modules to six,

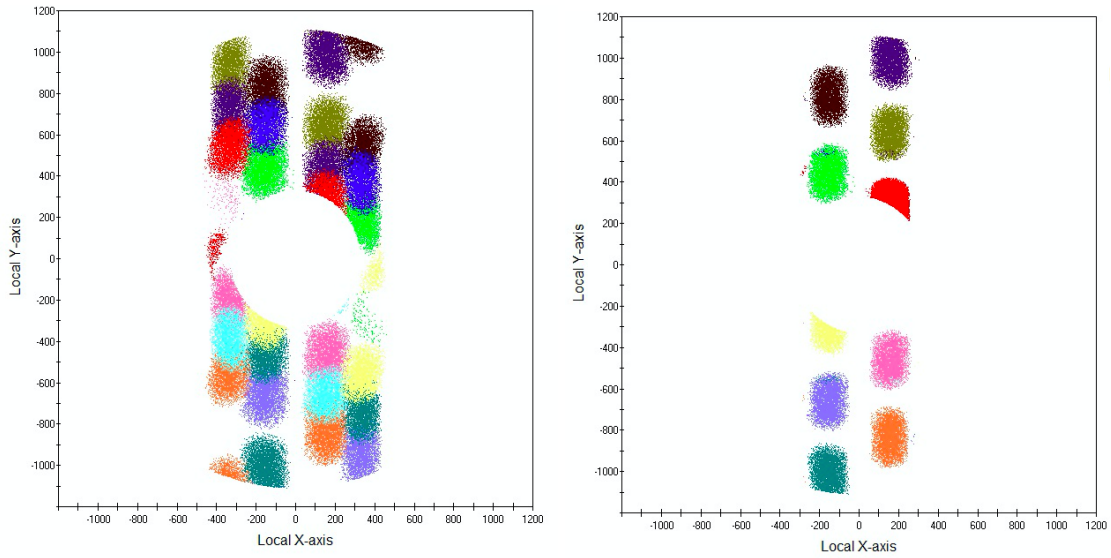

Fig. 6.11 Pattern created on a plane surface in the vicinity of the primary mirror of the UH 88 from simulations of the set-up in 6.10, in the case without (left panel) and with (right panel) integrating sphere light baffles. Every SCALA beam has a different color and the x and y axis are in mm.

without compromising the light level per beam. As mentioned before, the combination of this design with a mask on the primary mirror still allows to calibrate the same regions of entrance pupil, as that illuminated by stars.

A simulation of the illumination of the primary mirror of the telescope generated by the final design of SCALA is shown in fig. 6.12. This time we have the 6 projector modules configuration as in fig. 6.1, and since it is a static design we do not need the hexagonal masks on the mirrors and the beams are, therefore, circular.

6.3.2 Flatness of the beam

We can also use the simulations to check whether the selected design delivers the desired results. Since our goal is to create an extremely uniform and flat illumination of the focal plane of the telescope, the entire SCALA and UH 88 system was simulated and the light distribution in the focal plane checked, as schematized in fig. 6.13. The resulting overlap of the 18 beams from SCALA is shown in fig. 6.14 ,where the entire illumination of the focal plane is shown on the left hand-side plot and on the right hand-side there is a cut through its center along the x-axis. From these figures we see that the beam produced is flat to within 1% (<0.6% on the right plot) over its entire extension of 1°. We must keep in mind, though, that SNIFS' field of view is of 6.4" × 6.4", which corresponds to a square with a 0.6 mm side in the focal plane. The expected variations on the spectrograph field of view are, therefore, even

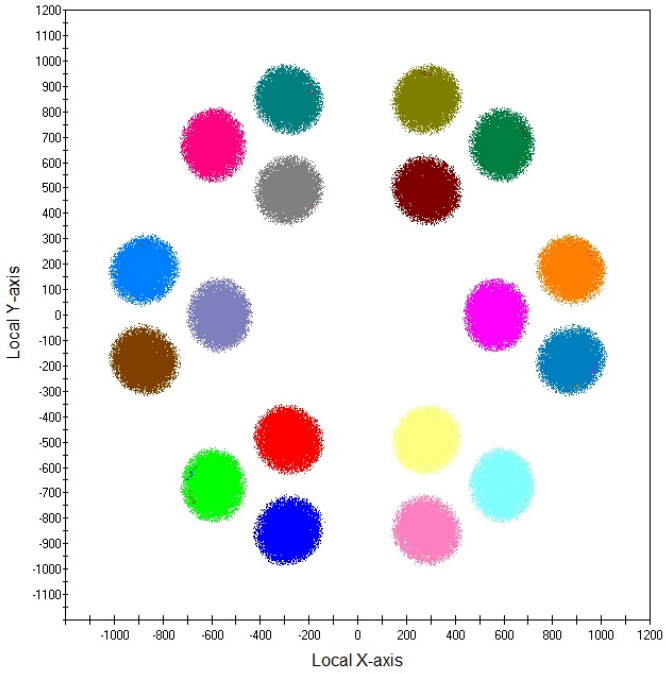

Fig. 6.12 Pattern of the SCALA illumination created on a plane surface in the vicinity of the primary mirror of the UH 88 from simulations of the set-up in 6.1. Every SCALA beam has a different color and the x and y axis are in mm.

smaller than 0.6%. However, with the computation resources at our disposal, we are not able to increase the resolution of the simulation and sample the focal plane with an appropriately finer grid.

6.4 Testing the performances

A very precise knowledge and control of SCALA is fundamental to reach our precision goal. After building the component, all of them were therefore tested to characterize their response as function of wavelength. Different set-ups (fig. 6.15) were created to measure fiber bundle arms, mirrors and integrating spheres transmissivity using a Xe lamp and monochromator (same models as finally used in SCALA) and a chopper in combination with two lock-in amplifiers, to amplify the signal received by the reference and signal photodiodes (two UV-035 EQC, thus not CLAPs). Each measurement was made 10 times and their averages and standard deviations, over the 10 acquisitions, were then stored. In the following subsections these measurements and their results are described in more detail.

These measurements did not use a halogen lamp. As the final goal is to compare the lab measurements with the in-situ ones to prove that we can reconstruct the overall color

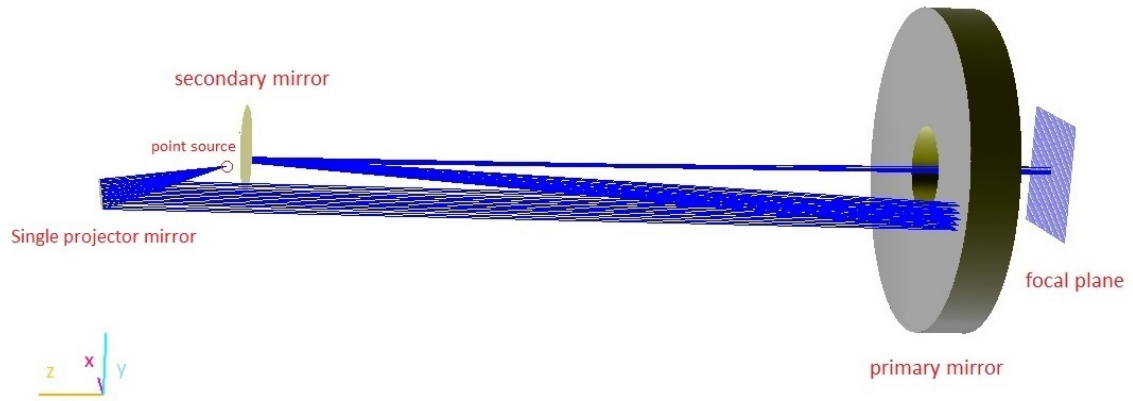

Fig. 6.13 Set-up for the simulation of the SCALA + UH 88 system, in the simplified case of a point source and only one SCALA mirror. In the figure are visible the primary and the secondary mirror of the UH 88 telescope with its focal plane.

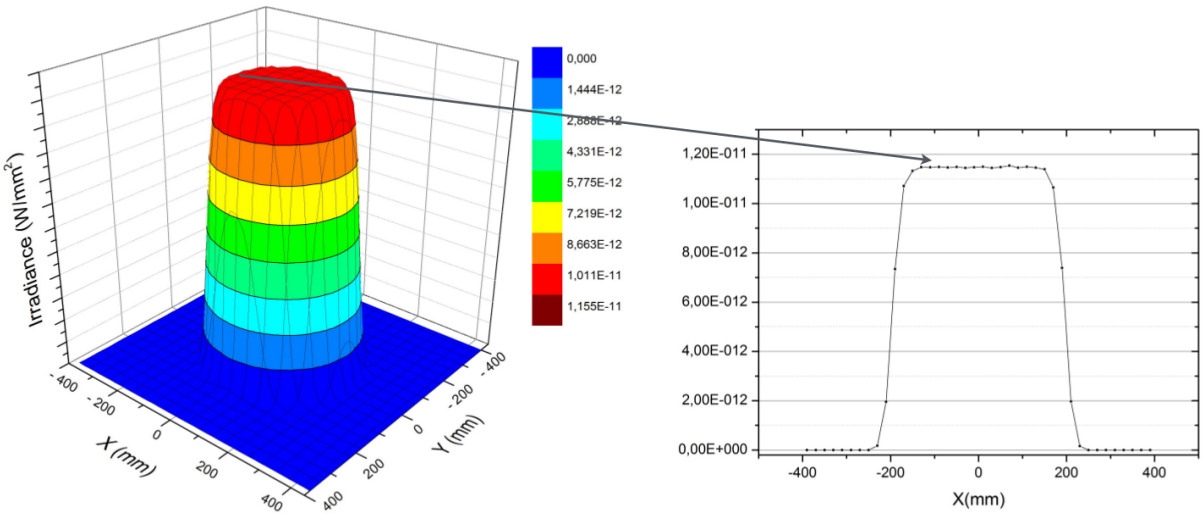

Fig. 6.14 Left: illumination of the focal plane of the UH 88 telescope simulating the final SCALA design. Right: cut through the middle of the beam along the x-axis direction. Note: SNIFS field of view corresponds to a square of 0.6 mm side.

trend, figures shown here stop at 7000 Å (where the halogen lamp is selected in the in-situ measurements). The pre- and post-commissioning setups, are systematically different and non comparable above 7000 Å. Furthermore, the narrow and bright emission lines (fig. 6.2) of the Xe lamp above 7000 Å cause too much variability in the comparison between different sets of laboratory measurements. This is due to the SCALA fibers distribution that samples the exit slit of the monochromator (see fig. 6.4): a small shift (0.5 Å) of the peak wavelength of the SCALA bandpass is found between the six fiber bundle arms (as shown in Küsters 2014). This effect is present, at a reduced level, between 4500-5000 Å, where some weaker emission lines are present. However, as the line amplitudes are smaller and the lines wider, the lamp can still be used in this wavelength range.

Before moving on to the description of SCALA components characterization, we summarize the working principle of photodiodes, the detector used for this set of measurements (and already mentioned several times in the thesis).

Photodiode A photodiode uses the same working principle of a CCD (discussed in sec. 4.1): the inner photoelectric effect. It is a p-n junction which generates a photocurrent once an electron-hole pair is formed and the build in electric field at the depletion region moves them towards the anode (holes) and cathode (electrons). The current generated is readout with a chosen frequency and integrated over a very small and fixed time (close to the maximum readout frequency usable). Thus, a photodiode can not integrate light as a CCD, by selecting the exposure time. As in the CCD case, we use photodiodes made from Silicon, as we wish to be sensitive to visible wavelengths.

An important quantity, that characterizes a photodiode, is its spectral responsivity: the ratio of the generated current to the incident light power as function of wavelength. This quantity is usually expressed in A/W but can be also given as a Quantum Efficiency (unitless).

The dark current, described in sec. 4.2.1, is another quantity to consider in a photodiode. As in the CCD case, we can measure a current also when the photodiode is not exposed to light. It is therefore fundamental to account for this effect when performing a precise measurement. Since photodiodes do not have a shutter to obscure their sensitive area, dark current measurements, usually, include the background/ambient light as well.

6.4.1 Fibers

For these tests, SCALA's fiber bundle was mounted at the exit of the monochromator. One fixed end was monitored with a reference photodiode (UV-035 EQC), and another photodiode, of the same kind, measured the light from one of the remaining 5 fiber bundles (as schematized in the top of fig. 6.15). The combined use of the chopper and lock-in amplifiers allows to correct the two photodiodes measurements for their darck current + background light and to

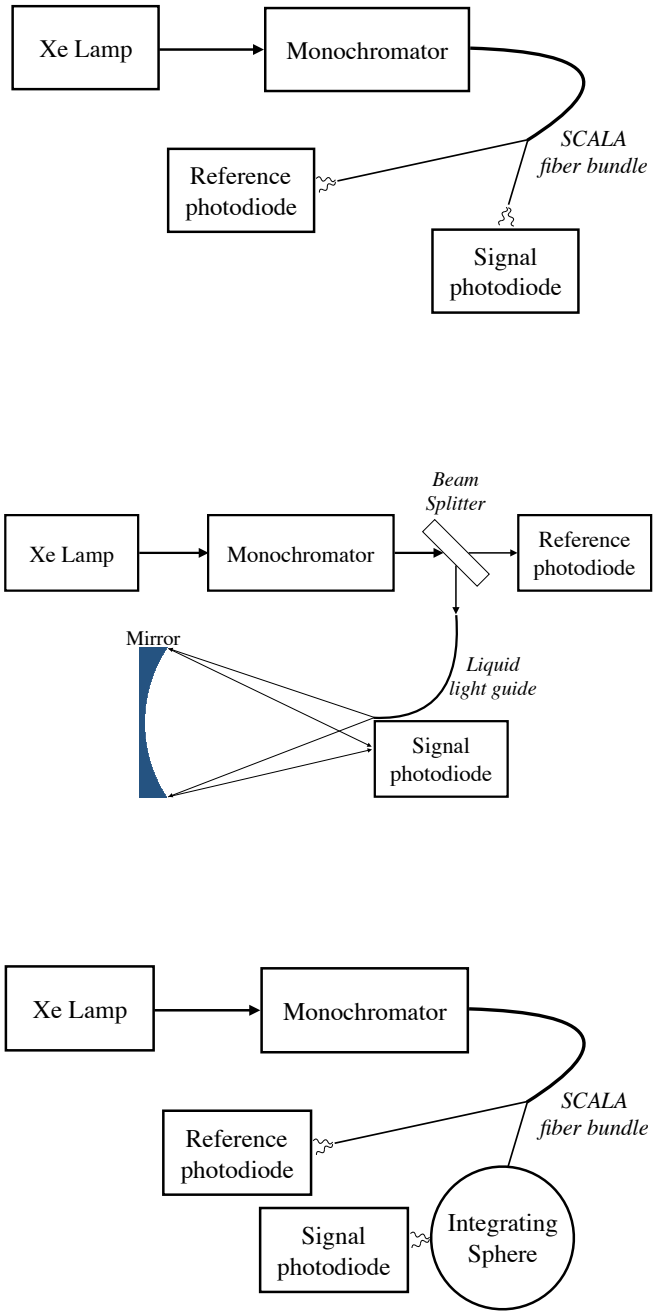

Fig. 6.15 Schematic representation of the set-ups for the laboratory tests of the SCALA components: fiber bundle (top), mirrors (middle), integrating spheres (bottom).

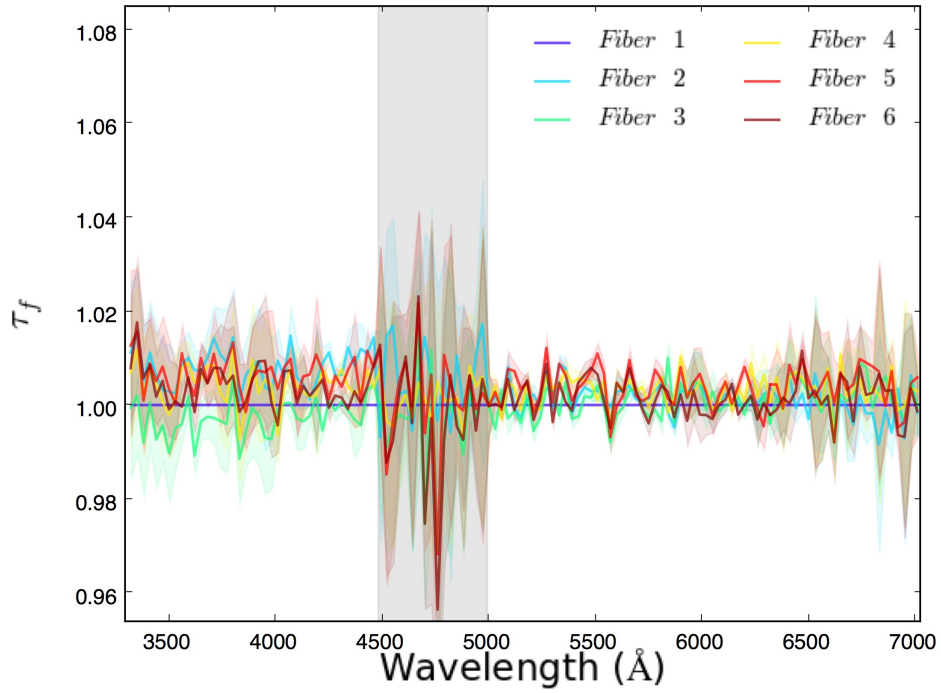

Fig. 6.16 Relative response of SCALA fiber bundles with respect to one of them, normalized at 5000 Å. The gray band delimits the region where the weak emission lines of the Xe lamp are located (4500-5000 Å) and the colored bands around the curves are the standard deviations of the measurements.

amplify the signal (this is used for the ISs and mirrors characterization as well). The spatial gap between the photodiodes and the fiber bundle ends was kept very small to observe the full light cone emitted. The response of every fiber bundle has been scanned in steps of 30 Å and plotted with respect to the reference bundle, as in fig. 6.16, according to:

$$\tau_{f_{i,1}}(\lambda) = \frac{S^i_{\rm ig}(\lambda)}{R_{\rm ef}(\lambda)} \cdot \frac{R^1_{\rm ef}(\lambda)}{S^1_{\rm ig}(\lambda)}, \tag{6.1}$$

where $S^i_{\rm ig}$ is the measurement of the signal photodiode for the i-th fiber bundle arm and $R_{\rm ef}$ is the one from the reference photodiode, $i = 1$ is for the reference bundle. The fibers show very similar wavelength sensitivity, with relative color trends smaller than 1%.

6.4.2 Mirrors

The responsivities of the 18 mirrors were measured similarly to the fibers, again using the lamp and monochromator system, but this time a beam splitter splits the light between a

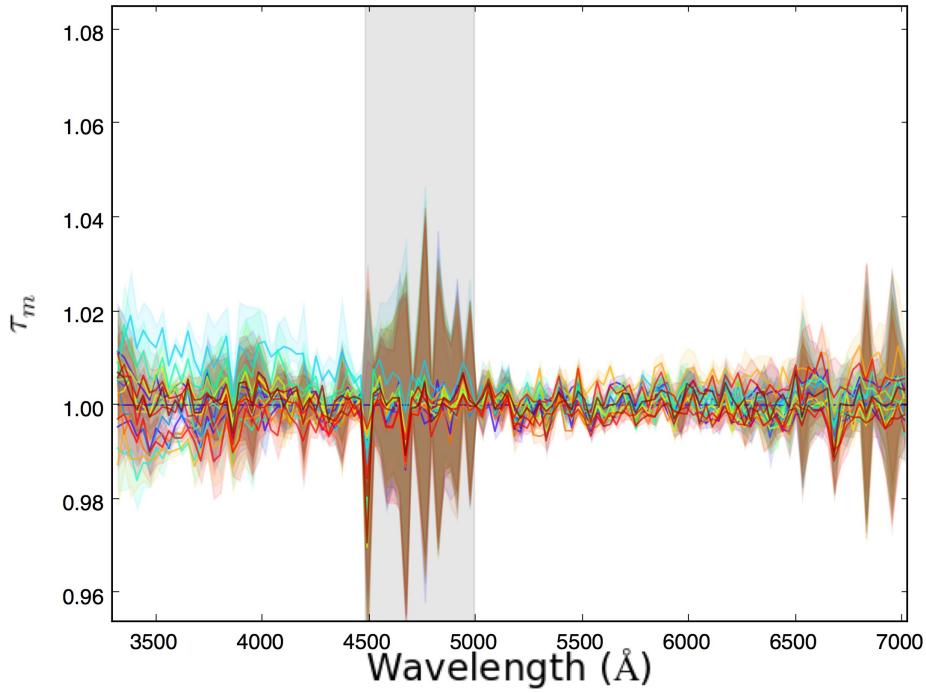

Fig. 6.17 Relative response of SCALA mirrors with respect to one of them, normalized at 5000 Å. The gray band delimits the region where the weak emission lines of the Xe lamp are located (4500-5000 Å) and the colored bands around the curves are the standard deviations of the measurements.

reference photodiode (always the same) and the entrance of a liquid light guide. The exit of the latter was illuminating a SCALA mirror, which then focused the light on the other photodiode (as represented in the middle of fig. 6.15). Fig. 6.17 shows the responses of the 18 mirrors with respect to one of them according to:

$$\tau_{\mathrm{m}_{k,1}}(\lambda) = \frac{S^k_{\mathrm{ig}}(\lambda)}{R_{\mathrm{ef}}(\lambda)} \cdot \frac{R^1_{\mathrm{ef}}(\lambda)}{S^1_{\mathrm{ig}}(\lambda)}, \tag{6.2}$$

where S^k_{ig} and R_{ef} have the same meaning as before for the k-th mirror, and $k = 1$ is for the reference mirror. Again, the color trend in these reflectivity comparisons is mostly gray, except below 4000 Å where it reaches 1%.

6.4.3 Integrating spheres

Finally, the integrating sphere responses were measured using the same set-up as for the fiber bundles, by connecting one fiber bundle arm with the IS entrance port and positioning

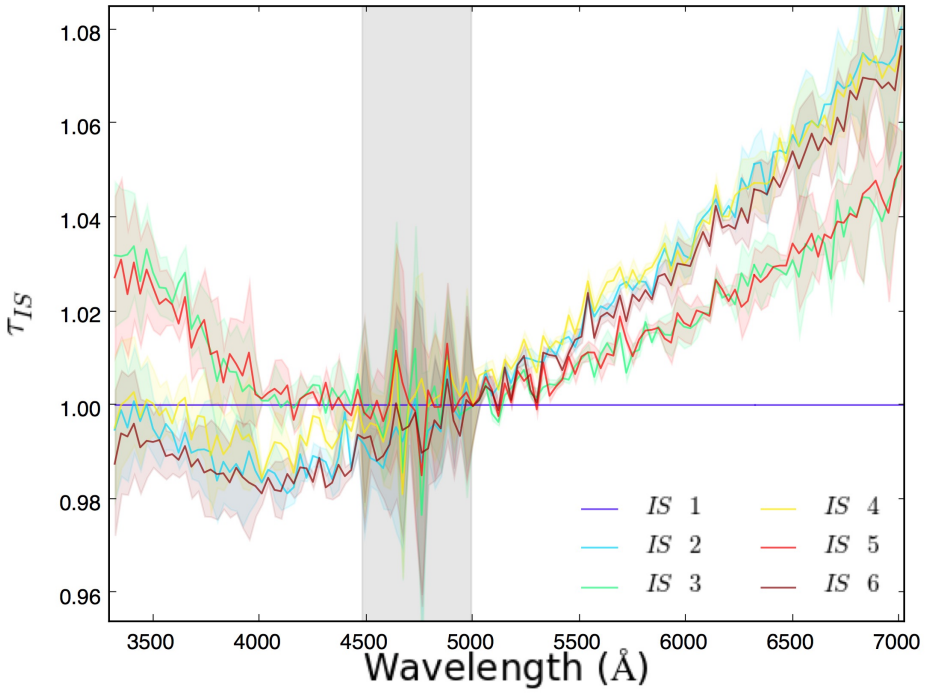

Fig. 6.18 Relative response of SCALA ISs with respect to one of them, normalized at 5000 Å. The gray band delimits the region where the weak emission lines of the Xe lamp are located (4500-5000 Å) and the colored bands around the curves are the standard deviations of the measurements.

the second photodiode immediately in front of one of the exit port (as in the bottom plot of fig. 6.15). The set up was built in such a way that the relative distances between the elements was not changing when measuring the other ISs. Once again fig. 6.18 shows the response function of the 6 ISs used for SCALA with respect to one of them:

$$\tau_{\mathrm{IS}_{j,1}}(\lambda) = \frac{S^{j}_{\mathrm{ig}}(\lambda)}{R_{\mathrm{ef}}(\lambda)} \cdot \frac{R_{\mathrm{ef}}(\lambda)}{S^{1}_{\mathrm{ig}}(\lambda)}. \tag{6.3}$$

Here, color trends reach the 6-8% level, likely due to the slightly different characteristics of the PTFE blocks from which they were machined. A small variation in the reflectivity of the material would correspond to a larger variation in the efficiency of the IS[3].

[3]For more information, look at eq. 12 of https://www.labsphere.com/site/assets/files/2551/a-guide-to-integrating-sphere-theory-and-applications.pdf

6.4.4 Putting it all together

In the previous subsections we have seen that the relative responses of the SCALA components have different behaviors as function of wavelengths (significantly so for the ISs). Since we are interested in the overall light produced by SCALA, we combine the above single components to match the final arrangement as in fig. 6.1 as:

$$P_{i,j,k}(\lambda) = \tau_{\mathrm{f}_{i,1}}(\lambda) \cdot \tau_{\mathrm{IS}_{j,1}}(\lambda) \cdot \tau_{\mathrm{m}_{k,1}}(\lambda), \tag{6.4}$$

where $P_{i,j,k}(\lambda)$ is the relative response of the SCALA beams with i-th fiber bundle, j-th integrating sphere and k-th mirror with respect to the reference beam, which is the same beam where the reference CLAP is positioned in the in-situ setup. The τ functions in the equation are the ones plotted in figs. 6.16-6.18, but without normalization at 5000 Å.

In those figures we always plotted the ratio between the signal and the reference measurement, to correct for lamp light level variations. Additionally we compare this quantity to the signal/reference ratio of the reference component, $i = k = j = 1$ (as in eq. 6.1-6.3). Therefore, by using eq. 6.4, we obtain a quantity that does not depend on the two photodiodes QEs or on the wavelength trend of the component scanned by the reference photodiode for each measurements.

Mirrors and fiber bundles do not present variations larger than 1% with respect to the reference for the wavelength range scanned. The IS curves will thus have the biggest impact on the overall wavelength trend of the SCALA beams in eq. 6.4.

Even if the ISs show strong trends as function of wavelength, repeated measurements of the same IS were very reproducible (as shown in Appendix A.1). The measured ISs responses, thus, allow us to properly account for these differences.

Chapter 7

CLAP calibration and output data

As mentioned in sec. 6.2.4, we equipped SCALA with two Cooled Large Area Photodiodes (CLAPs, two Hamamatsu S3477-04) of which one of them is used as flux standard to monitor the light (CLAP1) and the other one (CLAP0) to perform systematic checks. The two CLAPs have been produced by the DICE team for us (Regnault et al., 2015) and similar ones have also been used by their calibration experiments, SnDICE and SkyDICE. The CLAPs are detailed in this chapter, including the calibration procedure adopted, by the DICE team, to build the sensitivity curves of both photodiodes (sec. 7.1). Laboratory measurements meant to characterize them are presented as well, in sec. 7.2. We conclude presenting an estimate of the exposure times for SCALA wavelength observations used during the commissioning campaign in 2014 and their final version (sec. 7.3).

7.1 Photodiode calibration

Each CLAP module is composed of a front-end and a back-end board. The front-end board (box of 50 mm x 180 mm x 15 mm) includes the photodiode and a low noise amplifier; in its back-end the signal digitization is performed (box of 120 mm x 120 mm x 35 mm). These devices are small and compact enough to be placed in front of our beams without obscuring the light from the integrating sphere. The CLAPs calibration precision reaches a level better than 0.6% over the wavelength range of interest. For our in-situ measurements we set their sampling frequency to 1kHz.

The CLAPs have been calibrated relatively to a NIST calibrated photodiode (the flux laboratory standard previously described in sec. 4.3.3), in 2013. In their spectro-photometric lab-bench, the DICE team used stable LEDs (described in Regnault et al., 2015)) as light source input to a monochromator. The output of the monochromator was, then, focused on the CLAP photodiode, firstly, and the NIST one secondly. They compared the light level measured by the two of them and subtracted by the dark current. By using several LEDs with

central emission wavelengths ranging from 3500 Å to 9500 Å they sampled the responsivity of the CLAPs across wavelengths. One of the LED spectra as measured by the CLAP1 and NIST photodiodes is shown in fig. 7.1. It is hard to, by eye, separate the two curves as they mostly overlap. For the two CLAPs calibration, the DICE team used only the data of the LEDs spectra observed, whose values, normalized at peak, are between 0.5 and 1, to keep a high signal to noise ratio.

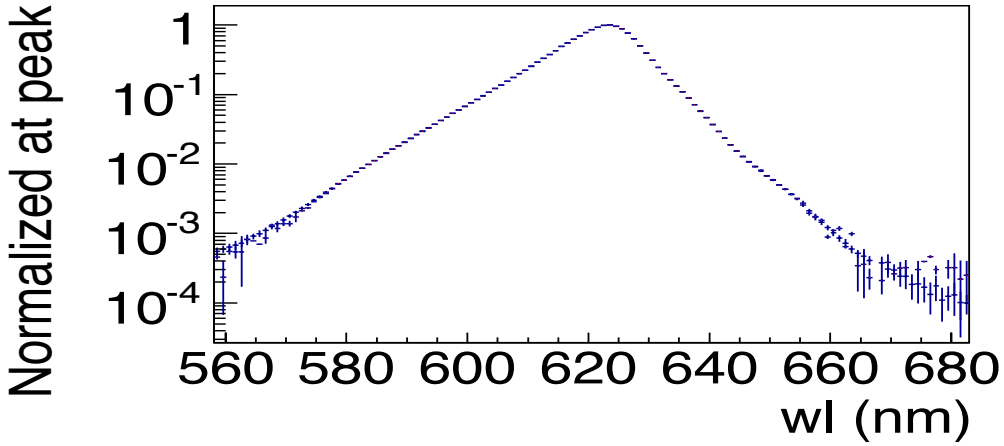

Fig. 7.1 Spectrum of the LED 14 ($\lambda_{\text{peak}} \simeq 625\,\text{nm}$) as observed by NIST and CLAP1 photodiode plotted superimposed and normalized at peak. (From the CLAP calibration report by Kyan Schahmaneche and the DICE team).

The ratio between the NIST and CLAP1 measurements is shown in fig. 7.2 with different color for each of the LEDs used. A five degree polynomial is fit to the ratios, to properly consider the different quantum efficiencies in the gaps between the datapoints and at the extreme wavelengths (UV and IR), where no LED was used. This yields a complete calibration curve over the entire range of wavelengths where the CLAP1 is sensitive. This fit and its residual are visible in fig. 7.2. Even if the rms (root mean square) of the residuals is $< 0.1\%$, for the response curve a conservative value of 0.15% has been chosen as additive error to the NIST calibration error. The calibration for CLAP0 is performed in the same way as for CLAP1 yielding almost identical results and precision. The response curves for both CLAPs are shown in fig. 7.3 where the CLAP0 response has been multiplied by 10 to make them comparable (since it has a 10 times smaller internal gain).

The two photodiodes have five readout channels that can be used one at the time. The first readout the signal registered by the photodiode without any additional gain, and the second with a gain of 41.05 ± 0.002 for CLAP0 and 43.5 ± 0.002 for CLAP1. The other three channels readout the measurements of temperature of the photodiode, of the photodiode's head and of the backend electronic box.

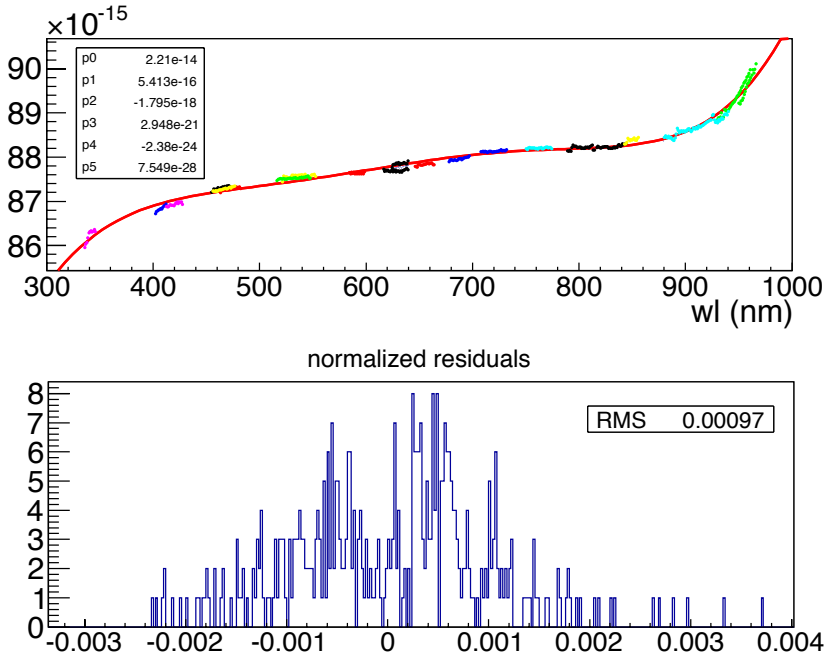

Fig. 7.2 Top: intercalibration between NIST-CLAP1 photodiodes: each short colored line correspond to the relative calibration derived from one LED, the red line is the 5 degree polynomial fit to the data. Bottom: residuals of the fit. (From the CLAP calibration report by Kyan Schahmaneche and the DICE team).

7.2 Background measurements of the photodiode

Every time a photodiode measures the light level, this quantity includes also the ambient light, from the surrounding environment, and its own dark current (as mentioned in sec. 6.4). These have to be carefully removed to have a proper measurement of the light emitted by SCALA.

Since the CLAPs do not have a shutter, we overcome this issue by performing three measurements for each wavelength observation: before and after the light exposure we expose the photodiodes for about 2 s with the monochromator's shutter closed to measure the background level (which is temperature and time dependent), and between these we perform the light exposure with the monochromator's shutter opened. The photodiodes continuously measure during these three phases.

The element ultimately setting the exposure time for the SCALA wavelength observation is, therefore, the shutter of the monochromator. CLAP data are thus not only used as light monitor, but also as independent mean to retrieve the exposure time information (further discussed in sec. 10.2.5). Furthermore, with the selected sampling frequency (1kHz) for the

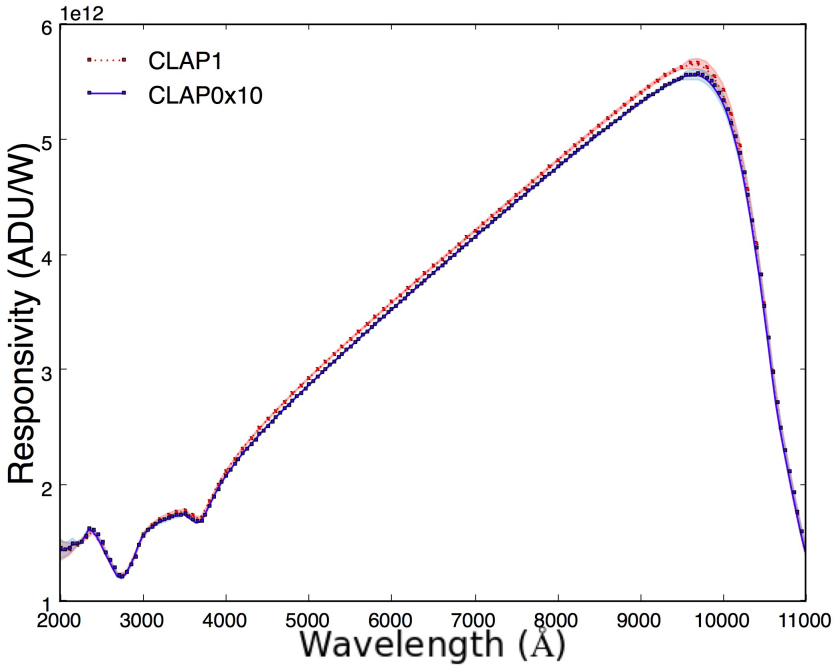

Fig. 7.3 Response curve in ADU/W of the two photodiode, CLAP1 (the reference) in red and CLAP0 in blue multiplied by 10 (as this has a lower internal gain).

in-situ measurements, we are able to measure the rising and falling ramp due to the opening and closure of the monochromator shutter.

In fig. 7.4 (left hand side plot) an example of a typical CLAP data-set with the entire SCALA wavelength range sampled in 60 Å steps is shown. The light level from SCALA is continuously recorded together with the two background exposures which precede and follow it. The following CLAP data reduction steps were applied to the data shown in the two plots. First of all (left hand side plot of fig. 7.4) the cosmic rays are removed from the data with a sigma clipping technique, by rejecting the data whose value is higher than the average ± 5 times the standard deviation. Secondly we compute the parameters that describe a line passing through the first and the second background, by a linear regression. This line is subsequently subtracted from all the data (background and light exposures) of a single wavelength observation (right hand side of fig. 7.4).

On the left hand side plot we notice the presence of ambient light slowly varying with time from the background exposures (the blue data). By applying the background removal procedure we are able to correct the light measurements (in red) for this effect as shown in the right hand side plot. The method described allows a background removal better than 0.3% for nighttime data, and 2.6% for daytime data, where these variations can occur on

smaller time scales, as shown in Küsters et al. (2016). More details about the background removal technique are discussed in the systematics section.

After removing the cosmic rays and the background level from the data, we have the option of directly averaging the signal. We obtain, therefore, a series of data, one for each wavelength observed, in units of ADU. The next steps of the data reduction and the other data reduction path – with SNIFS observations – are discussed in sec. 7.4 and sec. 9.2.2 respectively.

7.2.1 Laboratory tests of dark current evolution

The high precision reached for the nighttime background removal is mostly due to the very stable dark current of the calibrated photodiodes. Before commissioning, we verified this very important characteristic of the SCALA reference system as follows.

Because of the overall dimensions of SCALA, of about 2.2 m lateral size, we assembled it in an empty cellar of the Physics Institute (in Bonn) for testing, as shown in fig. 7.5. We performed most of the tests at this location. The entrance to the cellar was sealed with black foils, to make it as dark as possible.

Even with this precaution, small light leaks due to the presence of holes in the sealing, were still present and also the smallest one of them can cause visible variation in the light level registered by the CLAPs. Furthermore the presence of warm water pipes inside the room, caused varying temperature of the room, which can affect the dark current of the photodiodes. However, as mentioned in sec. 6.2.4, the CLAPs are mounted on a Peltier cooling system which keeps them at a temperature of about 0°C in the cellar environment (it is even lower in the UH 88 dome, ~ -14°C).

In the set-up shown in fig. 7.5 the background level of both CLAPs was measured for almost 48 hr consecutively. The result of such measurements is shown in fig. 7.6 where every point is an average over 1 s of background exposure with a sampling frequency of 250 kHz. Considering that the longest exposure performed with SNIFS to observe a SCALA line is about 5 min, we can conclude that in this time the dark current of the photodiodes varies negligibly and smoothly. The larger variations noticed in the data (fig. 7.6) might be due to the above mentioned light leaks during daytime measurements, represented by the shaded areas. We can conclude that the two background exposures for each SCALA line observed (as in fig. 7.4) are representative of the dark current level presents during the light exposure. By subtracting the background level as explained in sec. 7.2 we properly account for the dark current of the photodiode for nighttime measurements, when the dark current is the major contribution to the background level.

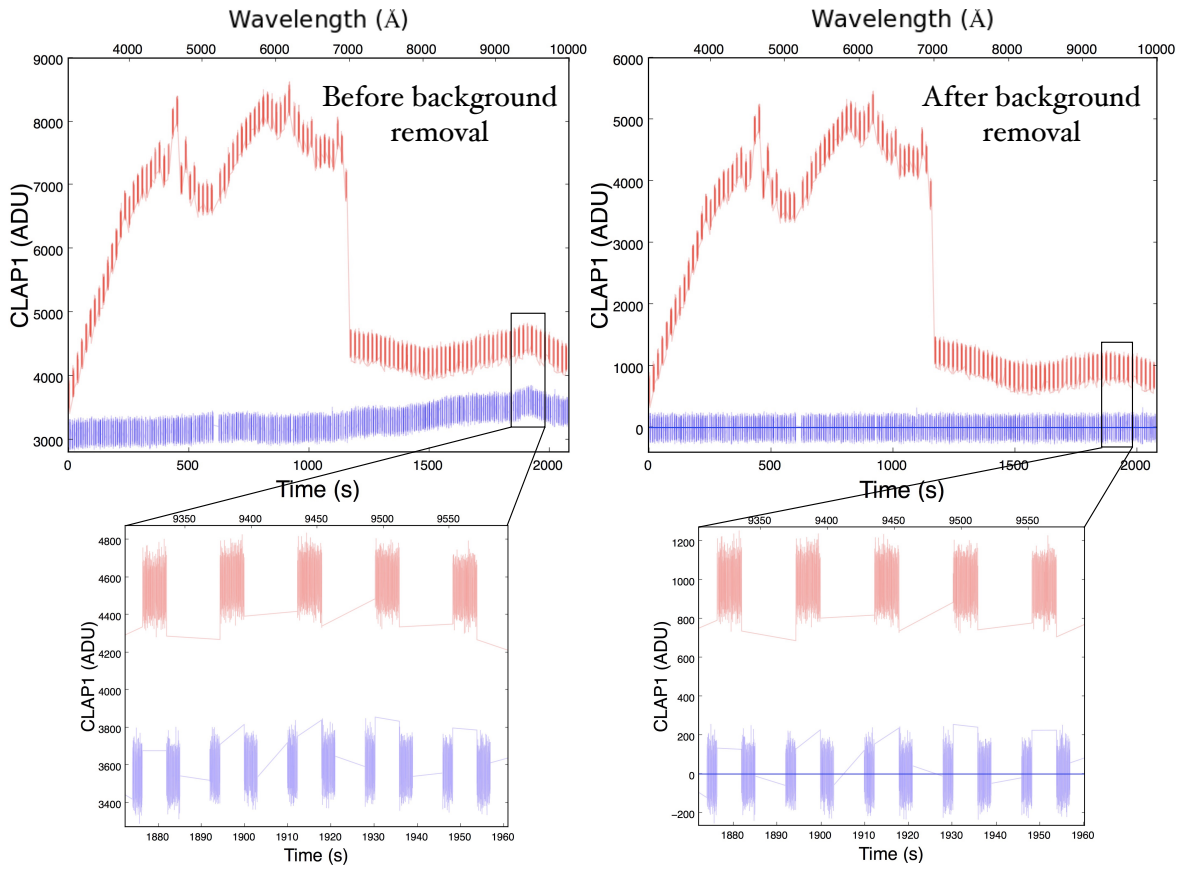

Fig. 7.4 A typical CLAP1 multi-wavelength observation over the entire SCALA wavelength range. The spectrum emitted by SCALA is sampled every 60 Å with 5 s expure times. In blue are the pre- and post-background exposures and in red the signal exposures. The data are plotted against time (lower x-axis) and wavelength observed (upper x-axis). The CLAP1 gain set for these exposures is 43.5. Left: the measurements are shown before background removal and in the bottom there is a zoom of few wavelengths observed. Right: the measurements are shown after the background has been removed from each wavelength individually. In the bottom, there is a zoom of few wavelengths observed. The blue line shows where the zero is.

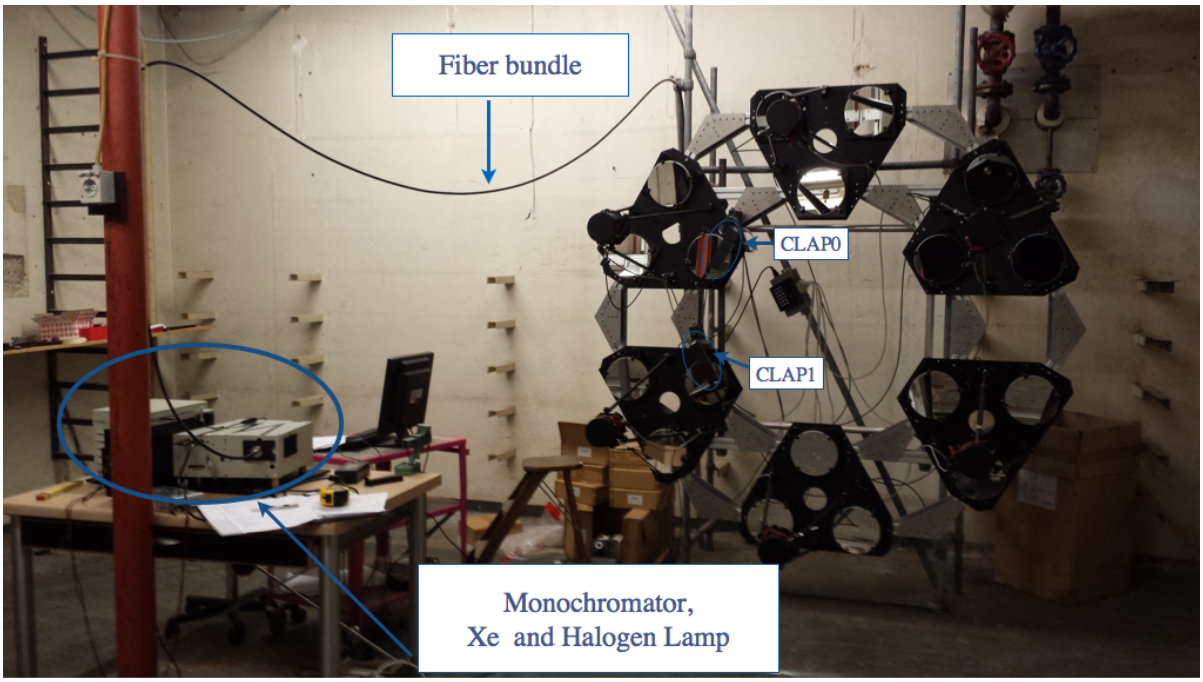

Fig. 7.5 SCALA mounted in the cellar of the physics institute in Bonn. The lamp system with monochromator and fiber bundle are visible on the left and the two photodiodes (CLAPs) are mounted in front of two of SCALA mirrors.

7.3 Lab determination of optimal SCALA exposure times

SCALA produces an artificial planet with a known spectrum. Pre-commissioning observations of this spectrum sampled with monochromatic steps of 30 Å, are extremely useful for, e.g., determining an initial set of exposure times for each wavelength. We want to achieve a mostly constant S/N ratio for every monochromatic SCALA line observation with SNIFS. To have an idea of how many photons SNIFS would collect for each wavelength, we can convert the fluxes measured by the calibrated photodiode. We thus have to scale the photodiode field of view and surface into SNIFS' and combine it with the typical "SNIFS+telescope" response, S_λ. As the CLAPs are calibrated, we can use the responsivity curves in fig. 7.3 to convert the ADUs measured by the CLAPs (as discussed in sec. 7.2) in energy units. More details about this conversion will be given in sec. 9.2.2 and systematics. At this stage we do not need high precision on the conversion between ADU and W, therefore, we simply interpolate linearly the CLAPs responsivity curves in fig. 7.3 to obtain their values in the SCALA central wavelengths observed. After multiplying these energies by 18, under the simplified assumption that every SCALA beam is the same, one can estimate the amount of

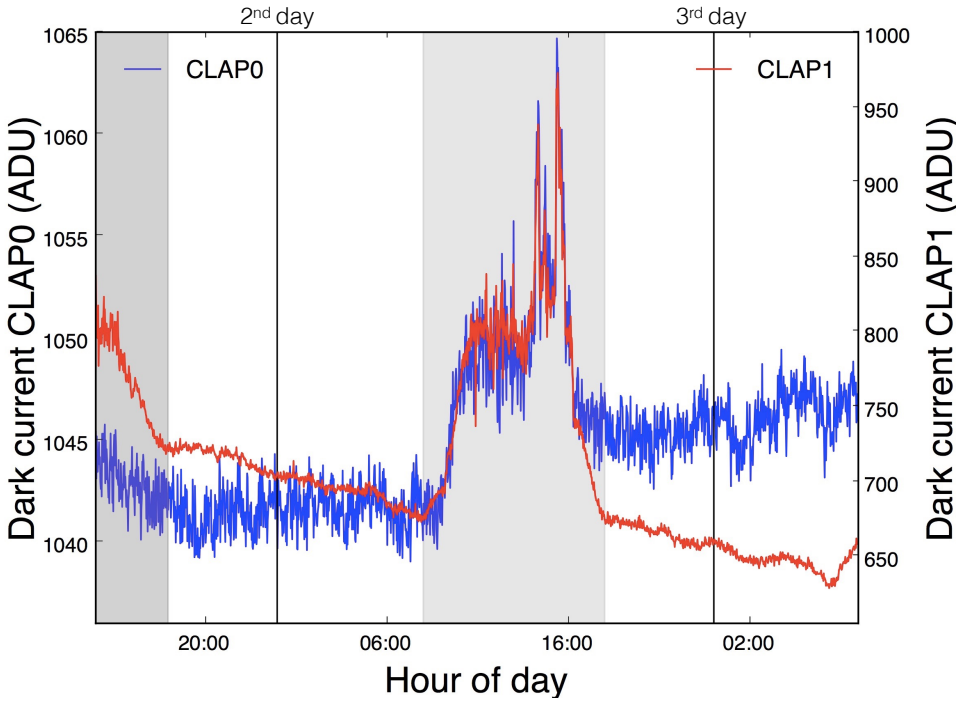

Fig. 7.6 Dark exposures for CLAP0 (in blue) and CLAP1 (in red) plotted against the hour of the day when they were acquired. Usual SCALA light level are around 4000 ADU for CLAP1 and 1300 ADU for CLAP0. The different behavior of the two dark current levels might be due to light leaks evolution affecting the two devices differently since they were located on different mirrors and oriented differently with respect to the light leaks. The gray bands represents the time of the day between 8:00 am and 18:00 pm, when the light leaks are supposed to be more visible.

photons observed in a spaxel of SNIFS in one second, N_{p_λ}, using:

$$N_{p_\lambda} = \frac{C_\lambda[W]}{E'_\lambda}\frac{18}{G}S_\lambda, \tag{7.1}$$

where $C_\lambda[W]$ is the CLAP averaged signal measurement in Watt and E'_λ is the energy of the photon of wavelength λ. Considering the sensitive area of the CLAPs (P_{area}), the aperture angle of SCALA (Ω_{SCALA}), the area of a SCALA mirror (A_{SCALA}) and the field of view of a spaxel of SNIFS (Ω_{spx}), the geometric factor G is:

$$G = \frac{P_{\text{area}} \cdot \Omega_{\text{SCALA}}}{A_{\text{SCALA}} \cdot \Omega_{\text{spx}}}. \tag{7.2}$$

By using eq. 7.1, CLAP observations of SCALA spectrum sampled with 30 Å steps and an ideally perfect response for "SNIFS+telescope" ($S_\lambda = 100\%$), we obtain the flux in units

of number of photons/s/spaxel as shown in the two plots of fig. 7.7. In the top plot of fig. 7.7, the very high and narrow IR emission lines are visible. The presence of these emission lines is the reason why we switch to the halogen lamp above 7020 Å, as mentioned in sec. 6.2.1. These narrow lines would likely be resolved by SNIFS, but not by SCALA's passband, of 35 Å, which would cause many issues in the calibration.

The usage of the halogen lamp in these wavelengths fix this problem as shown in the bottom of fig. 7.7: now, the spectrum looks very smooth on the entire wavelength range scanned, except for few broader and fainter emission lines between 4500-5000 Å, as discussed in sec. 6.4.

We now have an estimate of how many photons per wavelength are observed by each spaxel of SNIFS in a second. By introducing a more reasonable "SNIFS+telescope" response computed from standard stars observations as explained in sec. 5.2.2, we invert eq. 7.1 to obtain the exposure times for every single monochromatic line, such that a signal-to-noise-ratio S/N>100 is reached in SNIFS. This means that every integrated line from SCALA must account for more than 10^4 electrons. With this S/N we would not be dominated by shot noise, which is due to the particle nature of light and follows Poisson statistics. This issue concerns CCDs only, as photodiodes are not single photon counter devices. In fact, for the lowest light level we observe by illuminating a CLAP with SCALA, we anyway count $\sim 10^7$ electrons. The predicted exposure time curve (in dotted black) in fig. 7.8, shows, as expected, an inverse trend with respect to SNIFS transmissivity (in red). In the plot is also shown the effective exposure time (black circles with full line) used for SNIFS observations made during commissioning. The effective exposure times were computed by measuring the number of photons in SNIFS CCDs for several wavelengths and roughly scaling the correspondent exposure time to reach the S/N>100 goal. The predicted data are quite close to the effective ones, only some adjustments were necessary for the exposure times in the IR region.

7.4 CLAPs data reduction steps

For the in-situ CLAPs measurements we perform a more precise data reduction with respect to the steps already described in sec. 7.3. After removing the background level and the cosmic rays (sec.7.2), the data are corrected to account for optical cross talk effect within SCALA. As shown in Küsters et al. (2016), the IS illuminates an area much broader than just the SCALA mirror. This extra light is scattered by the surfaces hit and then observed by the reference photodiode. The overall behavior of this scattered light is measured by closing the IS shutter of the reference beam and by performing a scan through all the wavelengths used for regular calibration. The diffused light measured as a function of wavelength from these

tests, agrees with the reflection properties of black anodized aluminum. This suggests that the light is mostly scattered by the holding structure of SCALA and, thus, can be considered constant over time, as repetition of such tests has confirmed. The correction would have more influence over the IR region, since the cross talk trend is almost flat (around 2% of the light produced) until 7000 Å and then increases linearly up to 6% at 10000 Å.

The reduction steps described until now, i.e. background and cosmic rays removal and optical cross talk correction, are applied to all CLAPs data. After these, however, there are two possible data reduction paths for CLAPs data, depending on our final goal: we can just measure the observed light level as function of wavelengths, or, more generally, we can measure the amount of light emitted integrated over the exposure time, if we are comparing photodiode data with SNIFS exposures of SCALA. The former case will be exemplified in the following chapter (sec. 8.4) and the latter in chapter 9 (sec. 9.2.2).

Whatever is the final quantity we want to measure with CLAPs data, after computing it, we have to convert that (in ADU) into flux units. Since the CLAPs are calibrated, we can convert the ADU in energy units according to the following conversion factor:

$$D^i_m(\lambda_c) = \frac{\int B^i_{\mathrm{SCALA}}(\lambda) d\lambda}{\int K_m(\lambda) \cdot B^i_{\mathrm{SCALA}}(\lambda) \cdot \eta_m d\lambda}, \tag{7.3}$$

where $K_m(\lambda)$ is a linear interpolation of the CLAP sensitivity curve, in ADU/W (fig. 7.3), $m = 0$ for CLAP0 and $m = 1$ for CLAP1, $B^i_{\mathrm{SCALA}}(\lambda)$ is the (triangular) normalized line profile of the SCALA emission and η_m is the CLAP signal gain – 43.5 for CLAP1 and 41.04 for CLAP0 (sec. 7.1). A line profile has been separately measured for each SCALA fiber bundle arm, hence, i goes from 1 to 6. The uncertainties related to the line profiles will be discussed later, in sec. 10.2. The precision of the interpolation for the CLAP calibration curve $K_m(\lambda)$ will be also described there (sec. 10.2.7).

$D^i_m(\lambda_c)$ provides therefore the converting factor from ADU to W, properly weighted to account for the light distribution of the line emitted by SCALA, for the i-th fiber bundle arm and m-th CLAP, computed at the central emitted wavelength λ_c. We can thus multiply the CLAPs measurements in ADU by the appropriate $D^i_m(\lambda_c)$ and convert them into fluxes.

After describing in detail the CLAPs devices, their characterization tests and their data reduction, we show, in the next chapter, how SCALA was mounted in the UH 88 dome and the tests performed during commissioning.

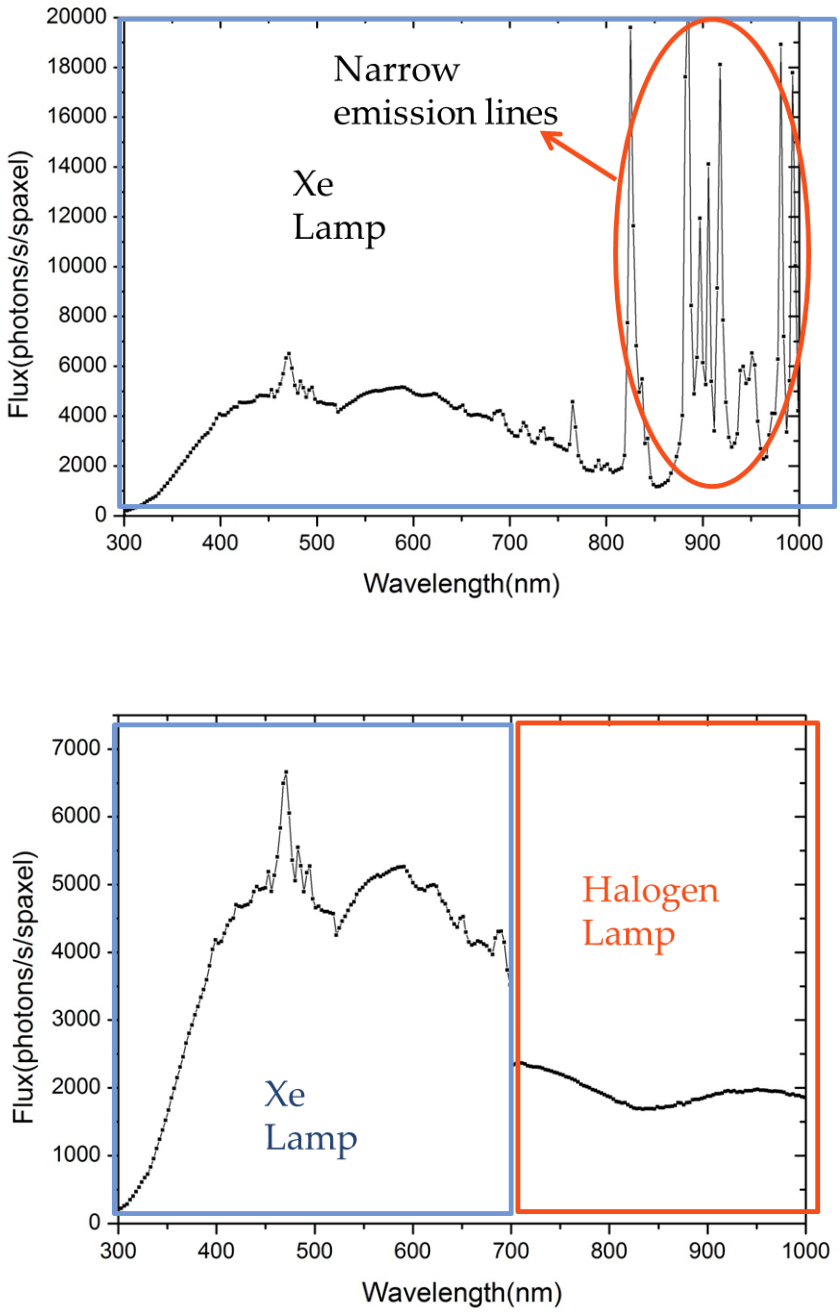

Fig. 7.7 Xe lamp (top) and Xe/halogen lamp (bottom) spectrum from one of the beam of SCALA, measured scanning with steps of 30 Å and monitoring with CLAP1. After converting ADU to energy, the number of photons as observed in a SNIFS spaxel was calculated, assuming that all 18 beams would be the same. The presence of emission lines in the IR region is highlighted in the top plot.

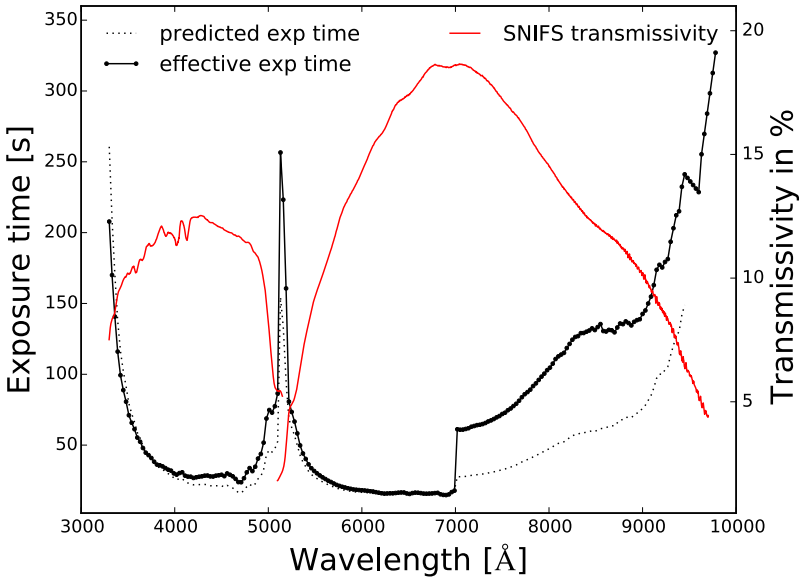

Fig. 7.8 Exposure time for each SCALA line observation with SNIFS predicted (dotted black line) and effectively used (black circles with full line), compared to the SNIFS transmissivity curve in % for February 24^{th} in 2014 (red line).

Chapter 8

SCALA: commissioning, alignment and relative efficiency

SCALA was commissioned in 2014 and fully deployed in 2015. During the 2014 commissioning the entire structure was mounted to a ladder on the inside of the UH 88 dome. This location allowed to keep the structure stable, so that it would not tilt or shake when rotating the dome during observations. The alignment procedure of SCALA with the telescope was tested, as was the controlling software, and other hardware tests were performed. The entire commissioning was performed during down time of the telescope. Even if this was very advantageous for the first installation, it didn't allow observations of standard stars.

We therefore planned another commissioning in 2015 to fully deploy SCALA. We reperformed the alignment, and a general maintenance of the optics (such as cleaning), we upgraded the system installing a mask for the primary mirror, so that the standard stars (that this time was possible to observe) would illuminate the same optical path calibrated by SCALA.

8.1 Alignment procedure

To ensure the correct alignment of all the SCALA optics with the telescope, we mounted a LED light source at the focal plane of the telescope and used its optics to illuminate SCALA with a collimated, parallel beam as fig. 8.1 shows. Such beam was then focused, adjusting the SCALA mirrors, onto the center of the integrating spheres holes, using small shutters mounted on the ISs, as shown in fig. 8.2. These shutters, which can be manually opened and closed to block the light from one hole, have spots painted on the location of the center of the IS hole, to facilitate the alignment.

The alignment of the SCALA optics has been performed in both commissioning phases, in 2014 and 2015, without finding a change the second time except for an overall tilt of the

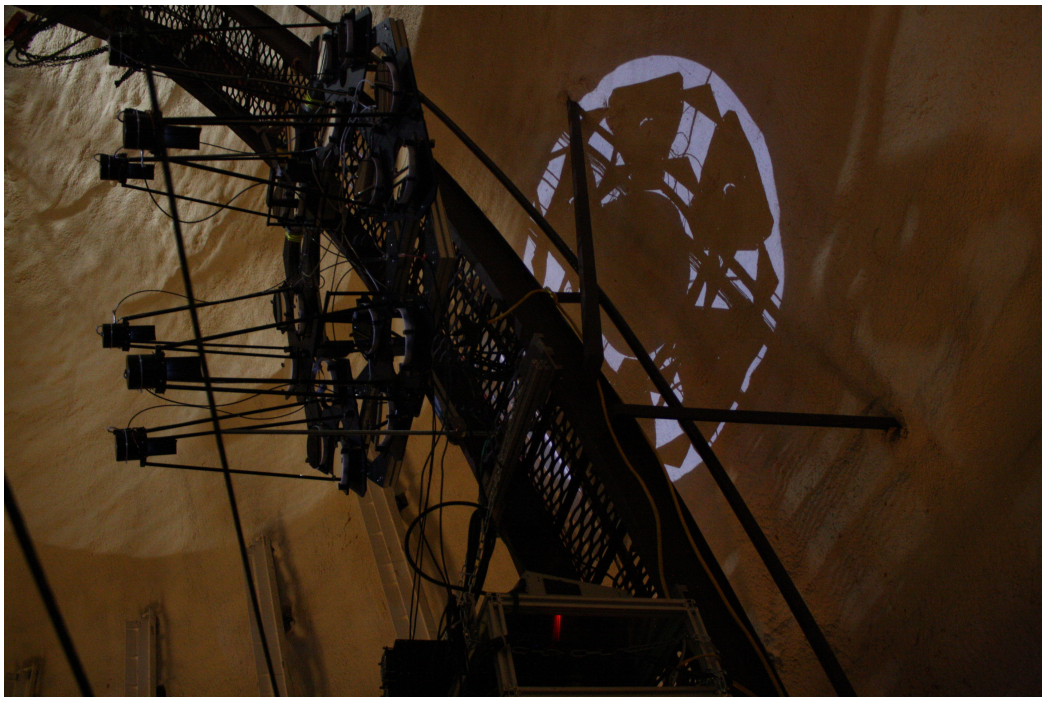

Fig. 8.1 SCALA mounted on the ladder of the UH 88 dome and illuminated by the LED in the focal plane of the telescope. In this configuration the telescope shines a parallel beam as big as its primary, which is visible on the dome wall.

entire structure due to a slightly loose screw, which set the tilt of the SCALA mounting with respect to the dome ladder. We conclude that the alignment of the SCALA optics is very stable.

Placing SCALA on the ladder of the UH 88 dome has advantages, e.g. stability and easy access from the back, but also some disadvantages. For example, the dome rotation is not as precise as the telescope pointing. We, therefore, used the following technique to compensate the intrinsic error from the dome encoder. A rough alignment is made using marks indicating the ideal SCALA position, painted painted both on the dome and the fixed walls below, and, while checking their position with a webcam, we move the dome until they match, allowing a 0.1 degree alignment. We switch the dome power off, to keep it in that position. Then we use SCALA to illuminate SNIFS and take an image with the SNIFS imaging channel in combination with its pin-hole grid. Such grid provides several images of the entrance pupil and one can use the SCALA illumination pattern to slightly move the telescope until it matches with a reference image where SCALA was well aligned. This last step is automatically performed. The software first point the telescope in the SCALA coordinate and then acquire an image of SCALA, illuminated with white light (obtained by setting one grating to 0^{th} order) with the imaging channel and the pin-hole grid filter.

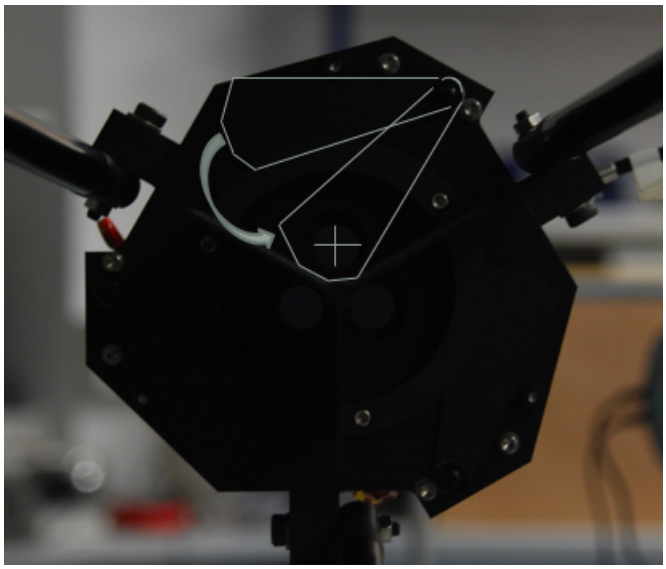

Fig. 8.2 SCALA integrating sphere. The shutters used to close the exit ports of the IS are highlighted with a bright contour, in this picture.

In fig. 8.3 an example of one of the entrance pupil images from the imaging channel+pinhole grid is shown. In the figure SCALA was illuminated with white light and the lights in the dome were on, hence SCALA beams are visible as well as the entrance pupil of the telescope and the SCALA holding structure with the dome ladder.

8.2 Instrument calibration strategy

The ideal way to perform a calibration sequence with SCALA would be to illuminate SNIFS one wavelength per time selecting a wavelength sampling of 30 Å, matching the SCALA passband. However, SNIFS' readout time is 90 s and would make this strategy too time-consuming. Instead, we observe more than one wavelength per SNIFS exposure, as we can use the monochromator's shutter to illuminate the device. However, SNIFS frames would become more crowded with spectra. We, hence, need to select these wavelengths in the best way possible.

The SCALA passband has a nearly triangular shape with a FWHM of 35 Å. We have verified that selecting a separation of 500 Å between the wavelengths observed within one SNIFS exposure yields negligible cross talk issues and overlaps between adjacent wavelengths (Küsters et al., 2016). Furthermore, we avoid crowded images or long exposures with SNIFS, as the maximum number of wavelengths observed per exposure is limited to 4 for the blue channel calibration (3300 - 5000 Å) and to 10 for the red one (5000 - 10000 Å).

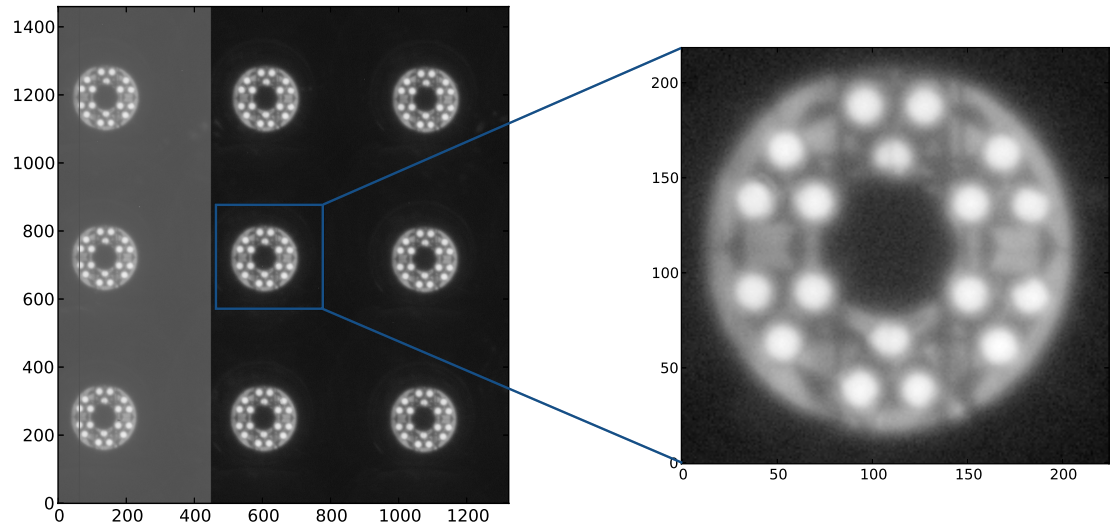

Fig. 8.3 Some of the entrance pupil images from the imaging channel+pin-hole grid are shown with a zoom in on the right for one of them. Illumination of SCALA and the light of the dome switched on allow to see the SCALA beam and the entire entrance pupil with the SCALA hexagonal structure and the ladder of the UH 88 dome. The axis are in number of pixels.

A schematic example of the calibration strategy is shown in fig. 8.4. In this conceptual diagram, background and light exposures are also shown. These belong to the calibrated photodiode measurements only, as previously seen in sec. 7.2. To recap, a SCALA calibration sequence is made of a complete SNIFS calibration with the specified wavelength sampling (from 30 Å on), consisting of several SNIFS exposures (for both blue and red channel) in which some – 4 or 10 – SCALA's wavelengths are observed. A typical SNIFS exposure is shown in fig. 8.5 for a observation of SCALA in the blue channel.

Setting the exposure time for each wavelength observation such that we get $S/N > 10^2$ per spaxel (spatial pixel, or in other words, the pixels illuminated by the same lens of the micro lens array), the overall time required for a complete SNIFS calibration is 8 hrs with typical exposure times from 30s to 180s (as shown in fig. 7.8) per wavelength. However, the flexibility of our acquisition software, allows to considerably reduce the exposure time for a calibration sequence using larger wavelength steps between the different SNIFS exposures. It is possible, for example, to calibrate SNIFS with steps of 150 Å , instead of 30 Å, in less then 2 hours. Even if in this way the wavelength sampling becomes sparser, the data is enough to e.g. monitor system throughput evolution.

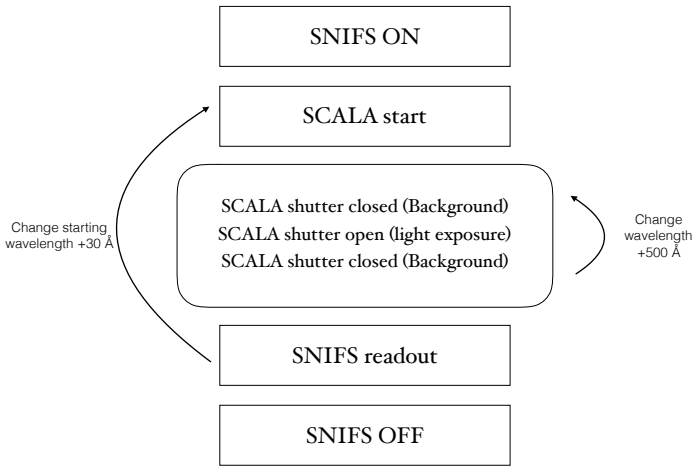

Fig. 8.4 Data taking scheme for the SCALA calibration. The round box refers to the measurements performed by the CLAPs and the rectangular ones to the spectrograph obesrvations. The arrows indicate the logic chain of steps. From Lombardo et al., 2017 (in prep.).

8.3 Commissioning tests

During the two commissioning phases many tests were performed to characterize the calibration device as well as to put limits on possible systematics.

Commissioning 2014

The first commissioning was scheduled during telescope down time. Since we could not observe any standard star during that time, there was no need for the mask to be applied on the primary. After having optimized our controlling software and observing strategy, we tried to obtain some information on the reflectivity properties of the primary mirror.

Several tests involved the calibration of SNIFS using only one module of SCALA to illuminate the primary, and, by changing the module selected, we study how the reflectivity in different parts of the mirror would influence the calibration. We, therefore, closed all the ISs shutters except the three belonging to the same projector module. For these measurements we always had to illuminate at least one of the calibrated photodiode to know the amount of light generated. The modules selected are shown in fig.8.6 and within three nights we performed full SCALA calibration sequences of the following combinations: module 1, module 2 and modules 2+3. Unfortunately during these measurements we experienced several failures of the monochromator shutter due to the cold environment. This inconvenience made the data set acquired mostly unusable, but we are still able to recover some important information. These results will be discussed in sec. 10.3.1.

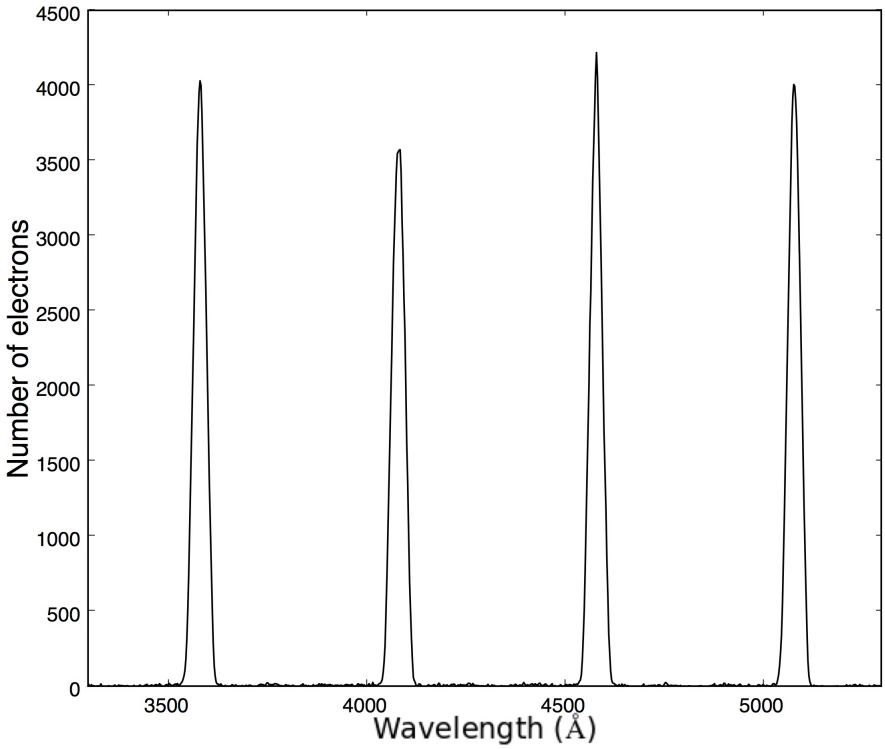

Fig. 8.5 Example of the data obtained for a spaxel of a datacube of SNIFS illuminated by SCALA, for the blue channel. This is a typical exposure where it is possible to notice the 500 Å separation between the different wavelengths observed and also the almost constant number of electrons per wavelength due to the chosen selection of the exposure time for the different wave. The characteristic passband of SCALA with its triangular shape and a FWHM of about 35 Å is also evident. The steps of the data reduction to obtain these kind of data are described in sec. 9.2.1. From Lombardo et al., 2017 (in prep.).

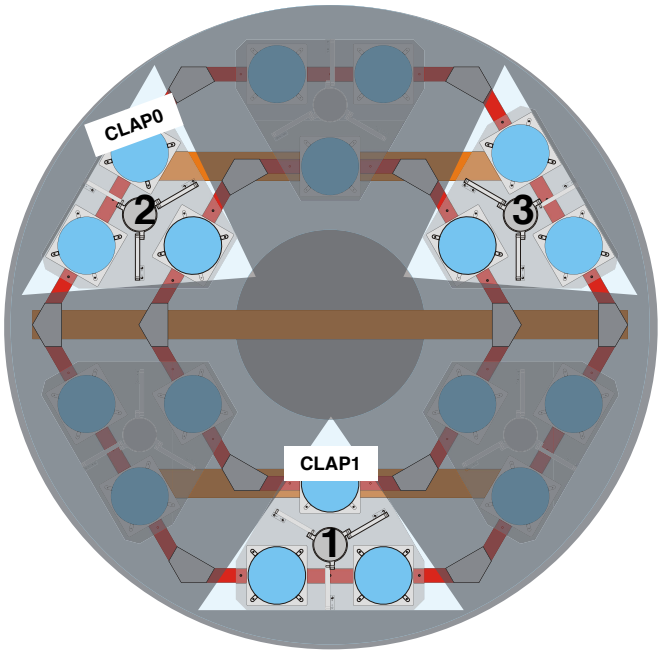

Fig. 8.6 SCALA projector modules selected to test the UH 88 primary mirror reflectivity properties are pointed out by lighter colors. We also indicate the positions where the CLAPs are located.

Commissioning 2015

We performed a set of tests in 2015 to measure the amount of scattered light within the telescopes optics and the spectrograph and to see how these would behave as function of wavelength. The well collimated beams of SCALA are designed to minimize the amount of scattered light, typically one of the most severe issue for calibration units. However, the beam aperture is still of about 1° which can be source of stray light in the internal optics of telescope and SNIFS, whose field of view is much smaller (6.4” × 6.4”).

To study this phenomenon we built a beam reducer – a black anodized aluminum disc with a hole – which make the angular aperture of SCALA beams half the size of the original one. Using SCALA to illuminate SNIFS photometric channel with white light, we produced several flat fielding images with the different SDSS-like filters (u, g, r, i, z) and compared the results between the usage of the reducer (0.5° beam) and the regular case (1° beam). The effect of the stray light is clearly visible from this comparison (Küsters et al., 2016), but it appears as a smooth gradient, with no wavelength dependencies, across the entire field of view of the imaging channel.

We additionally observed a set of SCALA lines, with the spectroscopic channel, with and without beam reducers and with and without mask applied on the primary. These are compared, and evaluated as systematic uncertainties in sec. 10.2.4.

8.4 SCALA relative efficiency

A key step for using SCALA is the determination of the relative sensitivity of the 17 beams not continuously monitored by CLAP1, to that which is. In order to have a proper estimation of the light produced by SCALA and observed by SNIFS we need to quantify the response of each of the 18 beams produced. In conjunction with the planned SCALA calibration sequences we measure this quantity using our two calibrated photodiodes. This is done as follows: CLAP1 is fixed as reference so that it monitors always the same SCALA beam, while the other one is moved to sample each of the remaining 17 mirrors. For each mirror several wavelengths were observed to build a single beam response curve. The scaling factor converting the measured flux by CLAP1 (at one mirror) to what is expected to reach SNIFS can be described as:

$$E_s(\lambda) = 1 + \sum_{i=n=2}^{18} \frac{C_0^{i(n)}(\lambda)}{C_1^n(\lambda)}, \tag{8.1}$$

where C_1^n is the n-th flux measurement by CLAP1 corresponding to the C_0^i flux measured by CLAP0 in the i-th beam; λ is the wavelength. E_s is given in units of the light measured by CLAP1, such that, if all the beams were identical to the reference one, E_s would be equal to 18 for every wavelength.

SCALA mirrors are in an off-axis configuration and there is, therefore, a gradient in the flux across the beam reflected (as mentioned in sec. 6.2.3). This means that the sensitive area of the photodiode experience a different amount of light depending on which part of the beam it is sampling. Hence, we carefully position these detectors to always face the same region of the SCALA beam which is monitored, reaching a reproducibility better than 0.8% in the wavelength range of interest (as shown in sec. 10.2.3). E_s has been measured during the two commissioning phases in 2014 and 2015.

The measured C_1^n and C_0^i are, as mentioned, the fluxes observed by the two CLAPs for each SCALA line. We explained in sec. 7.2 the first steps of the CLAPs data reduction to remove the background level and the cosmic rays, and, in sec. 7.4, how we remove the optical cross talk within SCALA and convert the ADU into flux units. In this section we only need CLAP measurements of SCALA observations and therefore we do not need to consider the exposure times for each wavelength observation. In this case the SCALA observation strategy is exemplified by fig. 7.4. As seen there, a typical SCALA relative efficiency beam measurement thus consists of a scan in wavelengths (upper x-axis) performed linearly increasing with time (lower x-axis) and with a fixed exposure time of 5 s. This is the chosen SCALA calibration strategy in case we are only interested in the data from CLAPs to, e.g., perform systematic tests on SCALA or SCALA relative efficiency measurements.

After removing the background level, the cosmic rays and the otical cross talk from the CALPs data, we compute an average of the data with fully opened monochromator

shutter, which means pure light exposure. We obtain, therefore, a series of data, one for each wavelength observed, in units of [ADU]. We multiply these CLAP0 and CLAP1 measurements by the appropriate $D^i_m(\lambda_c)$ defined in eq. 7.3 – CLAP1 will be always using the same fiber bundle arm line profile ($i = 1$) as it does not move. In this way we obtain the C^n_1 and C^i_0 in flux units and we can compute the SCALA relative efficiency as in eq. 8.1.

8.4.1 SCALA light reproducibility

We can now compare the relative efficiency, $E_s(\lambda)$, as measured with the same quantity calculated based on the lab measurements of individual components. The sum over all 18 beams from eq. 6.4, selecting the appropriate IS, fiber bundle arm and mirror to reproduce the in-situ set-up, is used as estimation of the total light produced by SCALA and represents the component-wise version of eq. 8.1.

The comparison between these measurements of the SCALA sensitivity vs wavelength, provides two important pieces of information regarding our system: how well we control it, comparing the sum over the 18 beams from eq. 6.4 and the quantity from eq. 8.1 as measured during the 2014 commissioning, and its evolution on timescales of a year, comparing the two in-situ measurements from 2014 and 2015.

The laboratory measured sum over the 18 relative responses is shown with green squares in the top panel of fig. 8.7. This curve is compared with the 2014 measurements of the fully integrated system, according to eq. 8.1 (blue circles). The measurements in this plot stop at 7000 Å, since the lamp used for the laboratory tests is a Xe lamp making a comparison with the other data set impossible above that wavelength where the halogen lamp is selected. The measurements have been normalized to their average values since we are only interested in comparing their color trend and not their absolute values. These averages are computed on the wavelength range shown in the plot and are 19.12 and 18.95 for the lab and 2014 curves respectively (Lombardo et al., 2017, in prep.). The trend in both curves fulfills our expectations from sec. 6.4.4 showing a behavior similar to the IS transmissivity (fig. 6.18). As can be seen in fig. 8.7 (bottom panel) the component-wise measurements and the in-situ in 2014 match well within the errors (shadowed area around the line), for the entire wavelength range measured. The mean and standard deviation of the ratio is 1.000 ± 0.004. This shows how well the two curves (after normalization) agree with each other as function of wavelength. Those two measurements were separated by only 2 months and the system did, thus, not evolve in the meantime. The agreement of the curves in fig. 8.7 together with the consideration that they have been measured with independent setups, prove that we are able to reconstruct the wavelength behavior of the SCALA relative efficiency with a precision better then 1%.

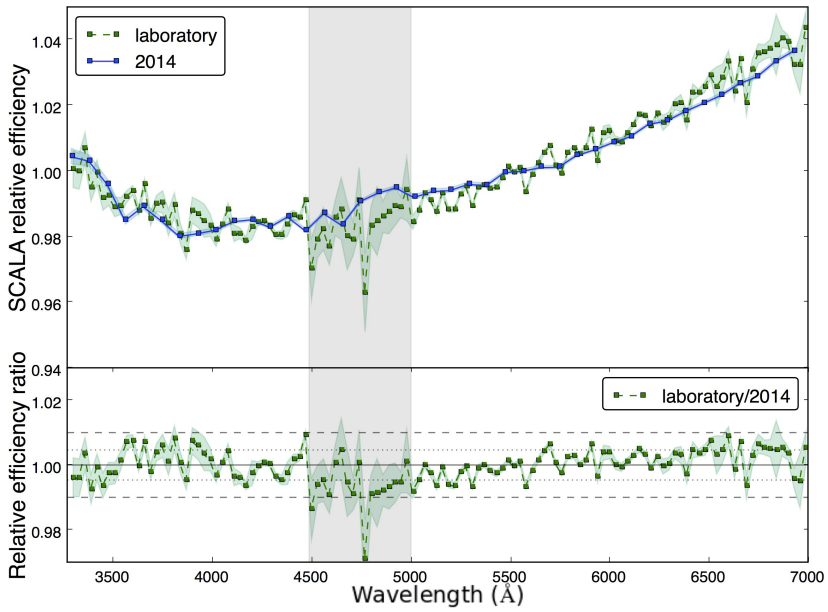

Fig. 8.7 The SCALA relative efficiency, E_s, is shown in the top panel. In green with dashed line is the SCALA relative efficiency estimated from the laboratory measurements, in blue with full line the one from the commissioning in May 2014. Both have been normalized with respect to their average to compare their color trend. The bottom panel shows the ratio between the laboratory measurement and the 2014 commissioning measurements and the dashed gray lines represent the 1% range around the averaged ratio of 1.000 (black full line) and the dotted lines are the standard deviation ($\pm$0.004). The gray band delimits the region where the weak emission lines of the Xe lamp are located (4500-5000 Å). The measurements have been performed with the Xe lamp only and we therefore show these up to 7000 Å. The colored bands around the data are the errors computed as explained in Appendix A.4. From Lombardo et al., 2017 (in prep.)

We can observe an evolution of the system on longer time scales as shown in fig. 8.8, which shows E_s for 2014 (blue circles) and 2015 (red circles), where a difference can be noticed at bluer wavelengths in the 2015 estimation (left panels). These curves (left and right panels) are normalized with respect to their average values of 20.09 and 19.46 for the 2014 and 2015 measurements respectively, computed over the full wavelength range. Note that the SCALA mirrors were cleaned before performing the measurements in 2015 and the reference mirror was cleaned more accurately with respect to the others, due to easier accessibility. Hence, a relative difference between the different beams and the reference beam is expected. From 4700 Å the two curves match again within 1% and this trend is kept also in the measurements above 7000 Å (right panels), with an overall mean and standard deviation of 0.995 ± 0.005 (black full and dotted lines respectively). This evolution might be due to a more accentuated degradation of the reference beam respect to the others. More specifically, a comparison between the responses of the beams belonging to the same IS as

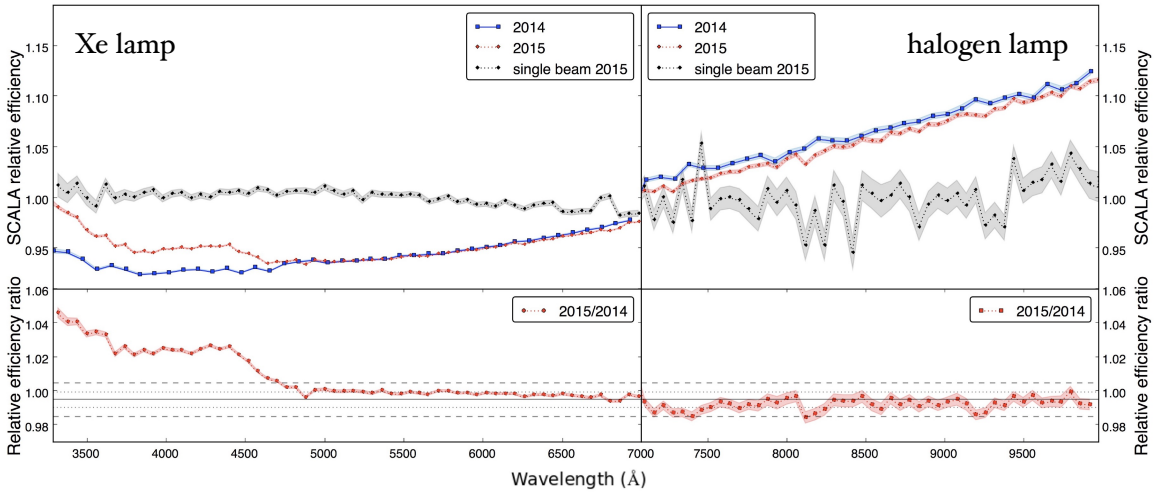

Fig. 8.8 The SCALA relative efficiency, E_s, is shown in the top panels. In blue with full line the SCALA relative efficiency from the commissioning in May 2014 and in red with dotted line the one from the latest commissioning in May 2015. One of the beams illuminated by the same IS as the reference for the 2015 SCALA relative efficiency measurements is with black circles, normalized to its average value. The bottom panels show the ratios between the two commissioning measurements and the dashed gray lines represent the 1% range around the averaged value computed for the measurements from 4700 Å to 10000 Å where a gray offset is present. The dotted lines show the standard deviation ($\pm$0.005). The quantities in the left figure refer to E_s measured with the Xe lamp and so goes only up to 7000 Å. The right figure instead refers to measurements with the Halogen lamp only. The colored bands around the data are the errors computed as explained in Appendix A.4. From Lombardo et al., 2017 (in prep.).

the reference beam do not show a deviation in the blue end, excluding a different degradation of CLAP1 with respect to CLAP0. Instead a color trend appears when the other beams are included in the comparison (more info in Appendix A.3). This suggests that we measure an evolution of the reference IS and/or fiber bundle arm with respect to the others. One of the beams illuminated by the same IS as the reference beam is plotted in fig. 8.8 in black circles with the name "single beam 2015", normalized with its average value of 0.70. We can notice how smooth and mostly achromatic its curve is, suggesting that the two CLAPs did not degraded differently. The larger dispersion on the right hand panel of fig. 8.8 is due to the smaller statistics caused by the lower light level generated by the halogen lamp (see fig. 7.7). For this SCALA relative efficiency measurements we set the exposure time of each wavelength to just 5 s, while for regular SCALA observations the exposure time is adjusted on the light level generated and on SNIFS transmissivity (as shown in fig. 7.8), hence keeping a constant S/N.

The less frequent wavelength sampling of the curves in 2014 respect to the one in 2015 is simply due to a reduced fraction of time devoted to the E_s measurements. In 2015 we opted for a more refined sampling and performed the measurements during three days. We repeated one of the beam measurements twice, once on the first day and once again on the last day, to verify the reproducibility of our measurements. The result of this test is discussed in sec. 10.2.3. We thus conclude that we understand how the SCALA components combine to the full system. We also find that the relative system throughput can change on longer time-scales, and that E_s should be remeasured in connection with any extensive calibration campaign.

Before moving to the next chapter it is worth noticing that the shaded areas around the data in fig. 8.7, 8.8 are the errors of the datapoints computed as explained in Appendix A.4. The errors presented in this thesis are always only statistical. The systematics affecting our measurements are described in a dedicated section (sec. 10.2). The full error propagation and covariance matrix is part of an ongoing thesis work by D. Küsters.

Chapter 9

Observations and data processing

We here describe the SNIFS observations of standard stars that were made during the 2015 commissioning (sec. 9.1), and how the flux calibration from these is compared with the flux calibration from nighttime SCALA measurements (sec.9.2).

9.1 Standard star network observation strategy

During 2015 we observed in the nights from the 3rd till the 7th of June several standard stars and our calibration device. Dividing the nights in blocks of standard stars and SCALA observations allows to track possible evolution of SNIFS during the night and verify its repeatibility.

Due to non photometric conditions (clouds) and telescope issues, the last night of observations, performed with an average seeing of 1.35", was the only one considered suitable for this program. In tab. 9.1 the stars observed during that night are listed together with the number of observations performed during the same night.

The observations of each star was distributed throughout the night to sample a large airmass range (between 1 and 2 for the full sample). Furthermore, care was taken so that stars of different color - i.e. different temperature - also sample this range. In this way we can limit the systematic error on the atmospheric extinction correction computed as in sec. 5.2.2. The consideration of these systematics is a very important part of the standard star network calibration process, which is the final goal for SCALA but not part of this thesis.

The night was subdivided into 5 sections: we initially performed a $\sim$ 2hrs SCALA calibration sequence starting from 3330 Å with steps of 180 Å before twilight, when the influence of ambient light in the dome was already much suppressed, then we opened the dome and performed regular SNIFS star observations for $\sim$ 2hrs. Subsequently we closed the dome and repeated another SCALA calibration sequence with the same steps but starting

Star name	# obs.	airmass
HD93521	2	1.17; 1.19
GD153	3	1.01; 1.03; 1.16
Feige34	2	1.41; 1.72
BD+332642	2	1.26; 1.75
P177D	2	1.21; 1.41
P041C	2	1.61; 1.41
P330E	2	1.15; 1.47
EG131	2	1.13; 1.18
HR7596	1	1.13
BD+284211	3	1.63; 1.19; 1.05
BD+174708	2	1.30; 1.14

Table 9.1 List of stars observed together with regular observations of SCALA during June 7^{th}. On the central and right columns are the number of times the stars have been observed during the same night and their airmasses.

at 3390 Å this time. After that, stars were observed until morning twilight, after which a final SCALA calibration sequence starting from 3450 Å was made.

Adding together all the SCALA calibration sequences performed during the night we can carry out a complete SNIFS calibration sampled with 60 Å steps, which translates into 111 measurements on the instrumental response.

Furthermore, to ascertain the stability of the "telescope + SNIFS" system during the night, the alignment of SCALA with the telescope, and that we do not make any mistake combining the three SCALA calibration sequences, we repeated the observations of a set of SCALA lines during each sequence (these additional observations are called A, B and C). The comparison between these repeated observations is shown and discussed in the systematic section.

In addition to what has already been described for SCALA observations, we also acquired at the beginning of every SCALA observing block an arc exposure plus a raster exposure (as described in sec. 5.2). Moreover, continuum exposures were taken at the beginning and end of the night, such that the usual SNIFS calibration can be run.

9.2 Data processing

We will now discuss the processing of data based on observations of SCALA, first from SNIFS and then from photodiode obsverations. Note that the latter differentiates slightly from what was used during the previously described system tests (sec. 8.4).

9.2.1 SCALA data from SNIFS

The SNIFS calibration pipeline as described in sec. 5.2, was run based on all star observations acquired during the night. The pipeline produces a nightly flat fielding datacube, by combining the continuum exposures of the night, and a flux solution which convert electrons in flux units. This flux solution corrects for the instrumental response, assumed constant during the night, and is applied together with the nightly atmospheric extinction, which is airmass dependent. The atmospheric extinction is fit by the model from Buton et al. (2013) at the same time as the instrumental response. The degeneracy between instrument and atmosphere is broken by the airmass dependency of the latter. Any systematic residuals in the atmospheric extinction model is thus incorporated in the instrumental response. If we are interested in a comparison of this instrumental response with the one derived from SCALA observations, some systematic differences are expected. For SNIFS flux calibrated data, this is not a problem since the atmospheric extinction and instrumental response are never used separately.

There are two kinds of data that we want to produce to exploit SCALA observations from SNIFS: wavelength calibrated data, to compute the throughput of the system, and flux calibrated data to have a direct comparison of the two calibration techniques (from standard stars and from SCALA). Both will be better explained later in this section.

The initial steps of the SNIFS data reduction of SCALA observations are performed according to the pipeline (see sec. 5.2) up to the wavelength calibration (step 3). The arc exposure, acquired before starting the SCALA observation, is used to achieve the wavelength calibration of SCALA data as in the usual pipeline and the raster exposure – acquired immediately after the arc – to correct for transmissivity variations due to the dichroic (this is used in a later stage of the production after wavelength calibration, step 4).

These wavelength calibrated data present cosmic rays, which would make the analysis much harder and possibly biased. We can eliminate the problem following the pipeline for two further steps: we, first, apply the flat fielding datacube (step 4), then we can run the cosmic rays removal script (step 5), as usual, and finally we reapply the inverted flat field, to obtain cosmic ray cleaned and wavelength calibrated datacube, i.e. 225 spectra. Note that the dichroic correction has not been applied to these data. An example of data from SNIFS, produced in this way, was shown in fig. 8.5.

For the flux calibration we perform the steps described above, but we avoid reapplying the inverted flat field. Instead, we apply the dichroic correction and the flux solution of the night computed by the standard stars observation (as described in the previous section). Considering that the atmospheric model depend on airmass, we set the airmass value of SCALA data to zero so that no atmospheric extinction will be used in this case. This is

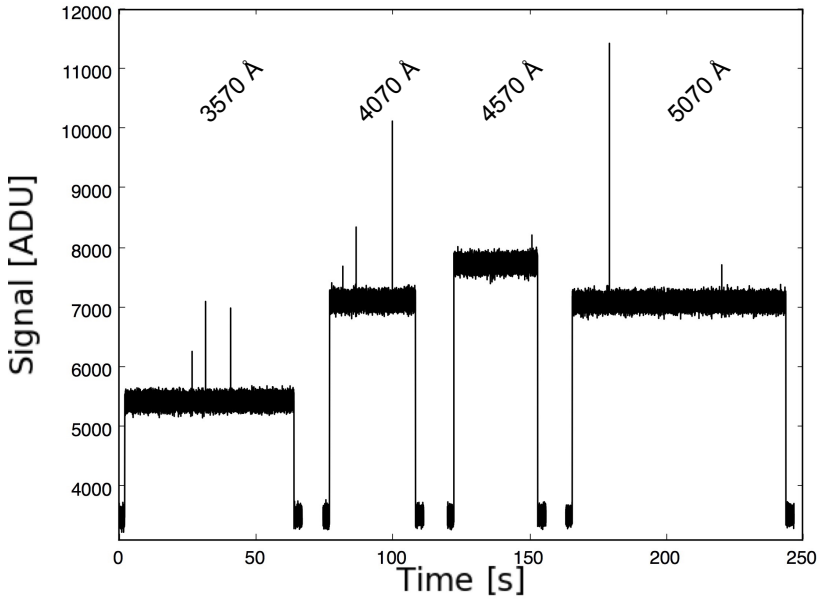

Fig. 9.1 Example of the data obtained from CLAP1 for four wavelength exposures. Notice the different exposure time for each wavelength, depending on the light level and SNIFS sensitivity, and also the presence of about 2 s background exposures before and after observing a wavelength. The big outliers in the data are cosmic rays which are subsequently removed by the analysis software. The numbers above each of the exposure are the wavelengths observed. This observation matches the SNIFS exposure shown in fig. 8.5. From Lombardo et al., 2017 (in prep.).

the last step to obtain flux calibrated SCALA datacubes from the spectrograph in units of erg/cm^2/Å/s.

All the steps described in this section are performed by a dedicated script which uses all the sub-blocks of SNIFS pipeline and it is written to specifically handle SCALA data.

9.2.2 SCALA data from photodiode

The reference photodiode data face a different kind of processing. As discussed above (sec. 8.2), each SNIFS exposure combines multiple wavelengths as shown in fig. 9.1. The light level from SCALA is continuously recorded together with the two background exposures which precede and follow it. Note that we here use the strategy where exposure times are adjusted to reach similar signal-to-noise levels, as described in sec. 7.3.

As in this section we are interested in comparing CLAPs and SNIFS observations of SCALA, we only process CLAP1 data. The steps for cosmic rays and background level removal and optical cross talk correction described in sec. 7.2 and 7.4 are performed.

The photodiode data – still in ADU units – are integrated with Simpson method including background and light exposures. We are also able to account for the rising and falling ramp due to the monochromator shutter opening and closure. A description of the error on this procedure is in sec. 10.2.5. This step is particularly important as SNIFS integrates over the entire exposure time, which includes many wavelengths (as described in sec. 8.2), and thus cannot yield the specific exposure time of single wavelengths. We could in principle use the requested exposure time, but this would be sensitive to systematic errors in the effective monochromator shutter time. Only the CLAP data can, therefore, provide the information needed to scale SNIFS data for each wavelength observation. Note that we do not need to explicitly measure the exposure time and scale SNIFS data with it, as we already integrate CLAP1 data over time.

After integration, we obtain data for each wavelength observed, in units of ADU·s and we can convert them in units of energy J by multiplying with D_λ from eq. 7.3. We are now ready to compare the information from the spectrograph and the photodiode as detailed in the following section.

The error propagation on the background removal is computed as explained in Appendix A.1 and to each data (first background exposure, light expose and second background expose) a variance is assigned according to eq. A.3. These errors are propagated through the integration with the composite Simpson's rule (Appendix A.5) and finally combined with the errors on D_λ from the linearly interpolated errors on the responsivity curve of CLAP1.

9.2.3 SCALA data products

The main goal of SCALA is to perform an independent measurement of the throughput of the "telescope + SNIFS". This is accomplished by comparing SNIFS observations of SCALA with the simultaneously obtained CLAP measurements according to the following equation:

$$T_{\lambda_i,\mathrm{spx}} = \frac{\int I^W_{\mathrm{SNIFS}}(\lambda_i,\mathrm{spx}) E'_{\lambda_i} d\lambda}{C_{1_{\lambda_i}} \cdot D_{\lambda_i}} \cdot \frac{G}{E_{s_{\lambda_i}}} \cdot X, \tag{9.1}$$

where $I^W_{SNIFS}(\lambda_i,\mathrm{spx})$ is the SCALA intensity in each spaxel spx in number of electrons from the wavelength calibrated datacubes produced as described in sec. 9.2.1 and E'_{λ_i} is the energy of a photon of wavelength λ_i; C_1 is the integrated light (over the SCALA line exposure time) from the reference CLAP produced as described in sec. 9.2.2; D_{λ_i} is the conversion factor from eq. 7.3; G is the geometrical factor in eq. 7.2; $E_{s_{\lambda_i}}$ is the SCALA relative efficiency as in eq. 8.1. Finally X is the unknown factor due to the different reflectivity of the non sampled parts of the primary mirror respect to the sampled part illuminated by SCALA (is not expected to, but could, depend on wavelength). As we here observe SCALA and the

primary standard stars with a mask applied on the telescope (sec. 6.2) so that they illuminate the same patches of the primary mirror, we can remove the term X.

Once scaled for the SCALA mirror and CLAP area, the factor $C_{1_{\lambda_i}} \cdot E_{s_{\lambda_i}}$ provides the total illumination generated by SCALA as function of wavelength, since, essentially, $E_{s_{\lambda_i}}$ is given in units of $C_{1_{\lambda_i}}$.

If we, instead, wish to make a direct comparison of the final flux calibration (sec. 9.2.1) we get the equation:

$$R_{\lambda_i,spx} = \frac{\int I^F_{\mathrm{SNIFS}}(\lambda_i, \mathrm{spx}) d\lambda}{C_{1_{\lambda_i}} \cdot D_{\lambda_i}} \cdot \frac{G'}{E_{s_{\lambda_i}}} \tag{9.2}$$

which fulfills the relation:

$$R_\lambda = \frac{T_\lambda}{S_\lambda}, \tag{9.3}$$

where $I^F_{\mathrm{SNIFS}}(\lambda)$ is the SCALA flux calibrated intensity, T_λ is defined in eq. 9.1, S_λ is the instrumental response estimated by the SNIFS pipeline using standard star observations (derived as described at the end of sec. 5.2.2), and $G' = G \cdot A_{\mathrm{tele}} \cdot 10^{-7}$ is the same geometric factor as before multiplied by the UH 88 primary mirror area, A_{tele}, and by the factor to convert erg in J (the SNIFS flux calibration is given in ergs, while the calibrated CLAP unit is J).

In the next chapter we show the results achieved analysing SCALA data according to eq. 9.1 and eq. 9.2 and discuss the systematics affecting these quantities.

Chapter 10

Results

In this chapter we present the transmissivity measurement of the "SNIFS+UH88" system obtained from SCALA observations (sec. 10.1). We then describe and constrain the main sources of systematic errors affecting the measurements (sec. 10.2). As we, in conjunction with the SCALA measurements, also observed standard stars we next compare the SCALA flux calibration with that of the standard SNIFS pipeline (sec. 10.3).

Finally, we describe the possible usage of the SCALA calibration device (sec. 10.4).

10.1 Throughput

We here show the SCALA flux calibration derived from measurements made June 7th 2015. While SCALA observations were made during several nights, this is the only night with photometric conditions, SNIFS fully operational and we experienced no monochromator shutter failures.

The observation strategy used during that night splits the time between standard stars and SCALA observations, as described in sec. 9.1. The throughput measurement is accomplished comparing the observations of SCALA made by SNIFS, with the reference light recorded by the CLAP (eq. 9.1), where we use the SCALA relative efficiency from 2015 (red curve in fig. 8.8). By averaging the throughput measurements over all spaxels in SNIFS, we obtain the mean throughput shown in fig. 10.1. This curve combines the data from the three blocks of SCALA-calibration-sequences (acquired as explained in sec. 9.1).

Fig.10.1 illustrates the main features of SNIFS' transmissivity: the fast decline in the transmission of both channels in the region where the dichroic splits the light between them (5000 - 5300 Å), and the dichroic features in the blue channel, between 3900 and 4200 Å, which look like a series of small wiggles in the throughput curve. In the regions affected by the dichroic features, the transmission is variable during the night. This variability is

corrected by the SNIFS pipeline (step 4 in sec. 5.2.1), but in the case shown in fig.10.1 the data have not been fully processed and the dichroic features have not been accounted for.

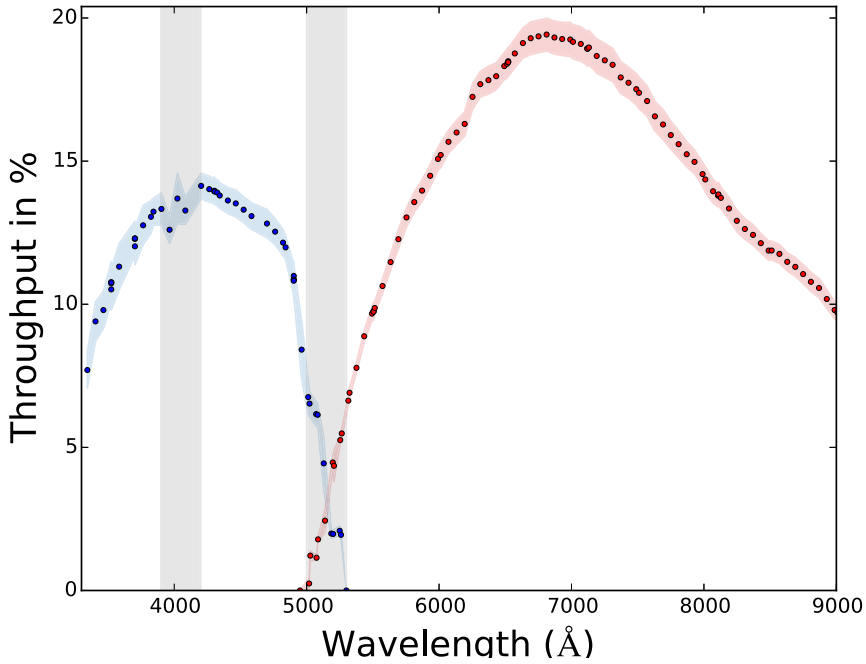

Fig. 10.1 The nighttime throughput $T_{\lambda,\mathrm{spx}}$ averaged over the spaxels is shown as per-cent of the incoming flux. The blue and red circles represent the throughput measured by illuminating the telescope+spectrograph (blue and red channel respectively) with SCALA. The colored bands indicate the throughput variation between SNIFS spaxels (the standard deviation), and are thus *not* an estimate of the throughput uncertainty. The gray bands represent the region affected by the dichroic features. From Lombardo et al., 2017 (in prep.).

The colored bands around the data in fig. 10.1 are the standard deviations of the average over the different spaxels and are, thus, not the errors on the measurements. In fig. 10.2 the contributions to the relative statistical uncertainty on the throughput are shown. In blue is the contribution due to the term $C_{1_{\lambda_i}} \cdot D_{\lambda_i} \cdot E_{s_{\lambda_i}}$ from eq. 9.1, that provides the wavelength dependency of the light generated by SCALA (from CLAP data). The plot illustrates that the error is smaller than 0.2%. The statistical error of SNIFS observations (i.e., the factor $\int I^W_{\mathrm{SNIFS}}(\lambda_i, \mathrm{spx}) E'_{\lambda_i} d\lambda$ in eq. 9.1) is <0.5% and plotted in red, for one spaxel. This error is due to photon counting statistics (error $= \sqrt{N_p}$ where N_p is the number of photons). The data in red show a parallel trend. This behavior can be easily explained considering that the exposure time of the last SCALA sequence (the morning block) have been erroneously set to be 1.5 times smaller than the default. As consequence the statistical error on these measurements become larger. The total statistical error on the throughput (in green) is mostly following the statistical error on the SNIFS data and it is <0.6%.

In the following section we describe the main systematics affecting the measurements and their upper limits.

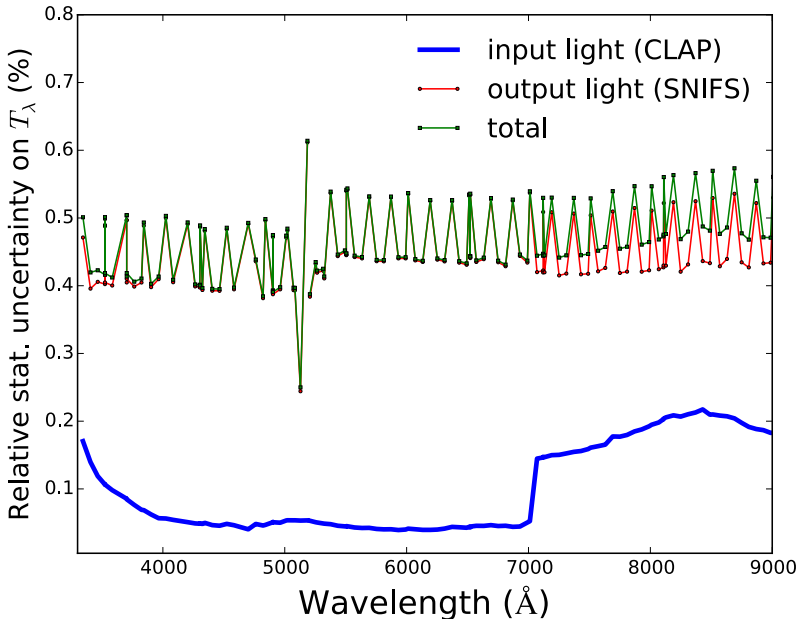

Fig. 10.2 Relative statistical error contributions to the throughput, for CLAP (blue full line) and SNIFS measurements (red circles) are plotted in %. The first is the error on the light level measured by CLAP1, converted in flux units and scaled to account for the other 17 SCALA beams. The red circles are the errors on the flux measured by SNIFS as function of wavelength for one spaxel (#97 is plotted here) due to photon counting statistics. In green squares is plotted the complete relative statistical error on the throughput.

10.2 Systematics

Our calibration precision is ultimately limited by the reference system used: the CLAPs are calibrated by the DICE team (Regnault et al., 2015), as described in sec. 7.1, and have uncertainties – mostly dominated by the NIST photodiode calibration uncertainties – around 0.74% between 3200 and 3400 Å, then <0.32% up to 4700 Å and <0.18% between 4700 and 9500 Å. In this we have assumed that the 2σ uncertainties quoted by NIST are Gaussian, so we can convert them into 1σ uncertainties.

In Table 10.1 we summarize the other systematic errors that contribute to the total error budget. In the following subsections each contribution will be discussed in more detail. A full calculation of the (correlated) systematic errors will be presented by Küsters et al. (in prep.).

From the elements composing equation 9.1, the biggest contribution to the error is due to the SCALA relative efficiency, E_{s_λ}, estimation. As E_{s_λ} is determined in different conditions,

Systematics	σ_T/T
Ambient light on SCALA relative efficiency	<0.5%
Wavelength uncertainty	<0.2%
SCALA relative efficiency stability	<0.7% $\lambda < 4700$ Å <0.02% $\lambda \geq 4700$ Å
Stray light on 0.5° beam	<0.4%
CLAP integration over time error	<0.07%
Optical cross talk in SCALA	<0.05%
Optical cross talk in SNIFS	<0.1%
SCALA and SNIFS reproducibility	0.3% $\lambda \geq 4000$ Å 2% $\lambda < 4000$ Å

Table 10.1 List of systematic uncertainties that contribute to the total uncertainty on the throughput measurements. From Lombardo et al., 2017 (in prep.)

this is subject to several additional potential sources of contamination. This particular set of measurements has been performed in rather different conditions than the usual ones, making it subject to several sources of contamination:

- since the measurements were made during daytime, they can have ambient light contamination,
- wavelength uncertainty caused by the monochromator reproducibility,
- reproducibility of how well we can place the photodiode on the same region of each mirror.

Some of these systematics are also present in nighttime observations, but at a reduced level. Additionally these data will also have lower statistics due to shorter exposure time (hence less data). In the following we will describe the systematics, both for the nighttime and daytime measurements, and also the systematics related to the other elements of equation 9.1 (and 9.2).

10.2.1 Ambient light contamination

The throughput measurements (fig. 10.1) were performed mostly during nighttime and with the telescope dome closed. Ambient light (or background light from other illumination sources in the room) contamination can, therefore, be neglected in the calibrated photodiode data analysis.

On the other hand, $E_{s_{\lambda_i}}$ was measured during daytime and, therefore, dome light leaks could create varying levels of ambient light contamination.

There are two cases that can occur: diffuse and scattered ambient light that smoothly drifts with time, and scattered ambient light that quickly varies on a time scale of seconds, probably modulated by clouds crossing the sky. The former case, appearing on time-scales longer than individual SCALA line exposures, can be accurately accounted for using the CLAP background measurements as shown in sec. 7.2. Hence, it does not affect the accuracy of the calibration. This situation is always attained during nighttime measurements, where we only have dark current variations, and during daytime when the weather conditions are stable. For these cases the background measurements before and after the light exposure (fig. 9.1) are representative of the dark current and ambient light level during the light exposure, reaching a precision better than 0.7% in the background removal (Küsters et al., 2016).

The case of quickly varying background light, on the other hand, is more complicated to handle. To estimate this uncertainty we have obtained a series of daytime measurements where the CLAPs are continously monitoring the amibent light in the UH 88 dome. We can test the precision of the background reconstruction by artificially dividing these data into background and signal, and measuring how well we subtract the background – in this case how close to zero counts we get. A full description of these tests can be found in Küsters et al. (2016), we here only summarize the results. We confirm that most background variations are slow, but that occasional faster modes exist (see fig. 10.3). Fortunately, fast variations with non-optimal background removal are all found to be strongly correlated between the two CLAPs. Thus, taking this correlation into account we found that the total error on $E_{s_{\lambda_i}}$ (which is a ratio between data from the two CLAPs) can be constrained to 0.5%

10.2.2 Wavelength uncertainty

SCALA produces monochromatic light through a monochromator, for which the wavelength reproducibility is declared to be about 1 Å from the manufacturer. For the SNIFS system throughput estimation we use the wavelength calibration from SNIFS data to evaluate the central wavelengths observed, therefore this error doesn't directly appear in the systematics budget (the wavelength uncertainty of SNIFS, estimated through arc exposures, is negligible).

The monochromator wavelength uncertainty is, however, present in the determination of the SCALA relative efficiency E_{s_λ} since these measurements are not accompanied by SNIFS exposures.

We used the SNIFS wavelengths calibration to verify the stated wavelength precision, comparing the central SCALA wavelengths estimated from a set of SNIFS exposures with the ones requested to the monochromator (recorded in the header of the photodiodes). They follow a linear trend, which can be fitted for the blue and red wavelengths as shown in fig.10.4 (top and bottom plots) together with their residuals (bottom panels in each plot).

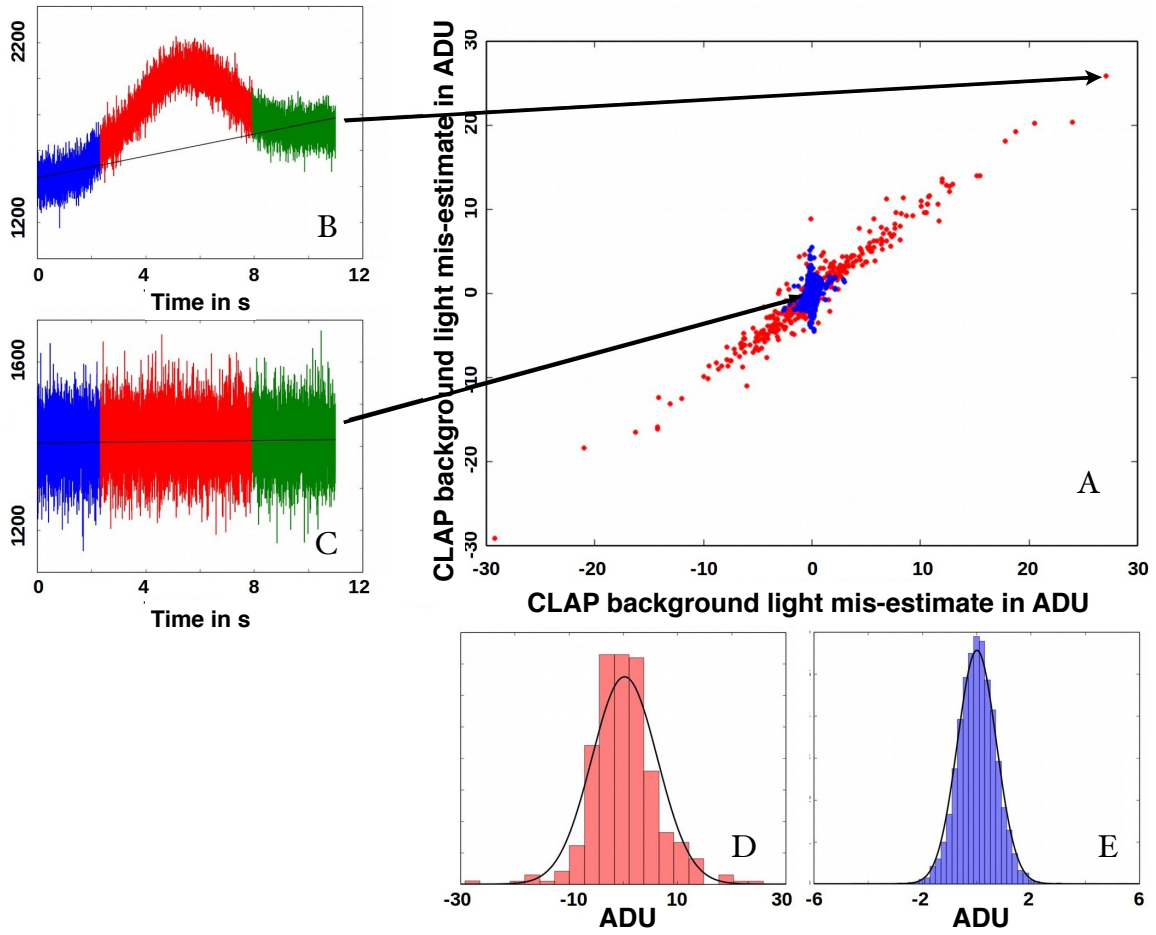

Fig. 10.3 Results from ambient light measurements. A: Comparing the residuals of background estimates for the two CLAPS (one on each axis). Blue points highlight low-amplitude residuals from slow background variations. Note that these constitute 95% of the sample, but are all overplotted in this graph. Red points show large amplitude variations due to variations on similar time-scales as exposures - these are strongly correlated between CLAPs. B: Example of rare ambient light fluctuations where the linear background removal (black line) leaves a residual (systematic) background component. Blue and green shows the pre- and post-light background, red region the time when an exposure would have been made. C: Example of standard, slowly changing, background conditions. D-E: distributions of the mis-estimates of the high-and low-frequency background variations respectively. The standard deviation in D is 6.1 ADU and in E 0.7 ADU where the minimum light level for measurements is 100 ADU. From Küsters et al. (2016).

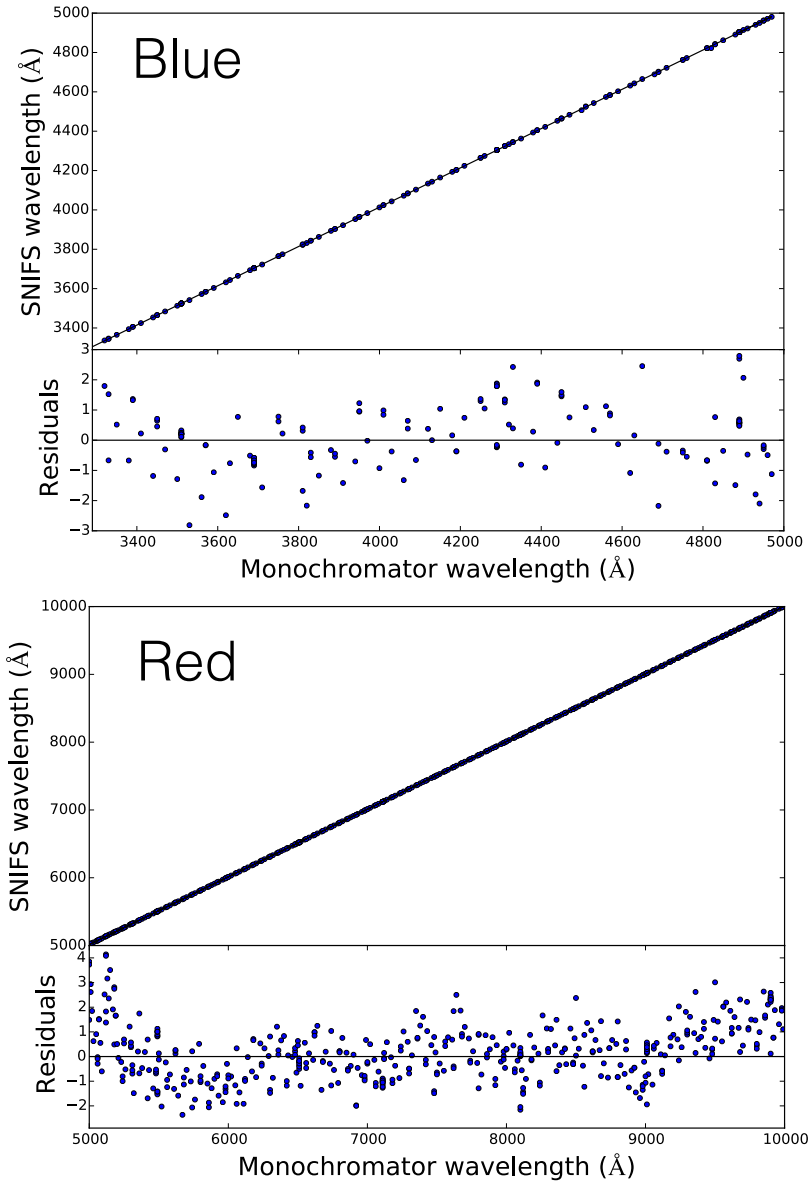

Fig. 10.4 Wavelengths estimated by the SNIFS exposures for the blue channel, on the top, and the red channel, on the bottom, vs the ones requested to the monochromator, plotted together with the linear fit (black line going through the points). Lower panel in each plot: residuals of the linear fit centered around zero (black line). The values for the fits are: slope$= 0.9984 \pm (2 \times 10^{-4})$ and intercept$= 19.87 \pm 1.02$ for the top plot, and slope$= 0.99836 \pm (5 \times 10^{-5})$ and intercept$= 22.87 \pm 0.39$ for the bottom figure. The errors on them are computed as in eq. A.2. From Lombardo et al., 2017 (in prep.)

Even though the monochromator is highly reproducible, we consider as conservative wavelength error estimate ± 3 Å (twice the standard deviation of the residuals) corresponding to the maximum value of the residuals. Such error does not constitute an issue in the E_{s_λ}

measurement (E_{s_λ} only requires wavelength reproducability) since we obtain the same result within 0.2%, when recomputing it using a wavelength increased (or decreased) by 3 Å.

10.2.3 SCALA relative efficiency stability

We have tested the reproducibility of the SCALA relative efficiency in 2015, $E_{s_{\lambda_i}}$, by repeating the measurement of one of the 18 SCALA beams at the start and end of the four days test run. We call these measurements α and β respectively and they represent the ratio between the moving photodiode and the reference one. The α run was made directly in connection with the nighttime SCALA calibration, and we thus wish all relative efficiency measurements to match this.

The mean reproducibility is excellent, having a mean of 0.999 (blue line in fig. 10.5) with standard deviation ± 0.008. The measurements on the reddest wavelength range are noisier since they have low flux levels. These fluctuations are further suppressed when all 17 beams are combined. In regular nighttime observation for wavelengths with lower intensity emission we expose longer, and this maintains a constant S/N. When measuring the SCALA relative efficiency, such long exposure times are not feasible as the measurement has to be remade 18 times (once for each non-reference beam + the reproducibility sequence). We here use a constant exposure time of 5 s per wavelength.

Signs of a possible system evolution on shorter time-scales (days) exist at the blue wavelength end as the ratio between α and β shows a 0.8% difference between 3200 and 4700 Å (see fig. 10.5). Since measurements of beams from the same (reference) module do not show any evolution (as shown in fig. 8.8), a relative evolution between the IS+fiber bundle combination belonging to the reference module with respect to the other modules is the likely explanation (see sec. 8.4.1). Note that SCALA relative efficiency measurements were performed in a mixed order – not module by module – and the reference module beams were measured on the second day.

The SCALA relative efficiency is used to correct the nighttime SCALA measurement of June 7th. From fig. 10.6, we see that CLAP data from this night mostly agree – or show a much smaller deviations than the one in fig. 10.5 – with the α run (note that the CLAPs were kept fixed during these observations). The source of this evolution at blue wavelength is currently being investigated. For the sake of computing an error, as β was the final measurement made, we can use this ratio as a (relative) systematic error. This systematic error is propagated to each of the SCALA beam measurements, except for the two beams that belong to the reference module and thus are illuminated by the same fiber/IS path. As each beam ratio has a similar amplitude, the total error on the SCALA relative efficiency is of the same order as the one from a single beam. The final error, after combining all beams, is 0.7% for wavelengths <4700 Å.

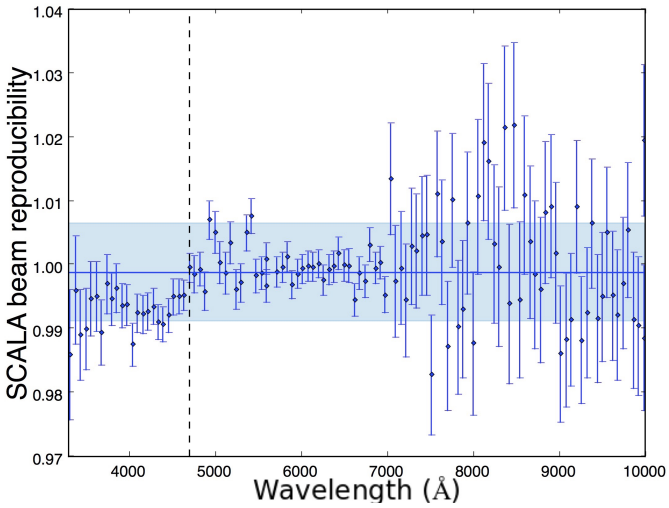

Fig. 10.5 Ratio between the same SCALA beam measurements, α/β. The shaded blue region is the standard deviation, ± 0.008, of the points around the blue line that represents their average of 0.999. The vertical dashed line at 4700 Å separates the region where the offset is found. Lombardo et al., 2017 (in prep.)

10.2.4 Stray light

The well-collimated beams of SCALA are designed to minimize the amount of scattered light. However, the beam aperture is still 1°, which might be a source of stray light in the internal optics of SNIFS. Note that all telescopes will have some amount of stray light, and the error we consider is thus the difference in stray light between a point source and a 1° beam.

To study this question we use a beam reducer – effectively a smaller aperture in the IS output ports – to reduce the SCALA angular aperture to half its original size. Using SCALA to illuminate the SNIFS photometric channel with white light, we produce several flat fielding images in the different filters (u, g, r, i, z) and compare the results between the usage of the reduced 0.5° beam and the regular case 1° beam.

The effect of the stray light is clearly present, but it appears as a smooth spatial gradient, with no wavelength dependencies, across the entire CCDs of the imaging channel (see full discussion in Küsters et al., 2016).

We also observed a set of monochromatic SCALA lines with and without beam reducers using the spectroscopic channels of SNIFS. The ratios between these measurements are shown in fig. 10.7. The mean ratio is offset form 1, thus confirming finding some amount of scattered light (as in Küsters et al., 2016). However, we again find that any wavelength dependency to the scattered light is small (well below 1%). A linear trend growing from blue to red wavelength (in fig. 10.7) is still $< 0.4\%$ over the wavelength region of interest.

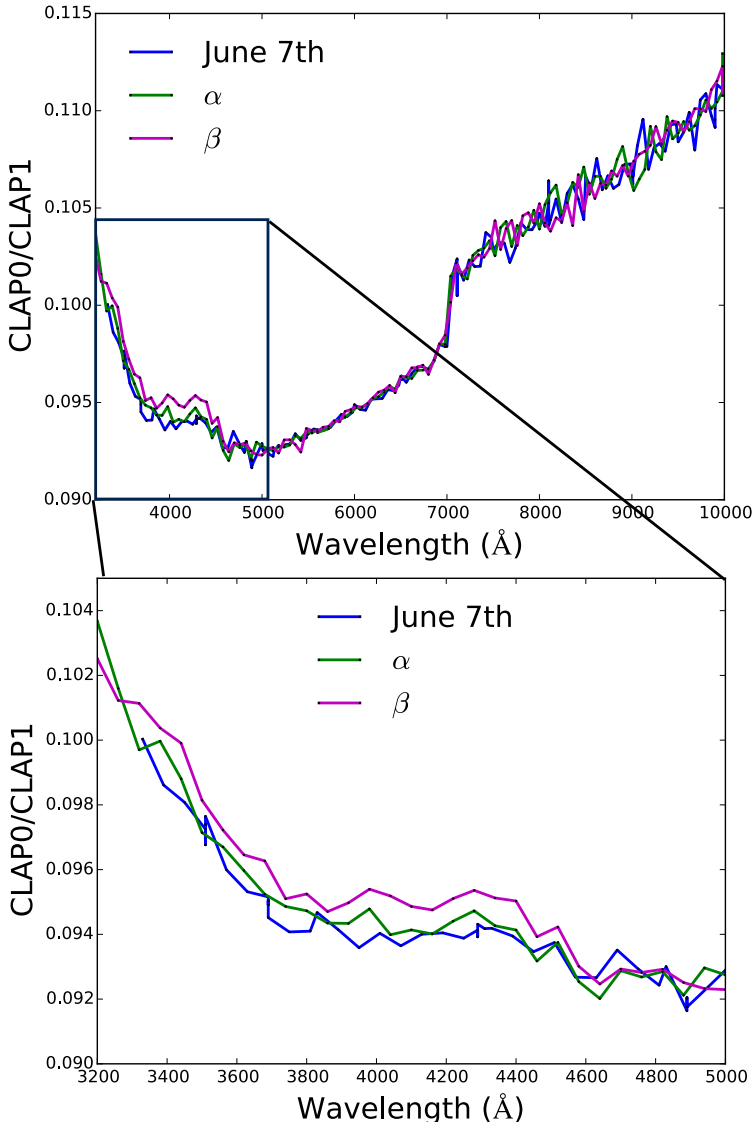

Fig. 10.6 Ratio between the CLAP0 and CLAP1 measurements (in ADU), for the different acquisitions in June 7th, α (June 8th) and β (June 11th) of the same two SCALA beams. The data are not scaled to compensate for the factor 10 due to the different internal gains of the two CLAPs. Top: the entire wavelength range scanned is shown. Bottom: a zoom in the range between 3300 and 5000 Å is shown. The statistical errors on these lines are similar to the errors shown in fig. 10.5 and are not plotted here for clarity. The June 7th (nighttime, blue) and α (first daytime, green) agree within statistical errors.

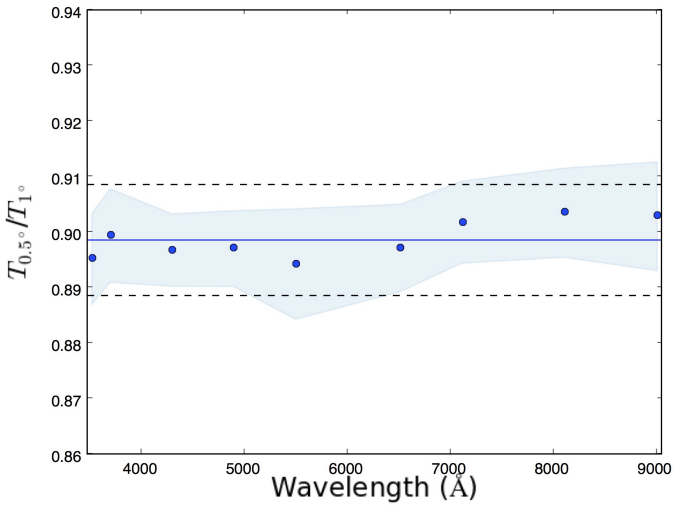

Fig. 10.7 The ratio between the quantity T_{λ_i} is shown for the same SCALA wavelengths observed with and without beam reducers. The mean amplitude is 0.899 with 0.003 standard deviation. The offset from 1 shows that some amount of scattered light exist, but the lack of a trend with wavelength (dashed lines show 1% offset from mean) shows this to be grey. The shadowed area around the circles is the standard deviation among all spaxels. From Lombardo et al., 2017 (in prep.)

We thus find no signs of significant wavelength dependent stray light at the 0.5° to 1° scale. We are currently planning future tests of stray light at even smaller scales. A complete comparison between observations with and without beam reducer and with and without mask on the primary mirror is shown in the Appendix A.2, where similar results are found again (gray offsets).

10.2.5 Exposure time error

In order to minimize the error on the SCALA exposure time we again use the CLAP data, integrating over the entire exposure using Simpson's method (see sec. 9.2.2). The sampling frequency (1kHz) allows us to sample up and down the ramp of the signal due to the shutter of the monochromator opening and closing (as shown in fig. 9.1).

We derive a conservative upper limit on the exposure time error by integrating only on the time with fully opened shutter. For each wavelength, we use only the exposure time computed from the number of data with fully opened shutter scaled with the sampling frequency, and we multiply it with the averaged light level. In this way, we also obtain an upper limit on the error due to the integration method. The two integration techniques show consistent results within <0.07%.

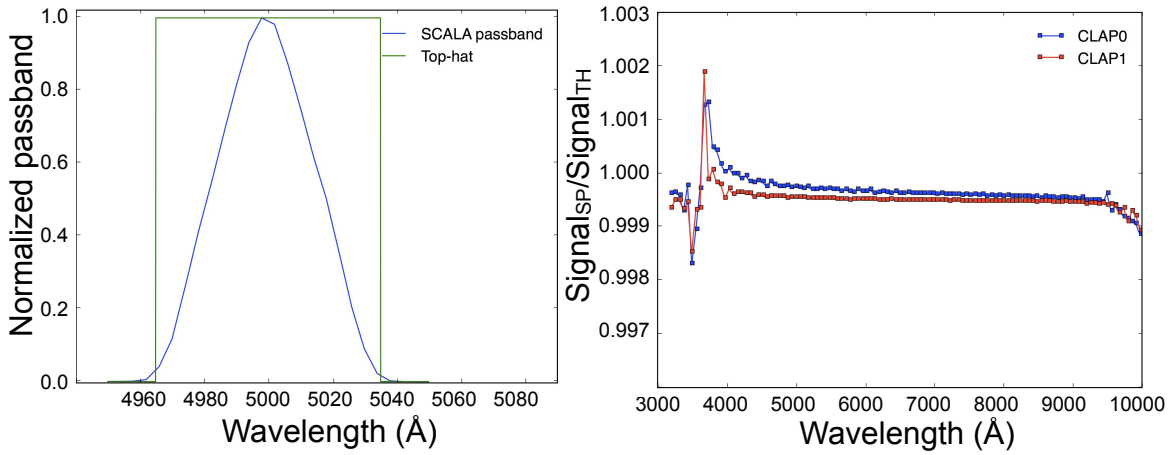

Fig. 10.8 Left: SCALA line profile (blue line) and a top-hat function centered at the line's peak wavelength (green line) are shown. Right: ratio between the CLAP measurements converted into fluxes using the SCALA profile ($\text{Signal}_{\text{SP}}$) and using a top-hat function ($\text{Signal}_{\text{TH}}$). The ratio for CLAP1 is in red and the ratio for CLAP0 is in blue.

10.2.6 SCALA line profile

Every time a photodiode observes a light source, the measured value is the light intensity integrated over the SED of the source and weighted by the wavelength dependent photodiode responsivity. One has to know these two quantities, SED of the source and photodiode responsivity, to find how much light is emitted by the source as function of wavelength. SCALA emits monochromatic light (35 Å FWHM bandpass), which makes the first requirement more relaxed, and the CLAPs are calibrated photodiodes, hence, we have their responses.

We now want to quantify how well we need to know the SCALA bandpass (or line profile), which is the factor $B^i_{\text{SCALA}}(\lambda)$ in eq. 7.3. As the CLAPs sensitivity curves are smoothly and almost linearly varying in the wavelength region of interest, the difference between using a realistic SCALA line profile (blue line in left hand side plot of fig. 10.8) and a top-hat filter (twice the previous FWHM, green line), centered at the central emission wavelength, is negligible. This is shown in the right hand side plot of fig. 10.8, which shows the ratio between the signal measured by CLAP (in blue CLAP0, in red CLAP1) and converted into flux units, one time using a top-hat function ($\text{Signal}_{\text{TH}}$) and the the second time using the SCALA bandpass profile ($\text{Signal}_{\text{SP}}$), to weight the response functions of the CLAPs. These ratios deviate less than 0.2% from 1, and represent conservative errors, as using a top-hat function as passband is an extreme case. From this we conclude that the precision requirements on the line profile estimate are well satisfied. We use the SCALA line profile to be closer to the effective passband shape.

We now have to verify that no systematic error is introduced by using the same line profile for each wavelength. The SCALA line profile from fig. 10.8 was measured in the lab

for each of the SCALA fiber bundle arms. As shown in Küsters 2014, a series of low pressure arc lamps (Ne, He and Xe) were used to illuminate the entrance slit of the monochromator, one at a time. The exit slit was then replaced by the SCALA fiber bundle and a photodiode was used to monitor the fiber bundle arms (one at a time). The output light was therefore given by the lamp spectrum convolved with the SCALA bandpass of the specific fiber bundle arm monitored. As the emission lines of the lamps were very narrow, their shapes were given only by the SCALA passband. The photodiode measured the SCALA passband by sampling these line profiles with a 4 Å step. The SCALA line shown in fig. 10.8 is an average over the many emission lines observed for one of the fiber bundle arms. SCALA fiber bundle arms have very similar line profiles. The main difference between them is that their peak emission wavelengths are slightly shifted, with maximum absolute shifts of 0.5 Å. Even if these shifts create issues when comparing the observed light from two different arms in a wavelength region where Xe emission lines are present (see sec. 6.4), they do not change the conclusions from fig. 10.8. We also verified that the shape and width of SCALA line profiles does not change with wavelengths. We can therefore apply these profiles to each wavelength observed by the CLAPs.

10.2.7 Interpolation of CLAPs responsivity

As mentioned in sec.7.4, we linearly interpolate the responsivity curves of the two CLAPs to obtain their calibration values in the wavelength ranges of usage. The curves provided by the DICE team have different sampling: 50 Å for CLAP0 and 100 Å for CLAP1.

To estimate the error due to this linear interpolation we compare the responsivity curves that a cubic spline interpolation produces. The total error (squared) on the CLAPs response curves is therefore computed by adding in quadrature the linear interpolation of the response curve errors (provided by the DICE team) and the difference between the linear and the cubic interpolation.

The square root of this error is shown in fig. 10.9 in blue for CLAP1 and green for CLAP0. The interpolation gives uncertainties smaller than 1% for the majority of wavelengths. They reach 1% in the wavelength regions where the response curves of the CLAPs are quickly changing (below 4000 Å and above 9990 Å). These uncertainties especially increase for CLAP1, whose response has a sparser sampling. For wavelengths bluer than 3500 Å the errors are dominated by the calibration errors rather than the interpolation, reaching the 1.2% level. As the total error is well below <0.4% for the wavelength range of interest, we do not need to improve the interpolation for the photodiode responses.

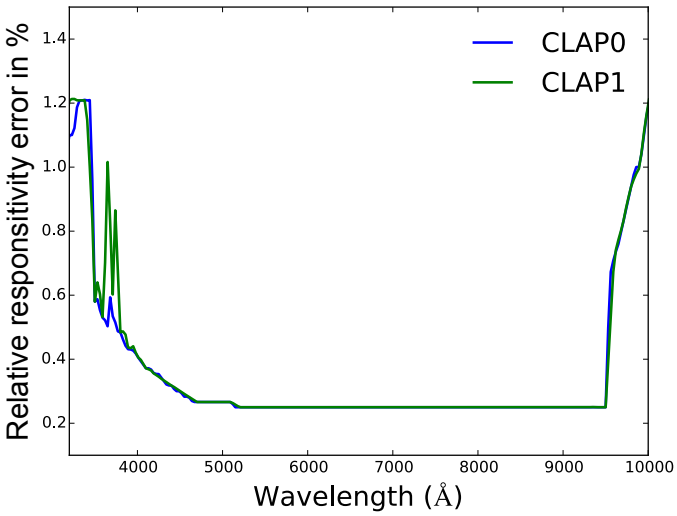

Fig. 10.9 The relative error, on a combination of the CLAPs responsivity uncertainties with that of the interpolation of the responsivity curves for the CLAPs, is shown in blue for CLAP1 and in green for CLAP0.

10.2.8 Optical cross talk within SCALA and SNIFS

There are two possible sources of optical cross talk for SCALA observations: the photodiode might receive scattered light from other beams, and in the SNIFS datacube part of the light belonging to one spaxel might be collected in another spaxel, and, because of the geometry of SNIFS optics, such light would be displayed in other wavelengths. In the second case the effect is negligible, since the light from another spaxel is <0.1% of the light integrated in the monochromatic line (Küsters et al., 2016).

The cross talk due to scattered light from another beam hitting the calibrated photodiode has been already described in sec. 7.4. The measurements have errors <0.05% (fig. 4 in Küsters et al., 2016). As this effect is mostly due to the reflection properties of the SCALA holding structure (black anodized aluminum), it can be assumed constant over time. The reference calibrated photodiode measurements in eq. 9.1, C_{1_λ}, have been corrected for this indirect illumination. In the SCALA relative efficiency measurements, eq. 8.1, the ratio between the two photodiode measurements highly suppresses the cross talk effect, since the different beams have similar contamination.

10.2.9 Scattered light within the monochromator

The monochromator out-of-bandpass light-leakage is 0.15% (manufacturer), which will be further reduced by the SNIFS background subtraction, yielding a final 0.05% contamination from an entire line. This is an estimate evaluated from the background level between SCALA lines in the SNIFS datacube. However, the photodiode integrates the entire spectrum observed

weighting it with its own responsivity. This is currently the limiting systematic uncertainty. We are currently performing narrow filter measurements to quantify this effect. If we confirm a 1% effect or more, a second monochromator, in series with the first, could be installed to effectively remove this contamination.

10.2.10 SCALA and SNIFS reproducibility

As mentioned in sec. 9.1, a set of wavelengths were repeated during each of the three SCALA sequences on June 7th. The system stability can be examined through computing the ratios between the throughput of the reobserved wavelengths, A/B and C/B. From 4000 to 9000 Å, the two ratios are consistent with each other and centered around 1.001 with standard deviation ± 0.003 (fig. 10.10). In the 3300-4000 Å region, the morning run (C) shows a 2% offset, which is added to the systematic uncertainty here. Thus, above 4000 Å we are not limited by reproducibility of our system.

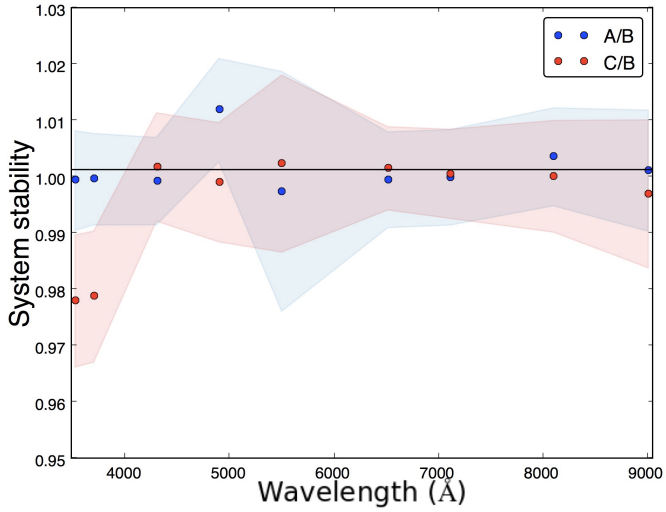

Fig. 10.10 Ratios of the throughput measured from the same SCALA lines observed during the three calibration sequences of June 7^{th}, 2015. The shaded blue region in the plot indicate the variations from spaxel to spaxel (standard deviation from the mean value). The black line is the average of the ratios from 4000 Å on, which is 1.001. From Lombardo et al., 2017 (in prep.)

10.3 Throughput comparison

After estimating the atmospheric extinction with the model by Buton et al. (2013), it is possible to compute the throughput using the flux calibration from the standard star observations. This is done by the SNIFS pipeline, whenever the atmospheric conditions are considered

photometric (so that time evolution of the atmospheric extinction during the same night can be neglected), as explained in sec. 5.2.2.

In this section we compare the calibration achieved through SCALA observations with the flux calibration from the standard stars observed during the same night, June 7^{th} 2015. In fig. 10.11 (top panel), the throughput of the "SNIFS+UH 88" system from these two calibration methodologies is shown. The two curves, blue circles from SCALA and black line from stars calibration, show a systematic difference resulting in what looks like a linear trend of $\sim$20%, comparing the bluest to the reddest wavelength (bottom panel of fig.10.11). In the bluest end we also find a larger scatter, as already noticed in fig.10.10. The offset around 6240 Å might partially be a consequence of the light scattered within the monochromator (as explained in sec. 10.2.9), as at that wavelength we introduce an order sorting filter. The overall effect, however, would be of just 1-2%, and even if it is larger than our precision requirements, it does not explain the linear trend observed.

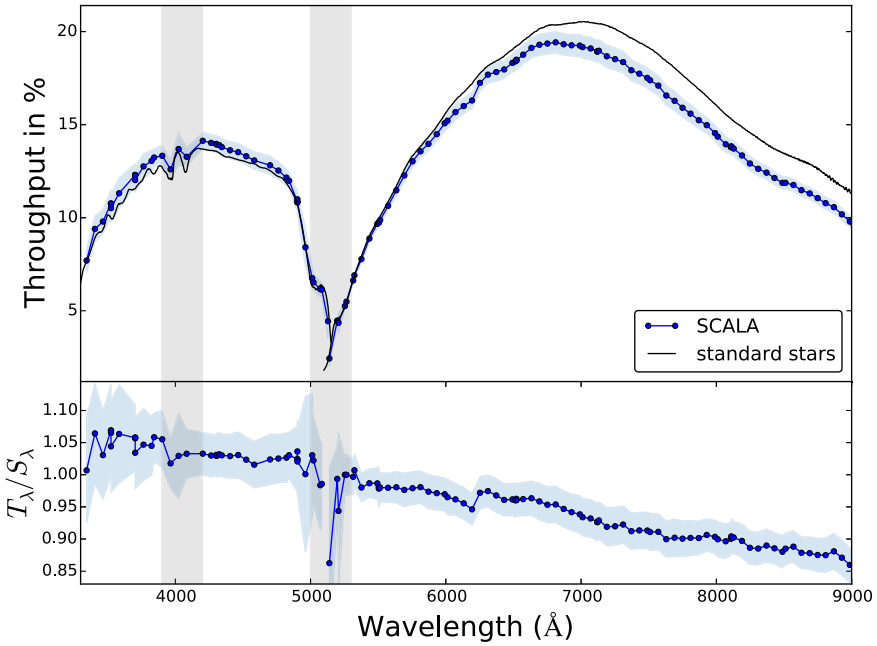

Fig. 10.11 Top: the throughput of the "SNIFS+UH 88" system is shown in % for the calibration from SCALA obsevations (T_λ as in fig.10.1), with blue circles, and from standard stars observations in the same night (S_λ), with a black full line. The measurements were performed on June 7^{th} with the primary mask applied. The black line is multiplied by 10 to scale it for the primary mirror surface covered by the mask. Bottom: ratio between the two calibration methodologies (as in the right hand side of eq. 9.3). The gray bands represent the regions affected by the dichroic features. The shaded blue bands in both panels in indicate the variations from spaxel to spaxel (standard deviation from the mean value).

As the decreasing linear trend appears to be too large to be due to a mis-calibration of SNIFS from the standard star observations, in the following sections, we describe a series of tests performed to uncover the origin of the discrepancy.

10.3.1 Investigating potential sources of the SNIFS/SCALA calibration trend

We performed several tests to understand the origin of the discrepancy found between the two flux calibration technique (from SCALA and standard star observations). In the following paragraphs a selection of these tests will be explained and shown in detail.

Flux calibrated SNIFS data

As consistency check, to ascertain that the linear trend is not caused by some conversion factor, e.g. from electrons to erg, or to some systematically off interpolation of the SNIFS pipeline calibration data, we also use the flux calibrated SNIFS datacubes of the SCALA calibration sequences, as described in sec. 9.2.1. From these datacubes we obtain a direct comparison of the "SNIFS+UH 88" system calibration performed through SCALA and standard star observations, as in eq. 9.2. We, thus, compare this result with the results shown in the bottom panel of fig. 10.11 (as in eq. 9.3). The two curves are shown in fig. 10.12 where we plot the measurements from flux calibrated data multiplied by 0.986 (computed just comparing the two curves), as a scaling factor might be present due to a non exact geometric factor estimation. Note that SCALA is not meant to provide an absolute flux calibration, but a relative calibration in wavelength, and hence a gray scaling factor is allowed. In the plot, the curves show the same decreasing linear trend. They match very well from 4200 Å, but disagree before that. The reason of this disagreement is under investigation. However, as the dichroic features are corrected for the flux calibrated data, we can expect some differences in those regions. These corrections might also affect regions nearby. We thus conclude that SNIFS data processed to full flux calibration produce similar SCALA comparisons as with the default mode of using the wavelength calibrated results. From now on the data from SNIFS will be only wavelength calibrated.

Extraction window for SNIFS data

We reduce SNIFS observations of SCALA following the standard SNIFS pipeline steps to be able to directly compare the calibration with the pipeline output. However, SCALA illuminates SNIFS in a different way than the calibration sources (continuum and arc lamps) or a star would. The pipeline steps, might therefore yield wrong results when applied to SCALA observations. For example one possibility is due to the extraction window used to

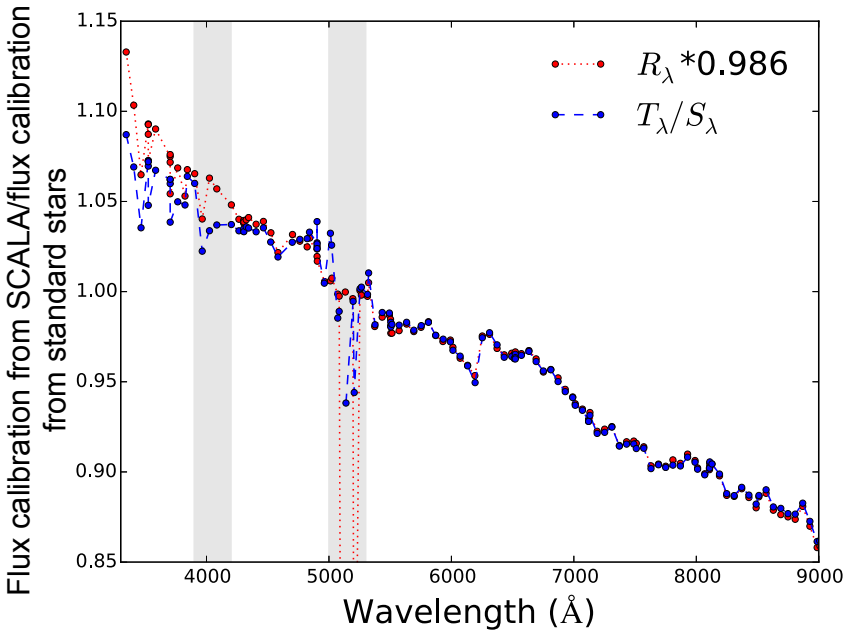

Fig. 10.12 Comparison between SCALA and traditional SNIFS flux calibration, evaluated first through comparing SNIFS throughput estimated by the pipeline and from SCALA observations, wavelength calibrated, (blue dashed line) and then if using the data as existing after the full SNIFS reduction pipeline (red dotted line). The measurements were performed on June 7^{th} with the primary mask applied. The red line is multiplied by 0.986. The gray bands represent the regions affected by the dichroic features.

group the pixels, in a CCD, belonging to the same spaxel in SNIFS images (i.e. to obtain datacubes from CCD images). This might be too small and cut some counts depending on wavelength. To better understand this point, we should consider this extraction window as a rectangle which has the long dimension in the direction of the dispersion. The spectrum, which is to be extracted and belongs to one spaxel, comes from the sum of the counts in the pixels in the orthogonal direction to the dispersion – cross-dispersion – hence the short side of the rectangle. If the pixels considered for extraction (in this direction) are not enough, then the observed flux in SNIFS would be systematically different from the flux estimated by the CLAPs, that do not have this issue.

Four SNIFS wavelength calibrated datacubes of SCALA observations, two for the red channel and two for the blue channel, were reduced (as described in sec.9.2.1) using different extraction windows width of 2, 4, 6, 8, 10, 12 and 14 pixels. Note that the default width for the SNIFS pipeline is of 5 pixels. For each SCALA line observed, one can plot the maximum emission value of the line averaged over the 225 spaxels, as a function of the extraction window (growth curve). There will be a residual background contribution to the number of

electrons measured that we can estimate with a linear fit on the larger extraction width data in the growth curve.

We can thus obtain an estimate of the true number of electrons belonging to a SCALA line, as shown in fig. 10.13 (chapter 5 of Howell, 2006, and references therein). The dashed line in the plot passes through the last two points of the plot, and the black solid line represents the estimated true number of electrons (the intercept of the dashed line). We compare this result with what we obtain from the default extraction width of 5 pixels (chosen to have a better S/N). By plotting this comparison against wavelength, we find the corrections to apply to the extracted default flux for each wavelength. The ratio between the true counts and the number extracted using a 5 pixel width is shown in fig. 10.14 where we find no significant trend for the blue channel of SNIFS and a falling trend, almost linearly, for the red channel.

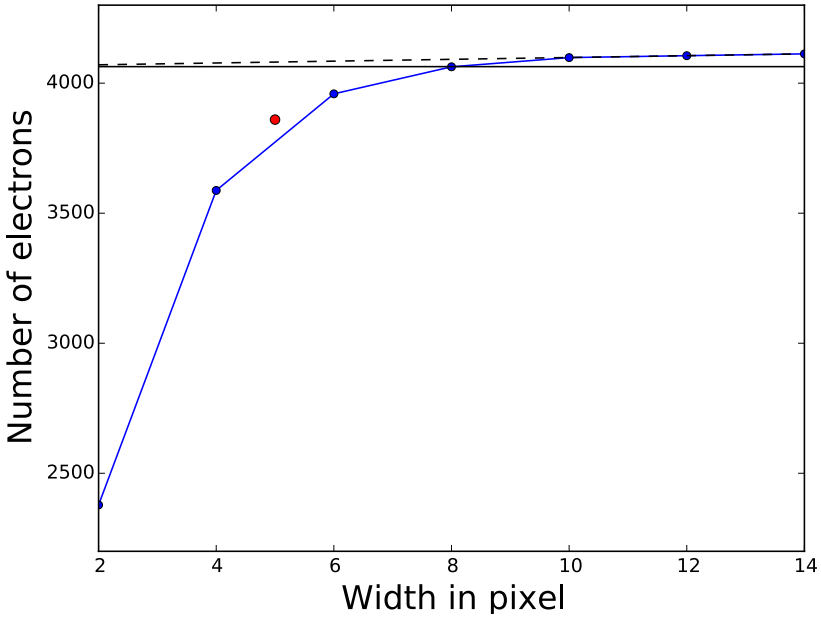

Fig. 10.13 Number of electrons in the maximum emission of a SCALA line (at 6431 Å) observed by SNIFS, as function of extraction width (blue circles). The peak values shown are averages of the peak values in every spaxels. The dashed black line indicates the line passing through the last two points and the black full line is the optimal number of electrons to extract. The red circle is the averaged peak value for the default extraction width. The errors are not visible in the plot as they are $\sim$0.1%.

The errors on the data shown in fig. 10.13 are $\sqrt{N_e/N_s}$ where N_e is the number of electrons and N_s the number of spaxels, as we are averaging over the 225 spaxels of SNIFS. These are not visible in the plot as they are $\sim 0.1\%$ level. By propagating them to the intercept computed, we produce the error bars in fig. 10.14.

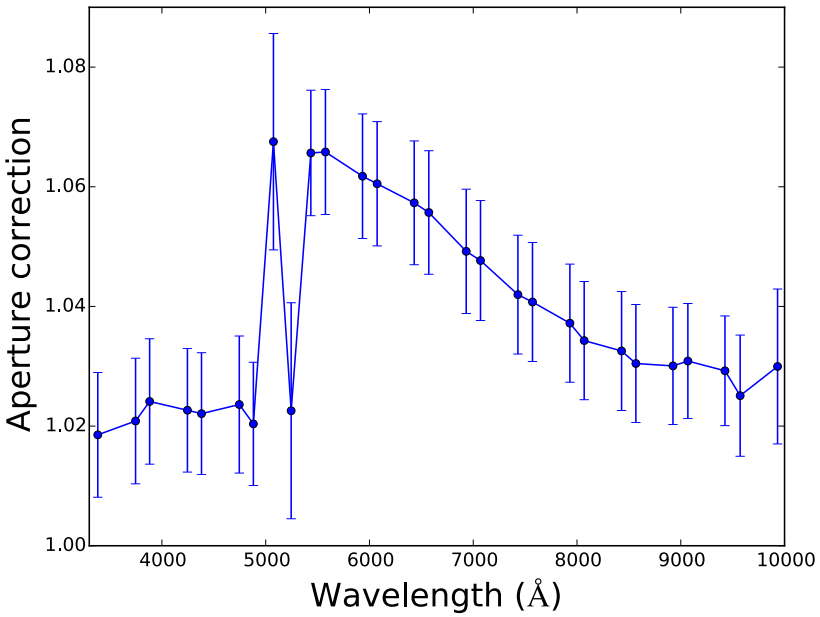

Fig. 10.14 The ratio between the optimal number of electrons extracted from SNIFS frames(as in fig. 10.13) and the values obtained for the default width is shown with the errors for each SCALA line observed in the four datacubes reduced.

The trend shown in fig. 10.14 agrees with the results for regular SNfactory observations as shown in fig. 3.9 of Copin (2013). That study predicts a faction of flux extracted by the default 5 pixels width of $\sim 96\%$ for all wavelengths in the blue channel and between 91% and 95% from 5546 to 9648 Å in the red channel. Additionally for an extraction width of 8 pixels Copin (2013) shows a faction of flux extracted of 0.99% for the blue channel (all wavelengths) and $\sim$0.98% for the red channel (all wavelengths), which is close to what we obtain. These quantities (for the 8 pixels width) agrees with the offsets from 1 shown in fig. 10.14 and the results with the 5 pixels width match the trend decreasing with wavelength observed by us in the red channel, and the gray behavior found in the blue channel. We conclude that there is no significant difference in the cross-dispersion line profile of a SCALA observation and of a star. We hence expect this effect to be accounted for in the instrumental calibration performed by the pipeline (S_λ) and canceled out in the ratio with the SCALA throughput (T_λ). Future tests could be made, e.g., using different width to extract the spectra of a calibration frame (such as a continuum exposure) and repeating the analysis again.

SCALA relative efficiency accuracy

Fig. 8.8 shows that, above 4700 Å, the SCALA relative efficiency has a trend growing, almost linearly, with wavelengths. For a rigorous analysis we want to test the assumptions that the

laboratory component-wise and the fully assembled in-situ measurements of the SCALA relative efficiencies (from sec. 8.4.1) are correct and that we are not dominated by some – yet unknown – systematic.

During the 2014 commissioning (sec. 8.3), we performed a series of SNIFS nighttime calibrations, illuminating only one module and closing all IS shutters of the other modules (as illustrated in fig. 8.6). As already mentioned, the elements dominating the color trend of the light emitted by the SCALA modules are the ISs (see fig. 6.18). If now we illuminate only one module at a time, where one of the CLAPs is mounted, we can disregard the SCALA relative efficiency and consider the three SCALA beams equals – in first approximation. It is therefore enough to consider the measurements from the CLAP illuminated, times three. In this case we do not need to correct for cross talk effects within SCALA (as in sec. 7.4).

As the measurements of module 1 (from fig. 8.61) are mostly compromised by monochromator shutter failures, we can use only the measurements from module 2 for this test. The ratio between these throughput measurements (night of June 8th) and the closest throughput from standard star observations (from July 24^{th}) is shown in fig. 10.15. Even without using the SCALA relative efficiency we still obtain the 30% decreasing linear trend as function of wavelengths. The SCALA relative efficiency is therefore not its cause.

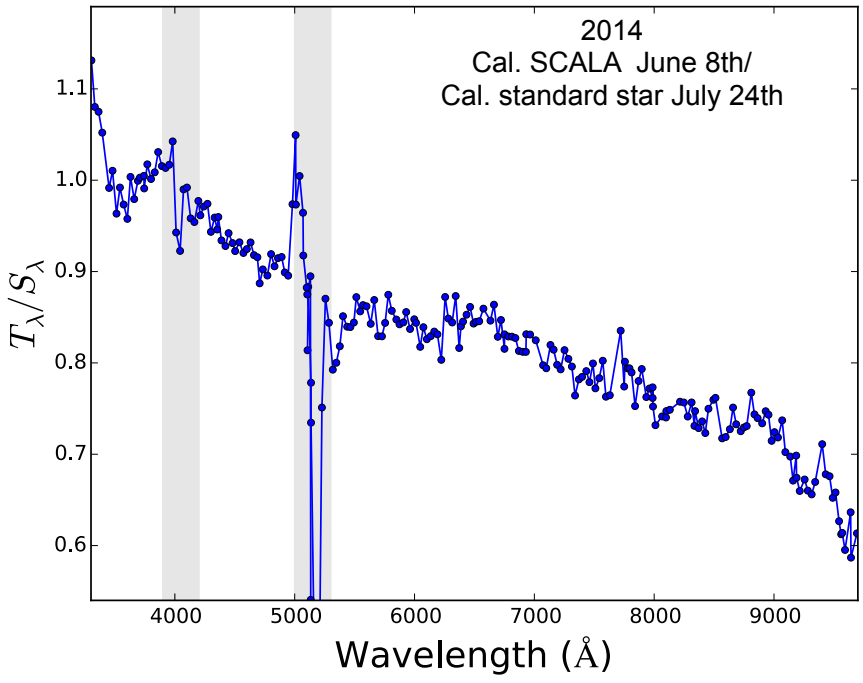

Fig. 10.15 Ratio between the calibration of the "SNIFS+UH 88" system from SCALA observations in June 8^{th}, 2014, and from standard star observation in July 24^{th}, same year. The SCALA measurements were performed illuminating only the module 2 from fig. 8.6. The gray bands represent the regions affected by the dichroic features.

Primary mirror mask effect on calibration from standard stars

During the 2015 nighttime observations, the standard stars were observed with the mask applied to the primary mirror of the telescope. As described, the mask covers 90% of the primary and the PSF, produced by this illumination, will be different from the usual. This difference might cause a systematic difference in how standard stars are extracted, as these algorithms were tested on stars observed using the full primary. Hence the flux calibration will result "wrong" correspondingly.

A straightforward way to verify if this is the case is to compare the throughput calculated with the mask with what is determined on a close-by night, without mask. In fig. 10.16 the ratios between the calibration from SCALA observations in June 7th and the standard star observations in June 7th (blue circles), May 25th (red circles and dotted line) and July 19th (magenta squares) are shown. The linear trend is present and even enhanced in all cases. We only show the results from May 25th and July 19th as they are the instrumental responses produced by the pipeline closest in time to June 7th. Note that these throughputs are produced only for photometric nights. Also, looking at the diagnostic plots of the residuals of the PSF extraction, generated by the pipeline, we don't find any significant hint of a "bad" extraction. From this we conclude that the PSF extraction code is able to handle the PSF produced by the presence of the mask and that this does not constitute the cause of the linear trend in fig. 10.11.

A better understanding of the mask effect on the PSF will be crucial for future studies, where the star spectra will be extracted for recalibration.

The discrepancy in the results of the calibration of the "SNIFS+UH 88" system with standard star observations and SCALA observations has not been solved yet and investigations are still continuing. These tests will include a calibration of the imaging channel, where a lack of a trend with wavelength would show that the difference arise internally in the SNIFS spectroscopic channels. In the next section we focus on the possible usage for SCALA.

10.4 Potential uses and possible applications

As already mentioned there are several possible additional applications for SCALA some of which are already in use for SNIFS:

1. Direct measurement of second-order contamination in the spectrograph.

2. Stray light study in the telescope optics, as briefly shown in the systematics section.

3. Individual SCALA wavelengenth exposures can be used to measure cross-talk between spaxels.

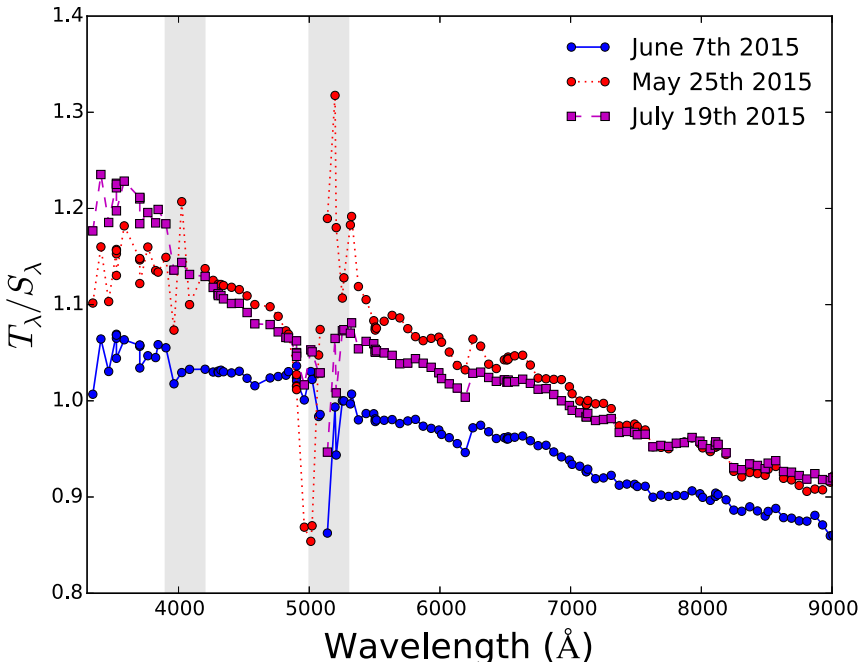

Fig. 10.16 The ratios between the two calibration methodologies from SCALA observations (in June 7^{th}) and standard star observations are shown. The standard star observations were performed with mask June 7^{th} (blue circles and full line) and without mask May 25^{th} (red circles and dotted line) and July 19^{th} (magenta squares and dashed line). The blue circles have been scales by 10 to make the curves comparable.The gray bands represent the regions affected by the dichroic features

4. UH 88+filter+CCD curves for the imaging channel filter set.

We have also tested throughput measurements with reduced exposure times, and during daytime. This would allow daily telescope throughput determinations.

10.4.1 Daytime usage of SCALA

We will in this section evaluate whether SCALA could be used to provide regular, daytime, throughput estimates. During 2015 we tested this possibility running a SCALA calibration with a wavelength sampling of 30 Å reducing the exposure time by a factor 3. This measurement set was performed during daytime, three days before the nighttime measurements of fig. 10.1, for about 4 hrs and the result is shown in fig. 10.17. Even though the statistical precision is lower than usual and there is some ambient light contamination, the overall result is still a smooth, high-precision measurement. Note that, as with the previous throughput curves, the shaded regions show the scatter between spaxels - not the throughput uncertainty.

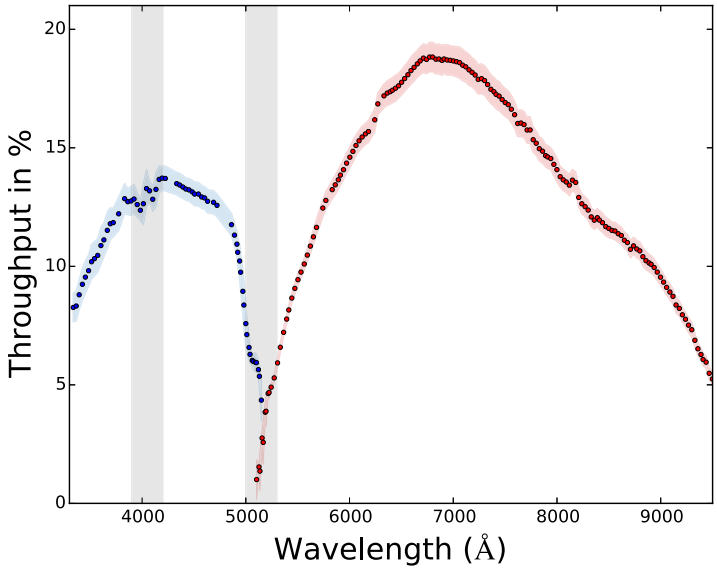

Fig. 10.17 Daytime measurements of the throughput $T_{\lambda_i,spx}$ averaged over the spaxels are shown in %. The blue and red circles represent the throughput measured by illuminating the spectrograph (blue and red channel respectively) and the telescope with SCALA during daytime on June 4^{th}, 2015. The colored bands indicate the throughput variation between SNIFS spaxels (the standard deviation), and are thus *not* an estimate of the throughput uncertainty. The gray bands represent the regions affected by the dichroic features. From Lombardo et al., 2017 (in prep.).

In fig. 10.18 we compare this June 4^{th} SCALA calibration with the SCALA nighttime calibration made on June 7^{th}, in red circles with dashed line (the primary mirror mask was applied for both cases). In the same figure we have included the ratio between the pipeline calibrations derived for these nights, in blue with full line. Both ratios have been scaled by their mean values computed in an interval between 5500 Å and 8000 Å, as we are just interested in their relative comparison as function of wavelength. The plot shows how well SCALA data follow the quickly changing transmissivity of SNIFS in wavelength, and match the one from the standard star flux calibration. A difference between the two is present in the wavelength region between 4500 and 5000 Å. This difference might be due to the variation of the dichroic mirror during these two days, as it could influence SNIFS transmissivity not only in the small wavelength regions in gray, but also in the range where the transmissivity is more steeply falling. These features are corrected in the SNIFS pipeline but not in the SCALA data used here. This difference might be enhanced as we interpolate the June 4th SCALA results (as more densely sampled) in order to build the ratio between the two SCALA measurements. More data from other days would be necessary to ascertain the origin of the difference (between pipiline and SCALA calibration of SNIFS) observed in the wavelength range 4500-5000 Å.

We find another difference between the two ratios above 9000 Å. This is most likely due to the presence of OH emission lines in the standard star spectra that are not removed by the nightly atmospheric extinction model. These features are partially removed by the sky background subtraction performed in the pipeline (step 6 in sec. 5.2.1). Their residuals will be imprinted in the instrumental response since the two quantities are fit together by the pipeline, as previously mentioned in sec. 5.2.2. The usage of an instrument like SCALA allows to calibrate the system at all wavelengths without being biased by external factors (e.g. the degeneracy of instrumental response and atmospheric extinction). An external calibration device might allow a better atmospheric extinction model and sky background subtraction, by providing an independent instrumental response.

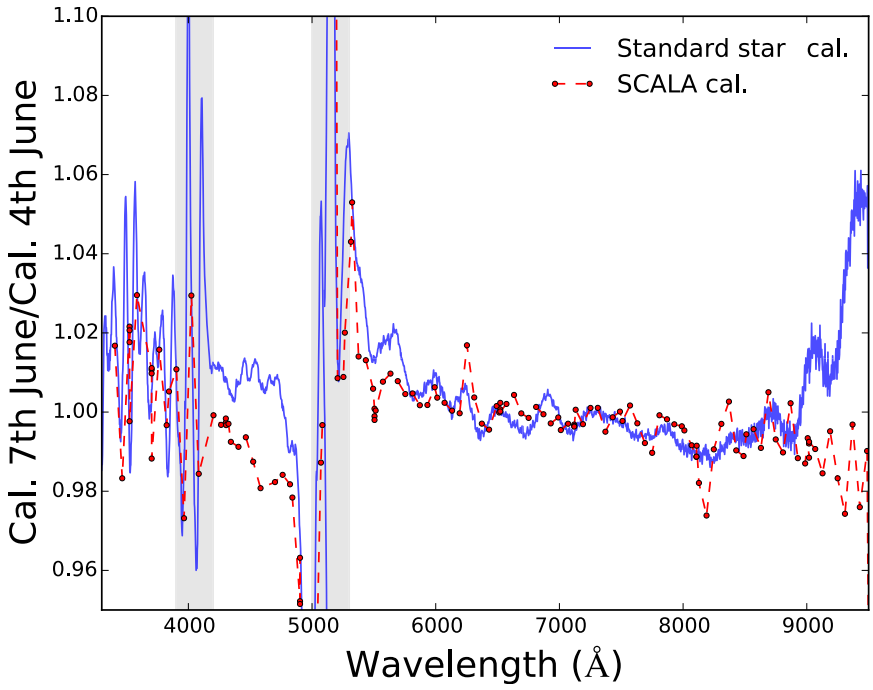

Fig. 10.18 The ratios between the throughput of the "SNIFS+UH 88" system measured on June 7^{th} and 4^{th}, 2015, are shown in red with dashed line for SCALA observations and blue full line from standard star observations. The SCALA and standard star measurements have been normalized with their averages of 0.969 and 0.931 respectively, computed in the wavelength range 5500-8000 Å. The gray bands represent the regions affected by the dichroic features.

From fig. 10.18 we conclude that daytime observations of SCALA can be used without compromising too much the overall precision of the calibration. SCALA can therefore be used also for fast estimation of throughput changes in case, e.g., of cleaning of the optics or filters replacements. Moreover, considering the large dimension of the calibration

beam produced in the focal plane of the telescope, such a device can be used also by other instruments mounted at the telescope having larger field of views than SNIFS.

Chapter 11

Summary and conclusions

The description and first results obtained with the SNIFS Calibration Apparatus, SCALA, were presented in this thesis. SCALA is built as part of a Nearby Supernova Factory effort to reach 1% color-calibration with the SuperNova Integral Field Spectrograph (SNIFS). It belongs to a global effort in astrophysics that in the past decades has tried to link the telescope+instrument calibration to laboratory flux standards. Such devices are necessary to improve the cosmological constraints from observations of SNe Ia, since systematic uncertainties on calibration are soon limiting factors when comparing SN Ia distances.

SCALA generates 18 beams, which are collimated at the 1° scale and illuminate the focal plane of the telescope uniformly. The SCALA light source system, lamp+monochromator, produces monochromatic light with a triangular line profile and a FWHM of 35 Å. The flux calibration of a NIST photodiode has been transferred to two photodiodes used as reference system (Cooled Large Area Photodiodes, CLAPs). SCALA is meant to transfer the NIST flux calibration to the UH 88+SNIFS system, and use this calibrated system to determine a NIST-traceable flux calibration of the standard star network. As SNIFS is an Integral Field Spectrograph, a SNIFS recalibrated standard star spectra could be used by any other astronomical observer.

Simulations and lab tests SCALA development had several testing and commissioning stages. After defining the overall design, simulations with a ray tracing software were performed. These simulations were used to improve the baffling system and to minimize, the already low, scattered light produced. Stray light is one of the limiting factors for the precision reached.

After the simulations the device was built and tested in the laboratory. All the color responses of the SCALA components (6 ISs, 6 fiber bundles and 18 mirrors) were characterized. These responses showed that the ISs, having relative color trends at the 6-8% level, dominate the overall color trend of the final SCALA beam.

Also the two CLAPs, the flux standards for SCALA, have been characterized. Their responsitivities were provided by the DICE team. We tested the evolution of the dark current which has to be subtracted for a precise light level measurement. We found that during nighttime, when the ambient light is not the dominant source of background variations, the dark current evolves smoothly. It shows a negligible variation when considered on the time scale of the longest, SCALA, exposure time, for which we have to subtract the dark current. By reading the CLAPs with the monochromator shutter closed before and after the light exposure (monochromator shutter opened) we can efficiently correct for the dark current.

SCALA characterization in-situ During commissioning we again measured the transmission of the SCALA beams, in the fully deployed set-up. We held the reference photodiode stationary, to always monitor the same SCALA beam, and we moved the other one sequentially to the 17 remaining beams. For each one of them we observed a series of monochromatic lines obtaining the relative response of the 17 beams with respect to the reference one, as function of wavelength. The normalized sum over these relative measurements provides the color of the SCALA light that illuminates SNIFS. Comparing this quantity with the independent component-wise measurements, we showed that we can reproduce the color trend of the total light generated by SCALA at a level better than 1%. By repeating the in-situ measurements after one year, we showed how the system evolves over time scales of years. It is therefore essential to repeat the 18 beams characterization before recalibrating the standard stars – the ultimate goal for SCALA.

Observational strategy, results and systematic errors The calibration strategy selected for SCALA allows us to perform a complete SNIFS+UH 88 calibration from 3300 Å to 10000 Å with steps of 30 Å in about 8 hrs and exposure times for each SCALA line between 30 s and 180 s. We use the monochromator's shutter to control SCALA illumination and we limit the maximum number of wavelengths observed per SNIFS exposure to 4 for the blue channel calibration (3300 - 5000 Å) and to 10 for the red one (5000 - 10000 Å).

In the 2015 commissioning, we mixed observations of standard stars with observations of SCALA, from which we calibrated the "SNIFS+UH 88" system with a sampling of 60 Å. During the same night we performed three SCALA calibration sequences (at twilight, middle of the night and after sunrise), and standard stars in the remaining available time slots. Combining these three SCALA observations, we produced a throughput curve of the "SNIFS+UH 88" system. Reobserving nine SCALA lines for each of these observations, we verified that the SCALA+SNIFS system is reproducible within 0.3% above 4000 Å and 2% below that. We also showed that we achieve a relative statistical uncertainty $< 0.6\%$ on these throughput measurements.

The main systematics currently measured are all $< 0.7\%$ in the wavelength range of interest (4000-9000 Å). We show, for example, that we can remove the ambient light contamination and the variations in the dark current from the photodiodes data by continuously monitoring the light from SCALA before the monochromator shutter opens and after it closes. SCALA can, therefore, be used for daytime throughput monitoring.

The stray light contribution due to the extended moon-like illumination provided by SCALA is found to be $< 0.4\%$ and mostly gray. The only limiting factor, to be verified, is the out-of-band-scattered-light within the monochromator, which could could lead to contamination larger than $1 - 2\%$. This scattered light would be observed by the reference photodiode and integrated over its range of sensitivity, while the spectrograph would disperse the light over its spectral range, yielding to a negligible contamination in SNIFS and a larger one in CLAP data.

Comparison of SCALA and standard star flux calibration of SNIFS Since we observed also standard stars in the 2015 commissioning, we were able to compare the flux calibration achieved through the standard pipeline of SNIFS, with the SCALA observations during the same night. The ratio between these two calibrations shows an overall color trend of $\sim$20% (from bluest to reddest wavelengths), decreasing towards redder wavelengths almost linearly. Many tests have been performed to ascertain the origin of the trend, but so far none of them gave indication of its cause. For example, we tested whether the presence of the primary mirror mask would cause a systematic difference in the estimated flux calibration through standard star observations. By using other pipeline throughput, from nights when the mask was not applied, we found the same trend again. We obtained the same trend also illuminating the "SNIFS+UH 88" system with only a single SCALA module (2014 commissioning test-data) and neglecting the SCALA relative efficiency term in the throughput.

The origin of this discrepancy in therefore still under investigation, and is the single missing step before a NIST-tracable calibration can be achieved.

Future steps and improvements There are several possibilities to improve the calibration results achieved. For example, one could use a more specific line profile to integrate the SCALA lines observed by SNIFS. These are currently integrated just using a Simpson method, but a line profile function might help to define more precisely the extended wings and pedestal of these lines. These corrections would improve the precision on the per mill scale.

Other checks are planned to put more stringent limits on some systematics, such as the scattered light form the monochromator and the optical stray light within SNIFS and the telescope. The former will be tested using narrow filters. We will hence compare the results

from SNIFS and CLAP observations with filters, inserted at the monochromator exit slit, and without. If this contamination is found to be above the 1% level, one could mount a second monochromator to suppress the effect. The stray light can be tested by unfocused observations of standard stars, such that the star would illuminate an area larger than the SNIFS field of view (closer to the SCALA illuminated area). By comparing the spectrum of the unfocused with the same focused star we could give limits on the impact of stray light.

The work so far has provided several lessons for a potential second generation SCALA project, SCALA 2.0. An improved calibration system should have as few optical components as possible, hence one would use only one light beam. In order to gain a better stray light control, this light source should be extremely collimated. For this purpose one could illuminate the focal plane of a small telescope with a light source – LEDs + monochromator+IS, or lamp+doublepass monochromator+IS – creating a parallel beam, called a projector beam, of the dimension of the primary mirror of this telescope. This projector beam should be monitored by a NIST-calibrated photodiode. By moving and rotating it in front of the primary of the telescope+instrument system to calibrate, one would calibrate the entire field of view observed.

References

S. Alam, F. D. Albareti, C. Allende Prieto, et al. The Eleventh and Twelfth Data Releases of the Sloan Digital Sky Survey: Final Data from SDSS-III. *ApJS*, 219:12, July 2015. doi: 10.1088/0067-0049/219/1/12.

J. Albert. Satellite-mounted Light Sources as Photometric Calibration Standards for Ground-based Telescopes. *AJ*, 143:8, January 2012. doi: 10.1088/0004-6256/143/1/8.

R. Amanullah, C. Lidman, D. Rubin, et al. Spectra and Hubble Space Telescope Light Curves of Six Type Ia Supernovae at 0.511 z 1.12 and the Union2 Compilation. *ApJ*, 716: 712–738, June 2010. doi: 10.1088/0004-637X/716/1/712.

P. Astier, J. Guy, N. Regnault, et al. The Supernova Legacy Survey: measurement of Ω_M, Ω and w from the first year data set. *A&A*, 447:31–48, February 2006. doi: 10.1051/0004-6361:20054185.

P. Astier, P. El Hage, J. Guy, et al. Photometry of supernovae in an image series: methods and application to the SuperNova Legacy Survey (SNLS). *A&A*, 557:A55, September 2013. doi: 10.1051/0004-6361/201321668.

M. Betoule, J. Marriner, N. Regnault, et al. Improved photometric calibration of the SNLS and the SDSS supernova surveys. *A&A*, 552:A124, April 2013. doi: 10.1051/0004-6361/201220610.

M. Betoule, R. Kessler, J. Guy, et al. Improved cosmological constraints from a joint analysis of the SDSS-II and SNLS supernova samples. *A&A*, 568:A22, August 2014. doi: 10.1051/0004-6361/201423413.

S. Blondin, L. Dessart, D. J. Hillier, and A. M. Khokhlov. One-dimensional delayed-detonation models of Type Ia supernovae: confrontation to observations at bolometric maximum. *MNRAS*, 429:2127–2142, March 2013. doi: 10.1093/mnras/sts484.

R. C. Bohlin. HST Stellar Standards with 1% Accuracy in Absolute Flux. In C. Sterken, editor, *The Future of Photometric, Spectrophotometric and Polarimetric Standardization*, volume 364 of *Astronomical Society of the Pacific Conference Series*, page 315, April 2007.

R. C. Bohlin. Hubble Space Telescope CALSPEC Flux Standards: Sirius (and Vega). *AJ*, 147:127, June 2014. doi: 10.1088/0004-6256/147/6/127.

R. C. Bohlin and R. L. Gilliland. Absolute Flux Distribution of the SDSS Standard BD +17deg4708. $AJ, 128 : 3053 - -3060, December 2004. doi : .$

R. C. Bohlin, K. D. Gordon, and P.-E. Tremblay. Techniques and Review of Absolute Flux Calibration from the Ultraviolet to the Mid-Infrared. *PASP*, 126:711–732, August 2014. 10.1086/677655.

C. Buton. *Étalonnage spectro-photométrique du SuperNova Integral Field Spectrograph dans le cadre du projet the Nearby Supernova Factory*. PhD thesis, Université Claude Bernard - Lyon I, Institut de Physique Nucléaire de Lyon., 2009.

C. Buton, Y. Copin, G. Aldering, et al. Atmospheric extinction properties above Mauna Kea from the Nearby SuperNova Factory spectro-photometric data set. *A&A*, 549:A8, January 2013. 10.1051/0004-6361/201219834.

M. Cappellari and E. Emsellem. Parametric Recovery of Line-of-Sight Velocity Distributions from Absorption-Line Spectra of Galaxies via Penalized Likelihood. *PASP*, 116:138–147, February 2004. 10.1086/381875.

J. A. Cardelli, G. C. Clayton, and J. S. Mathis. The relationship between infrared, optical, and ultraviolet extinction. *ApJ*, 345:245–256, October 1989. 10.1086/167900.

S. Chandrasekhar. The Maximum Mass of Ideal White Dwarfs. *ApJ*, 74:81, July 1931. 10.1086/143324.

M. Childress, G. Aldering, P. Antilogus, et al. Host Galaxy Properties and Hubble Residuals of Type Ia Supernovae from the Nearby Supernova Factory. *ApJ*, 770:108, June 2013. 10.1088/0004-637X/770/2/108.

M. Colless, B. A. Peterson, C. Jackson, et al. The 2dF Galaxy Redshift Survey: Final Data Release. *ArXiv Astrophysics e-prints*, June 2003.

A. Conley, J. Guy, M. Sullivan, et al. Light-curve parameters from the SNLS (Conley+, 2011). *VizieR Online Data Catalog*, 219:20001, February 2011.

Yannick Copin. *Spectro-photométrie à champ intégral dans le cadre du projet " The Nearby Supernova Factory "*. Accreditation to supervise research, Université Claude Bernard - Lyon I, June 2013. URL https://tel.archives-ouvertes.fr/tel-00855585.

S. Deustua, S. Kent, and J. A. Smith. *Absolute Calibration of Astronomical Flux Standards*, page 375. 2013. 10.1007/978-94-007-5618-2_8.

D. J. Eisenstein, H.-J. Seo, E. Sirko, and D. N. Spergel. Improving Cosmological Distance Measurements by Reconstruction of the Baryon Acoustic Peak. *ApJ*, 664:675–679, August 2007. 10.1086/518712.

H. K. Fakhouri, K. Boone, G. Aldering, et al. Improving Cosmological Distance Measurements Using Twin Type Ia Supernovae. *ApJ*, 815:58, December 2015. 10.1088/0004-637X/815/1/58.

A. V. Filippenko. The importance of atmospheric differential refraction in spectrophotometry. *PASP*, 94:715–721, August 1982. 10.1086/131052.

D. S. Finley, G. Basri, and S. Bowyer. The temperature scale of hot DA white dwarfs - Temperatures from far-ultraviolet continuum fluxes. *ApJ*, 359:483–498, August 1990. 10.1086/169080.

A. Friedmann. Über die Krümmung des Raumes. *Zeitschrift fur Physik*, 10:377–386, 1922. 10.1007/BF01332580.

J. A. Frieman, M. S. Turner, and D. Huterer. Dark Energy and the Accelerating Universe. *ARA&A*, 46:385–432, September 2008. 10.1146/annurev.astro.46.060407.145243.

J. Guy, P. Astier, S. Nobili, N. Regnault, and R. Pain. SALT: a spectral adaptive light curve template for type Ia supernovae. *A&A*, 443:781–791, December 2005. 10.1051/0004-6361:20053025.

J. Guy, P. Astier, S. Baumont, et al. SALT2: using distant supernovae to improve the use of type Ia supernovae as distance indicators. *A&A*, 466:11–21, April 2007. 10.1051/0004-6361:20066930.

M. Hamuy, M. M. Phillips, N. B. Suntzeff, et al. The Absolute Luminosities of the Calan/Tololo Type IA Supernovae. *AJ*, 112:2391, December 1996. 10.1086/118190.

D. S. Hayes. An Absolute Spectrophotometric Calibration of the Energy Distribution of Twelve Standard Stars. *ApJ*, 159:165, January 1970. 10.1086/150299.

D. S. Hayes and D. W. Latham. A rediscussion of the atmospheric extinction and the absolute spectral-energy distribution of VEGA. *ApJ*, 197:593–601, May 1975. 10.1086/153548.

M. Hicken, W. M. Wood-Vasey, S. Blondin, et al. Improved Dark Energy Constraints from ˜100 New CfA Supernova Type Ia Light Curves. *ApJ*, 700:1097–1140, August 2009. 10.1088/0004-637X/700/2/1097.

W. Hillebrandt and J. C. Niemeyer. Type IA Supernova Explosion Models. *ARA&A*, 38: 191–230, 2000. 10.1146/annurev.astro.38.1.191.

J. B. Holberg, J. Basile, and F. Wesemael. DA white dwarf effective temperatures determined from IUE Lyman-alpha profiles. *ApJ*, 306:629–641, July 1986. 10.1086/164372.

S. B. Howell. *Handbook of CCD Astronomy*. March 2006.

J. Janesick and M. Blouke. Sky on a Chip: The Fabulous CCD. *S&T*, 74, September 1987.

S. Jha, A. G. Riess, and R. P. Kirshner. Improved Distances to Type Ia Supernovae with Multicolor Light-Curve Shapes: MLCS2k2. *ApJ*, 659:122–148, April 2007. 10.1086/512054.

M. E. Kaiser and Access Team. ACCESS: Design, Calibration Strategy, and Status. In S. Deustua, S. Allam, D. Tucker, and J. A. Smith, editors, *The Science of Calibration*, volume 503 of *Astronomical Society of the Pacific Conference Series*, page 221, May 2016.

M. E. Kaiser, J. W. Kruk, S. R. McCandliss, et al. ACCESS: absolute color calibration experiment for standard stars. In *Ground-based and Airborne Instrumentation for Astronomy II*, volume 7014 of , page 70145Y, July 2008. 10.1117/12.790106.

P. L. Kelly, M. Hicken, D. L. Burke, K. S. Mandel, and R. P. Kirshner. Hubble Residuals of Nearby Type Ia Supernovae are Correlated with Host Galaxy Masses. *ApJ*, 715:743–756, June 2010. 10.1088/0004-637X/715/2/743.

A. Kim, A. Goobar, and S. Perlmutter. A Generalized K Correction for Type IA Supernovae: Comparing R-band Photometry beyond z=0.2 with B, V, and R-band Nearby Photometry. *PASP*, 108:190, February 1996. 10.1086/133709.

D. Küsters, S. Lombardo, M. Kowalski, et al. Calibrating the SNfactory Integral Field Spectrograph (SNIFS) with SCALA . In *Ground-based and Airborne Instrumentation for Astronomy VI*, volume 99084 of , 2016. 10.1117/12.2232902.

D. Küsters 2014. "development of a calibration unit for the supernova integral field spectrograph (snifs)". Master Thesis.

B. Lantz, G. Aldering, P. Antilogus, et al. SNIFS: a wideband integral field spectrograph with microlens arrays. In L. Mazuray, P. J. Rogers, and R. Wartmann, editors, *Optical Design and Engineering*, volume 5249 of *Society of Photo-Optical Instrumentation Engineers (SPIE) Conference Series*, pages 146–155, February 2004. 10.1117/12.512493.

T. C. Larason and J. M. Houston. Spectroradiometric Detector Measurements: Ultraviolet, Visible, and Near-Infrared Detectors for Spectral Power. Technical report, National Institute of Standards and Technology, NIST Special Publication 250-41, 2008.

G. Lemaître. Un Univers homogène de masse constante et de rayon croissant rendant compte de la vitesse radiale des nébuleuses extra-galactiques. *Annales de la Société Scientifique de Bruxelles*, 47:49–59, 1927.

E. V. Linder. Importance of supernovae at z0.1 for probing dark energy. *PhRvD*, 74(10): 103518, November 2006. 10.1103/PhysRevD.74.103518.

S. Lombardo, G. Aldering, A. Hoffmann, et al. A flux calibration device for the SuperNova Integral Field Spectrograph (SNIFS). In *Ground-based and Airborne Instrumentation for Astronomy V*, volume 9147 of , page 91474R, July 2014. 10.1117/12.2055066.

J. L. Marshall, J.-P. Rheault, D. L. DePoy, et al. DECal: A Spectrophotometric Calibration System For DECam. *ArXiv e-prints*, February 2013.

J. C. Mather, E. S. Cheng, D. A. Cottingham, et al. Measurement of the cosmic microwave background spectrum by the COBE FIRAS instrument. *ApJ*, 420:439–444, January 1994. 10.1086/173574.

J. B. Oke and R. E. Schild. The Absolute Spectral Energy Distribution of Alpha Lyrae. *ApJ*, 161:1015, September 1970. 10.1086/150603.

Y.-C. Pan, M. Sullivan, K. Maguire, et al. The host galaxies of Type Ia supernovae discovered by the Palomar Transient Factory. *MNRAS*, 438:1391–1416, February 2014. 10.1093/mnras/stt2287.

A. A. Penzias and R. W. Wilson. A Measurement of Excess Antenna Temperature at 4080 Mc/s. *ApJ*, 142:419–421, July 1965. 10.1086/148307.

R. Pereira, R. C. Thomas, G. Aldering, et al. Spectrophotometric time series of SN 2011fe from the Nearby Supernova Factory. *A&A*, 554:A27, June 2013. 10.1051/0004-6361/201221008.

S. Perlmutter. Supernovae, Dark Energy, and the Accelerating Universe. *Physics Today*, 56 (4):53–62, April 2003. 10.1063/1.1580050.

S. Perlmutter, G. Aldering, G. Goldhaber, et al. Measurements of Ω and Λ from 42 High-Redshift Supernovae. *ApJ*, 517:565–586, June 1999.

M. M. Phillips. The absolute magnitudes of Type IA supernovae. *ApJl*, 413:L105–L108, August 1993. 10.1086/186970.

Planck Collaboration, R. Adam, P. A. R. Ade, et al. Planck 2015 results. IX. Diffuse component separation: CMB maps. *A&A*, 594:A9, August 2016. 10.1051/0004-6361/201525936.

T. Rauch, K. Werner, R. Bohlin, and J. W. Kruk. The virtual observatory service TheoSSA: Establishing a database of synthetic stellar flux standards. I. NLTE spectral analysis of the DA-type white dwarf G191-B2B. *A&A*, 560:A106, December 2013. 10.1051/0004-6361/201322336.

N. Regnault, A. Guyonnet, K. Schahmanèche, et al. The DICE calibration project Design, characterization, and first results. *A&A*, 581:A45, September 2015. 10.1051/0004-6361/201424471.

A. G. Riess, W. H. Press, and R. P. Kirshner. A Precise Distance Indicator: Type IA Supernova Multicolor Light-Curve Shapes. *ApJ*, 473:88, December 1996. 10.1086/178129.

A. G. Riess, A. V. Filippenko, P. Challis, et al. Observational Evidence from Supernovae for an Accelerating Universe and a Cosmological Constant. *AJ*, 116:1009–1038, September 1998.

M. Rigault, Y. Copin, G. Aldering, et al. Evidence of environmental dependencies of Type Ia supernovae from the Nearby Supernova Factory indicated by local Hα. *A&A*, 560:A66, December 2013. 10.1051/0004-6361/201322104.

M. Rigault, G. Aldering, M. Kowalski, et al. Confirmation of a Star Formation Bias in Type Ia Supernova Distances and its Effect on the Measurement of the Hubble Constant. *ApJ*, 802: 20, March 2015. 10.1088/0004-637X/802/1/20.

H. P. Robertson. On the Foundations of Relativistic Cosmology. *Proceedings of the National Academy of Science*, 15:822–829, November 1929. 10.1073/pnas.15.11.822.

S. E. Rugh and H. Zinkernagel. The Quantum Vacuum and the Cosmological Constant Problem. *ArXiv High Energy Physics - Theory e-prints*, December 2000.

C. Saunders, G. Aldering, P. Antilogus, et al. Type Ia Supernova Distance Modulus Bias and Dispersion from K-correction Errors: A Direct Measurement Using Light Curve Fits to Observed Spectral Time Series. *ApJ*, 800:57, February 2015. 10.1088/0004-637X/800/1/57.

C. W. Stubbs and J. L. Tonry. Toward 1% Photometry: End-to-End Calibration of Astronomical Telescopes and Detectors. *ApJ*, 646:1436–1444, August 2006. 10.1086/505138.

C. W. Stubbs, S. K. Slater, Y. J. Brown, et al. Preliminary Results from Detector-Based Throughput Calibration of the CTIO Mosaic Imager and Blanco Telescope Using a Tunable Laser. In C. Sterken, editor, *The Future of Photometric, Spectrophotometric and Polarimetric Standardization*, volume 364 of *Astronomical Society of the Pacific Conference Series*, page 373, April 2007.

C. W. Stubbs, P. Doherty, C. Cramer, et al. Precise Throughput Determination of the PanSTARRS Telescope and the Gigapixel Imager Using a Calibrated Silicon Photodiode and a Tunable Laser: Initial Results. *ApJS*, 191:376–388, December 2010. 10.1088/0067-0049/191/2/376.

M. Sullivan, A. Conley, D. A. Howell, et al. The dependence of Type Ia Supernovae luminosities on their host galaxies. *MNRAS*, 406:782–802, August 2010. 10.1111/j.1365-2966.2010.16731.x.

R. Tripp. A two-parameter luminosity correction for Type IA supernovae. *A&A*, 331: 815–820, March 1998.

M. Turatto. Classification of Supernovae. In K. Weiler, editor, *Supernovae and Gamma-Ray Bursters*, volume 598 of *Lecture Notes in Physics, Berlin Springer Verlag*, pages 21–36, 2003. 10.1007/3-540-45863-8_3.

A. G. Walker. Distance in an expanding universe. *MNRAS*, 94:159, December 1933. 10.1093/mnras/94.2.159.

Appendix A

A.1 Reproducibility of lab measurements for SCALA ISs

During the laboratory measurements performed in 2014 as described in sec. 6.4.3, we repeated the measurement of the response of IS4 three times (a, b and c). These measurements were made in different days and in mixed orders with all the other ISs. We show in fig. A.1 the ratios of two of the IS4 measurements with the third one.

These ratios show an offset with no wavelength dependencies, as expected. The position of the output port of the IS with respect to the signal photodiode might differ of some tens of mm making the flux collected by the photodiode slightly different in absolute value, but not in color. This is also the reason why we usually normalize these results (we are only interested in the relative response of SCALA components).

A.2 Stray light tests

As explained in sec. 10.2.4 we performed several tests to study the stray light produced inside the telescope and SNIFS by SCALA illumination. We repeated the same set of SCALA lines observations with SNIFS in the following configurations: beam reducer+mask (beams of 0.5° and 16 cm diameter), mask only (beams of 1° and 16 cm diameter), beam reducer and no mask (beams of 0.5° and 20 cm diameter) and finally no mask and no beam reducer (beams of 1° and 20 cm diameter). The ratio between the case with mask+beam reducer and mask without beam reducer is already shown in fig. 10.7 and plotted again in fig. A.2 for completeness among the other possible combinations. From the plot in fig. A.2 we do not see any significant wavelength dependency for all the cases shown. We conclude that the lowest amount of stray light are for the cases with beam reducer and primary mask applied.

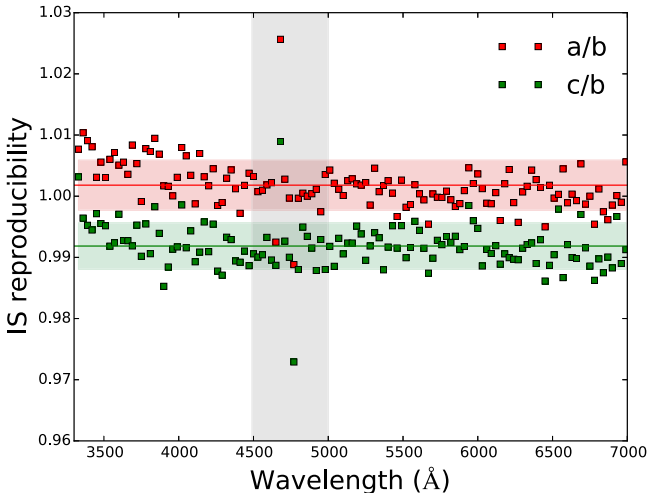

Fig. A.1 Ratios of the relative responses of SCALA IS4 a, c with respect to the third one, b. The gray band delimits the region where the weak emission lines of the Xe lamp are located (4500-5000 Å). The full lines are the averages of these ratios and the colored bands are the standard deviations ($a/b = 1.002 \pm 0.004$, $c/b = 0.992 \pm 0.004$).

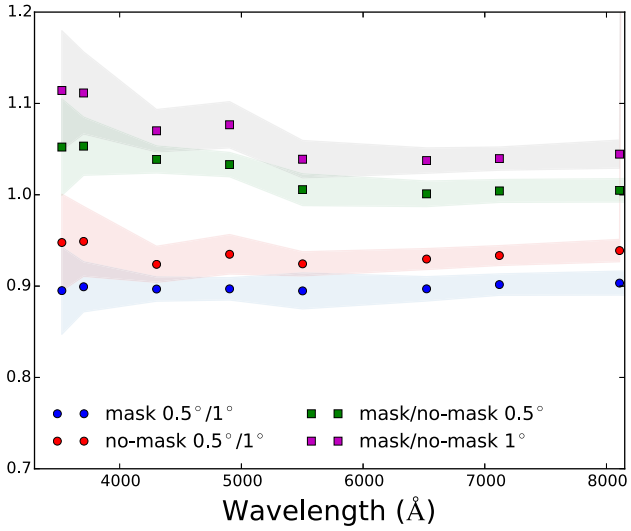

Fig. A.2 The ratio between the quantity T_{λ_i} is shown for the same SCALA wavelengths observed with and without beam reducers (in blue with mask and red without mask), with and without mask (for the case with beam reducer in green and without beam reducer in magenta). The shadowed areas around the squares are the standard deviations among all spaxels.

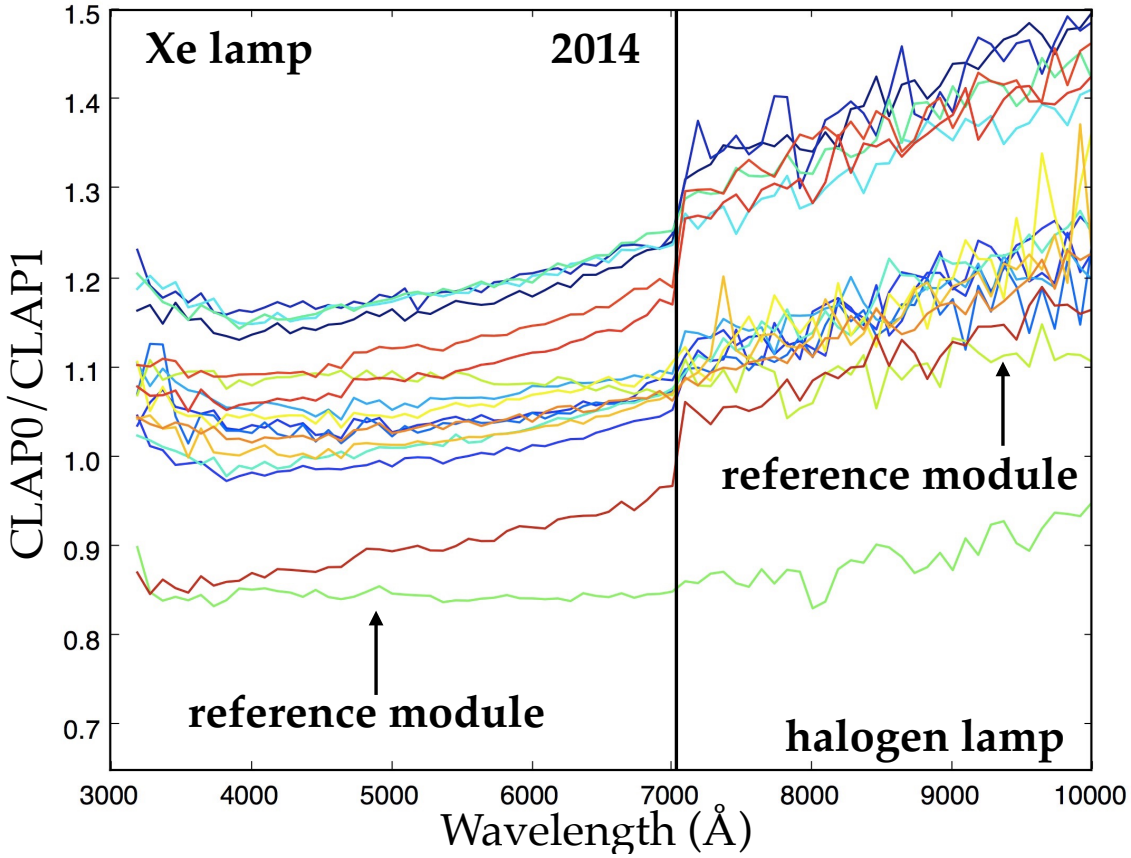

Fig. A.3 Single SCALA beam in-situ measurements, for the SCALA relative efficiency performed in 2014, are shown with different colors for each beam. The black line in the middle distinguish the wavelength range for which we used the Xe lamp and the halogen lamp. The CLAPs measurements are in W. The responses that corresponds to the beams belonging to the same module as the reference beam (measured by CLAP1) are pointed by black arrows and are in acid green and yellow sand.

A.3 SCALA relative efficiency accuracy

In fig. A.3 and A.4 are shown the single SCALA beam in-situ measurements for the SCALA relative efficiency performed in 2014 and 2015 respectively and discussed in sec. 8.4.1. We can see how the responses of the two beams from the same projector module of the reference beam (in acid green and yellow sand) are mostly gray (no trend as function of wavelength) with respect to the other beams in both figures. Comparing the figures from 2014 and 2015 we can additionally see that the bluest ends of each curve of the other projector modules are steeper in the 2015 than in the 2014 in-situ measurements, and in the 2015 a more pronounced "bump " appears between 3700 and 4700 Å. These differences between the two SCALA relative efficiency measurements are causing the color trend shown in the bottom of fig. 8.8.

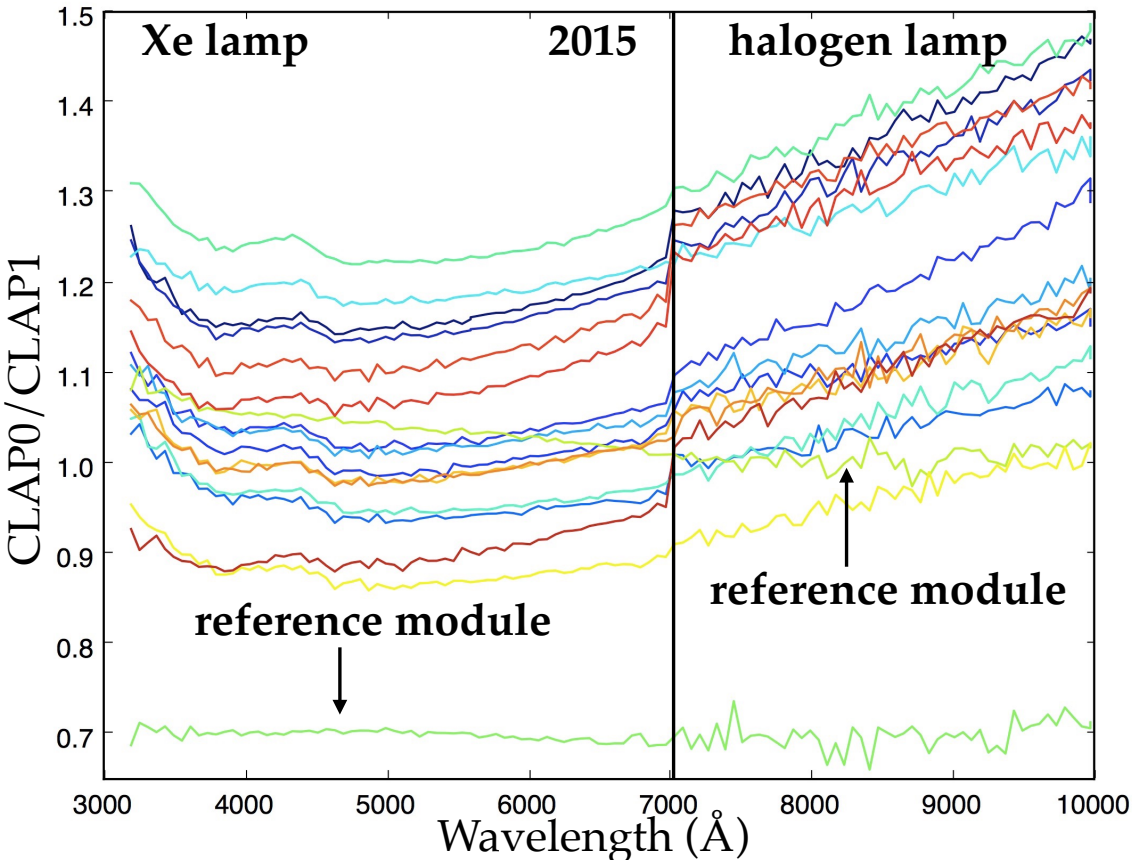

Fig. A.4 Single SCALA beam in-situ measurements, for the SCALA relative efficiency performed in 2015, are shown with different colors for each beam. The black line in the middle distinguish the wavelength range for which we used the Xe lamp and the halogen lamp. The CLAPs measurements are in W. The responses that corresponds to the beams belonging to the same module as the reference beam (measured by CLAP1) are pointed by black arrows and are in acid green and yellow sand. The curve in acid green is the same as the black curve in fig. 8.8.

A.4 Statistical error propagation

For this thesis work, all errors shown are statistical errors computed with standard error propagation:

$$\sigma_y^2 = \sum_i \left(\frac{\partial y}{\partial x_i} \sigma_{x_i} \right)^2, \tag{A.1}$$

where σ_y^2 is the variance on the function that depends on i variables (x_i) under the assumption that these variables are uncorrelated.

In the case of fig. 8.7, the errors on the laboratory measurements where propagated starting from the single components responses, computed from averaged measurements over 10 acquisitions.

For the two commissioning curves in fig. 8.7 and 8.8 the error is propagated according to eq. A.1 through each of the data reduction steps performed: removal of background level, cosmic rays and optical cross talk, averages of light-only exposures and conversion from ADU to W. For example, the background removal is performed (for each wavelength) by subtracting the result of a linear regression on the background exposure data only. From these data we compute the slope of the line passing through them ($y = x \cdot a_1 + a_2$) as $a_1 = \mathrm{Cov}[X,Y]/\mathrm{Var}[X]$ where X is the sampling in time and Y are the counts level registered. In this case the variance on slope and intercept are:

$$\sigma_{a_1}^2 = \frac{N\sigma_Y^2}{\left(N\sum_i X_i^2\right) - \left(\sum_i X_i\right)^2}; \quad \sigma_{a_2}^2 = \sigma_{a_1}^2 \cdot \frac{\sum_i X_i^2}{N}, \tag{A.2}$$

where N is the number of data belonging to the background exposures and $\sigma_Y^2 = \sum_i Y_i'^2 / (N-2)$, with $Y' = Y - y$.

If now we translate our reference system so that $X \to X'$ and its average is zero ($\bar{X}' = 0$), we have $\mathrm{Cov}(a_1, a_2') = 0$. Therefore, after subtracting the line described by a_1 and $a_2' = \bar{Y}$ to the data (the two background exposures and the light exposure), $Y' = Y - y$, we can compute the variance on each data point as:

$$\sigma_{Y_i'}^2 = \sigma_{a_1}^2 X'^2 + \sigma_{\bar{X}}^2 a_1^2 + \sigma_{\bar{Y}}^2, \tag{A.3}$$

where $\sigma_{\bar{X}}^2$ is the variance on the mean of X, $\sigma_{\bar{Y}}^2$ is the variance on the mean of Y and $\sigma_{a_1}^2$ is the same as before. We then use eq. A.1 to obtain the error on the mean of the pure light exposure data, used in this section (we take the square root of the sum over all the variances of the pure light data divided for the squared number of data used).

A.5 Composite Simpson's rule

The composite Simpson's rule to integrate is:

$$\int_a^b f(x)dx \approx \frac{h}{3}\left[f(x_0)+2\sum_{j=1}^{n/2-1} f(x_{2j})+4\sum_{j=1}^{n/2} f(x_{2j-1})+f(x_n)\right], \tag{A.4}$$

where n is the number of data, $h=(b-a)/n$, $x_0=a$ and $x_n=b$.

Appendix B

B.1 Reducing astrophysical uncertainties on SN Ia cosmology

Using the SNfactory dataset, we recently demonstrated a correlation between the SN standardized brightness and the intensity of local host star formation activity (Rigault et al., 2013, 2015). This seems to explain the well known –yet not understood– SN dependency with the global host stellar mass. The next step to fully understand the origin of these effects is to access the SN progenitor properties themselves.

With that goal, I have developed a statistical analysis based on the spectral energy distribution (SED) fit of the several hundreds local host spectra of SNfactory. Fig.B.1. exemplifies such a SED fit – using the ppxf code by Cappellari and Emsellem (2004), as in Pan et al. (2014) – and the derived local star formation history. This enables me to build the first delay time distribution (DTD) based on stellar information in the SN vicinity. In comparison to the usual global measurements this allows to mitigate the influence of the potentially strong gradients of galaxy stellar population properties. The goal of my analysis is to deliver a more accurate SN progenitor DTD. With fits to data complete, I am currently estimating uncertainties through simulated/perturbed spectra.

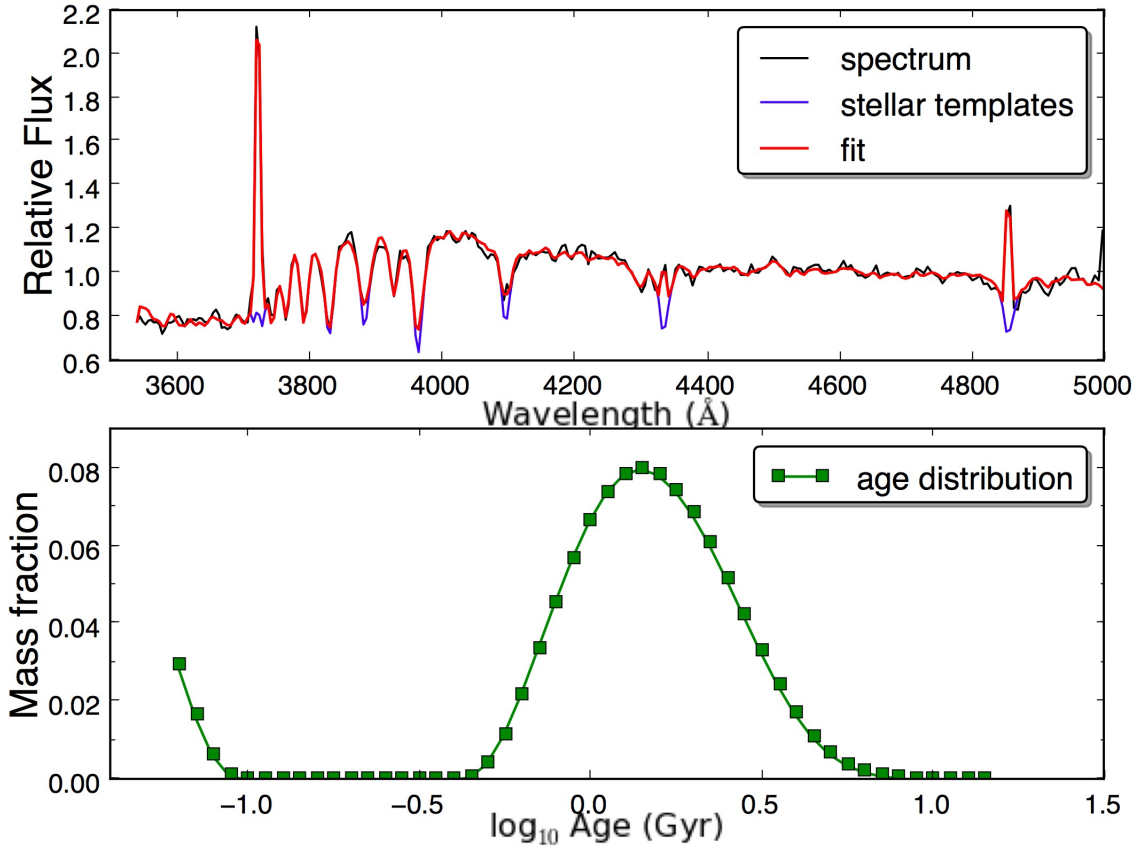

Fig. B.1 Top: example of fit of an SNfactory host galaxy (PTF10qjq) spectrum: in black the galaxy spectrum, in blue the stellar templates and in red the best fit. Bottom: Age distribution obtained from the fit shown on the top. A consistent fraction of the mass is located in very young star populations (age $<$200Myr).

List of figures

List of tables

List of Abbreviations

2dFGRS Two-degree-Field Galaxy Redshift Survey (http://2dfgrs.net).
ACCESS Absolute Color Calibration Experiment for Standard Stars.
ADR Atmospheric Differential Refraction.
BAO Baryon Acoustic Oscillations.
C-O WD carbon-oxygen white dwarf.
CMB Cosmic Microwave Background.
DES Dark Energy Survey (https://www.darkenergysurvey.org/).
FLRW Friedmann-Lemaître-Robertson-Walker metric of an expanding universe.
FWHM full width at half maximum.
GR general theory of relativity.
HST the Hubble Space Telescope (http://hubblesite.org/).
IFU Integral Field Unit.
IUE International Ultraviolet Explorer Satellite (https://archive.stsci.edu/iue/).
JLA Joint Light-curve Analysis.
LSQ La Silla/QUEST.
LSST Large Synoptic Survey Telescope (https://www.lsst.org/).
MLCS the Multicolor Light Curve Shape fitter.
MLCS2k2 Improved Multicolor Light Curve Shape fitter.
NBS National Bureau of Standards (https://www.nist.gov/pml).
NIST National Institute of Standards and Technology (https://www.nist.gov/).
NLTE Non Local Thermal Equilibrium.
Pan-STARRS Panoramic Survey Telescope and Rapid Response System (http://pswww.ifa.hawaii.edu/pswww/).
PSF Point Spread Function.
PTF Palomar Transient Factory (http://ptf.caltech.edu).
SALT Spectral Adaptive Lightcurve Template (http://supernovae.in2p3.fr/salt/doku.php).
SCALA SNIFS Calibration Apparatus.
SDSS Sloan Digital Sky Survey (http://sdss.org).
SED Spectral Energy Distribution.

SN Ia Type Ia supernova (Plural: SNe Ia).
DICE Direct Illumination Calibration Experiment (for SnDICE and SkyDICE).
SNfactory Nearby Supernova Factory.
SNIFS SuperNova Integral Field Spectorgraph.
SNLS Supernova Legacy Survey (http://cfht.hawaii.edu/SNLS).
STIS the Space Telescope Imaging Spectrograph (http://www.stsci.edu/instruments/stis/).
UH 88 the University of Hawaii 88-inch (2.2-meter) telescope (http://www.ifa.hawaii.edu/88inch/).
WFIRST Wide Field Infrared Survey Telescope (https://wfirst.gsfc.nasa.gov/).
ZTF Zwicky Transient Facility (http://ptf.caltech.edu/ztf).
ΛCDM Lambda Cold Dark Matter.

Acknowledgments

Carrying out a PhD is a long and hard task, and also writing the thesis is not exactly a piece of cake. I would like to take some moment to thank all the people that helped me get to this point. First of all I would like to thank you for reading my thesis. If you did not read the thesis though, or skipped some chapters, the following acknowledgments are not valid for you. Just kidding!

First of all I would like to thank my supervisor Prof. Marek Kowalski for allowing me to begin this adventure, for his optimism and all the good advises, that I hope helped me grow professionally. I would like to thank my colleagues, Dr Jakob Nordin and Dr Mickael Rigault, for all the good discussions, supervision and support during working hours and beer Wednesdays that made me proceed with my work. I would also like to thank them for reading this thesis so thoroughly and commenting on it (despite the Italianisms that are probably still there). I would like to thank Dr Yannick Copin, Dr Greg Aldering and Dr Nicolas Chotard for always being available for my silly questions about SNIFS pipeline, or observations with SNIFS, and to providing all the material needed as background for my thesis.

I would like to thank my fellow phd-office mates for making this experience great, particularly: Markus Voge, Dustin Hebecker, Dr Lukas Schulte for the nice German dinner evenings and pub quiz nights, Dr Ulrich Feindt for his great availability (and proof reading the thesis), Nora Strotjohann for the many exotic cooking evenings and nights out together (yeah I like eating, I guess now it is clear), Daniel Küsters for sharing the many Hawaiian adventure, trusting my driving and proof-reading my thesis (as you see many people read it, so if you did not like it, you can ask them). I would like to thank my Berlin flatmate, Alexander Stasik, for all the cheering up evenings at the Opera, and for making me feel less alone in the misadventure along the way.

I am also grateful to Dr Klaus Reif and Dr Akos Hoffmann for the help provided during the beginning of my PhD, and Luke McKay for making me feel welcome in Hawaii and for the many acrobatics performed to help us install SCALA in the UH 88 dome.

All these years have been very special because of the many special people I met. They all made my life richer and more joyful. For this I would like to thank Slava and Dinar for being great people and friends, and Sabrina, my grand Italian friend/shopping mate.

A special thank goes to my favorite people of the Roman time, my two incredible astrophysisist friends Donatella and Alessia, my physicist friend Daria, and my previous flatmate soon-to-be-a-super-famous-actress Silvia. Thank you so much for being there for me, supporting and believing in me even while living very very far away.

I left at the end my family, my big, messy, noisy, very much Italian family. I love all of you very much and really want to thank you to be my counselor and advisers in many hard choices I had to make during my studies and my life in general. Thank you Monica, Massimiliano, Andrea, Antonio, Gianni and Cinzia for being there when I needed it, you are the best (most of the time) siblings and brother/sister in laws that one can hope for. Thanks to all my nephews and nieces for all the funny and relaxing times (sometimes more than others) during holidays at home. A special thank goes to my aunt Franca, for all the things that she does for me without me asking, and for keeping my wardrobe well stocked. Thank you mum and dad for giving me such solid grounds and your unconditional love and support. An entire thesis would not be enough to express my gratitude and love towards you (plus you will have to have someone translating this for you or learn English, so it's better if I keep it short :D).

At last a huge thank you to Davide, my boyfriend, is on order. I should thank you for putting up with my bad moods during the many times I was under stress (even if it is actually your duty, so you know ...) and to share with me the many moments of happiness (and the trip around the world). Thank you for making me come back down to earth in those moments when my thoughts make my mind spin very fast. Thank you for just being in my life and always on my side.

I would also like to acknowledge Kyan Schahmaneche, Laurent Le Guillou and Nicolas Regnault from LPNHE for providing the CLAP modules and support. This work was supported by the German Science Foundation through TRR33 "The Dark Universe" as well as through the graduate school "Mass, Spectrum, Symmetry" GRK1504 of the Humboldt University Berlin, the Technical University Dresden and DESY Zeuthen and by the Director, Office of Science, Office of High Energy Physics, of the U.S. Department of Energy under Contract No. DE-AC02-05CH11231. We additionally thank the University of Hawaii and the UH 88 staff members for all the support provided during commissioning.